Kjersti Wergeland Krakhella

Energy Storage
by Salinity Gradients

Kjersti Wergeland Krakhella

Doctoral thesis

NTNU
Norwegian University of Science and Technology
Thesis for the Degree of
Philosophiae Doctor
Faculty of Natural Sciences
Department of Materials Science and
Engineering

NTNU
Norwegian University of
Science and Technology

NTNU
Norwegian University of
Science and Technology

NTNU

Kjersti Wergeland Krakhella

Energy Storage
by Salinity Gradients

Thesis for the Degree of Philosophiae Doctor

Trondheim, November 2019

Norwegian University of Science and Technology
Faculty of Natural Sciences
Department of Materials Science and Engineering

NTNU
Norwegian University of
Science and Technology

Acknowledgement

The work in this thesis was carried out at the Department of Material Science and the Deparment of Energy and Process Engineering from 2015 to 2019, at the Norwegian University of Science and Technology, in the renewable lab at Kalvskinnet and the lab at the Department of Energy and Process Engineering. I am grateful for the financial support from NTNU, though the Energy and Sensor Systems group (ENERSENSE), making this work possible.

Firstly, I want to thank my supervisors for guiding and supporting me through this PhD. I want to thank Kristian Etienne Einarsrud for your guidance in all the theory and simulations, and for all the priceless feedback on all written work. Thank you for calming me when the work was difficult; even while on paternity leave, you made sure everything was going well with the PhD and with me. I want to thank Odne Stokke Burheim for all your time spent on explanation, discussion and the time you spent in the lab with me. You are an idea machine and have come up with new ideas throughout the PhD, and you have also shown great involvement throughout my work. I want to thank Frode Seland for guidance in electrochemistry in meeting and at the lab, and for always quickly answering email regarding 'out of the ordinary' CV and EIS curves. I still have not found anything you cannot answer in electrochemistry.

I would also like to thank my fellow PhD collegue and friend Zohreh Jalili, whom I worked together with throughout the PhD and published a paper with. Thank you for all the time you used on explaining flow phenomena and simulation, and for all the social events where we got to relax from all the simulations and writing. You have become a close friend that I am truly grateful to share this PhD work with. I would like to thank Ellen Synnøve Skilbred and Yash Raka for numerous discussions and problem solving of membrane characterisations and RED stack measurements. I also want to thank Dr Robert Bock for all this contribution at the end of my PhD, with measurements, proofreading and discussion; without you, the finishing of this PhD would have been close to impossible. Another person who deserve great acknowledgment is Håvard Karoliussen, whom always welcomed me to ask questions on measurement setups and membrane properties. Håvard also copy-edited a large part of my thesis, which I am truly grateful for.

I have also been blessed with the best collegiate imaginable thought the researching program ENERSENSE: Laurina Felius, Jacob Lamb, Markus Wahl, Ian Muri, Md Hujjatul Islam, Felix Kelberlau, Ebrahim Hashemi and Ailo Aasen. Thank you for all

Abstract

Storing energy in salinity gradients can solve the problem of renewable energy sources being intermittent. A salinity gradient energy storage system (SGESS) is easy to scale for large capacities, uses non-toxic and environmentally friendly materials, and is relatively cheap. Another advantage is the increase in power and efficiency with increased temperature, which is an advantage when low-grade energy (e.g. heat) is available. An SGESS is charged by increasing the difference in salt concentration between two solutions, which can be done by applying surplus electrical energy or thermal energy. Both techniques are investigated in this thesis. The system can produce electricity or hydrogen gas (directly).

Three SGESSs that use electricity for charging and have electricity as an output are compared using mathematical modelling. The systems are combinations of mixing technologies; reverse electrodialysis (RED), pressure retarded osmosis (PRO) and capacitive Donnan potential (CDP) with a desalination technologies; electrodialysis (ED), reverse osmosis (RO) and membrane capacitive deionisation (MCDI). Two SGESS that use thermal waste energy for charging and with hydrogen as output are compared using modelling and by experimentally measuring certain key parameters. The first thermal separation process uses heat and decompression to evaporate water from one solution, after which the water is added to another salt solution thereby creating difference in concentration. The second thermal separation process removes heat from one solution to precipitate salt, whereupon the salt is added to another solution. This process requires heat to increase the solution temperature and to dissolve the salt. The membrane conductivity of a suitable salt for the precipitation process is measured, and the result is used to calculate the hydrogen production from RED. The energy needed for the evaporation and the precipitation process is calculated per volume of hydrogen produced. The SGESSs are closed systems where the concentrations are not restricted by naturally occurring solutions (like river and seawater). Stack and permselectivity measurements of the electrodialytic energy storage system (EESS) using NaCl concentrations close to saturation were conducted. The results were used for a simple life-cycle analysis for a 1 GWh EESS with two hours discharging time per day for 20 years.

The power density for the EESS (RED-ED) and the osmotic energy storage system (PRO-RO) at room temperature was found from modelling to be 5 W m^{-2}, while the power density of the capacitive energy storage system (CDP-MCDI) was 0.5 W m^{-2}. Raising the temperature to 60 °C increased the power density of the EESS by 80 %, and made EESS the SGESS with the highest power density. For EESS to

match the electricity prices in the EU the membrane prices need to be lower than 5.2 $ m^{-2}. KNO_3 was found to have a steep change in solubility with temperature and was therefore chosen as the salt to be used in the thermally driven RED. The membrane conductivity of KNO_3 at 40 °C was found to be 1.1±0.9 mS cm^{-1} in FAS-50 (Fumatech) and 1.8±0.7 mS cm^{-1} in FKS-50 (Fumatech). FKS-50 showed similar conductivity for K^+ and Na^+, while FAS-50 showed three to eight times higher conductivity for Cl^- compared to NO_3^-. The reason for the difference in conductivity between the two ions was not possible to determine, but it is dependent on the size of the ions. The results from the conductivity measurements were used to calculate the hydrogen production, which was 2.6±1.3 g s^{-1} m^{-2} using concentrations relevant for the evaporation process and 1.1±0.7 g s^{-1} m^{-2} using concentrations relevant for the precipitation process. The evaporation process uses 700±300 kWh per kg (55±22 kWh m^{-3}) hydrogen produced, while the precipitation process uses 104.8±0.6 kWh per kg (8.23±0.05 kWh m^{-3}) hydrogen produced. Using RED together with the precipitation process has comparable energy demand per volume hydrogen as proton exchange membrane water electrolysis (PEMWE) and alkaline electrolysis, but the energy input to PEMWE and alkaline electrolysis is high-grade energy while the Heat to H_2 system uses low-grade energy. For EESS using electricity for charging, and NaCl concentrations close to saturation (5.0 M), the permselectivity was found to be 0.7±0.1 in FAS-50 and 0.84±0.07 in FKS-50 (dilute concentration of 0.05 M), which is much lower than the permselectivity using seawater (0.92-0.99). The maximum power density from EESS was found to be 2.0±0.3 W m^{-2} at 40 °C. The life-cycle analysis of the production of an EESS showed a global warming factor of 75 kg CO_2 equivalents per MWh and cumulative energy demand of 0.26 MWh per MWh produced.

The analyses done in this PhD show how SGESS can be used to store electrical and thermal energy in salinity gradients and be used to produce electricity or hydrogen gas.

List of Papers

The following publications are included in this thesis:

(I) **Energy generation and storage by salinity gradient power: A model-based assessment**

Zohreh Jalili**, Kjersti Wergeland Krakhella**, Kristian Etienne Einarsrud and Odne Stokke Burheim*

*Corresponding author

**Jalili and Krakhella have equal collaboration in writing of this article

Journal of Energy Storage, 2019.

Kjersti Wergeland Krakhella: Responsible for the simulation and writing of the CESS and the total cost analysis, and contributor to the simulation of the EESS. *Zohreh Jalili*: Responsible for the simulation and writing of the EESS and OESS.
Kjersti and Zohreh: Contribution equally in writing the remaining of the article and the proofreading.
Odne Stokke Burheim and Kristian Etienne Einarsrud: Formulated the idea of three salinity gradient energy storage systems, and contributed with scientific feedback and otherwise advising manuscript development for editorial advising to the level of proofreading.

(II) **Heat to H$_2$**

Kjersti Wergeland Krakhella*, Robert Bock, Frode Seland, Odne Stokke Burheim and Kristian Etienne Einarsrud,

*Corresponding author

Journal of Energies, 2019.

Kjersti Wergeland Krakhella: Kjersti conducted the preparation of membranes and most of the conductivity measurements and all simulations. Kjersti has written the article with contributions from weekly supervision meetings.
Robert Bock: Robert conducted many of the conductivity measurements, contributed to discussions of the energy calculation and did copy-editing of the article. Robert also attended many of the weekly meetings.
Frode Seland: Frode has contributed with guidance in EIS and general measurements at the lab and contributed with scientific feedback and proofreading. Frode also attended many supervision meetings.

Kristian Etienne Einarsrud and *Odne Stokke Burheim*: Odne and Kristian formulate the idea of combining low-grade waste heat with RED to produce hydrogen and had weekly meetings with Kjersti for discussion, and guidance of the theory and simulations. Both contributed with scientific feedback and otherwise advising manuscript development for editorial advising to the level of proofreading.

(III) **Electrodialytic Energy Storage System: IEM Permselectivity, Stack Measurements and LCA**

Kjersti Wergeland Krakhella, Marjorie Alejandra Morales Arancibia, Robert Bock, Frode Seland, Kristian Etienne Einarsrud and Odne Stokke Burheim

Manuscript

Kjersti Wergeland Krakhella: Measured membrane permselectivity and potential from the RED stack and did all the calculations and simulations, and has contributed to the LCA of the RED system. Kjersti has written the article with contributions from weekly supervision meetings.

Marjorie Alejandra Morales Arancibia: Did the LCA in SimaPro.

Robert Bock: Robert has joined in discussions, contributed with scientific feedback and did copy-editing of the article. Robert also joined many of the weekly meetings.

Frode Seland: Frode has contributed with guidance in electrochemistry and general measurements at the lab. He has also contributed with discussions at many of the weekly meetings.

Kristian Etienne Einarsrud and *Odne Stokke Burheim*: Formulate the idea of combining RED and ED to an energy storage system, and to use waste heat to increase its efficiency. They guided Kjersti in the measurements and theory, thought weekly meeting, and contributed with scientific feedback and otherwise advising manuscript development for editorial advising to the level of proofreading.

Contents

List of Abbreviations

AEM   anion exchange membrane

CDP   capacitive Donnan potential

CED   cumulative energy demand

CEM   cation exchange membrane

CESS   capacitive energy storage system

CPE   constant phase element

ED   electrodialysis

EESS   electrodialytic energy storage system

EIS   electrochemical impedance spectroscopy

IEM   ion exchange membrane

LCA   life-cycle analysis

LSV   linear sweep voltammetry

MCDI   membrane capacitive deionisation

OCV   open-circuit voltage

OESS   osmotic energy storage system

PRO   pressure retraded osmosis

RED   reverse electrodialysis

RO   reverse osmosis

SCTD   saturation concentration temperature dependency

SGES(S)   salinity gradient energy storage (system)

SGP   salinity gradient power

SHE   standard hydrogen electrode

Part I

Thesis

This part gives an introduction to the field of salinity gradient energy storage, where relevant theory and methodology is presented. It continues with summaries of the papers, an overall conclusion and a suggestion for further work. It should be emphasised that most of the information provided in this part is given in the papers as well.

Introduction

1

In the early 1800s, John Tyndall first discovered what is now called the greenhouse effect [1, p.3]. Although the awareness of human influence on climate and attention towards non-polluting energy sources has increased, recent research shows that 80 % of the global energy still originates from oil, gas, coal and bio-fuels [2]. However, it is predicted that by 2050 70 % of the energy production will come from solar and wind energy [3]: The so-called green transition. Both these sources are intermittent, and wind in particular is most efficient in rural areas according to the Norwegian Water Resources and Energy Directorate [4]. Due to the intermittent behaviour and location of renewable energy sources, energy storage technology will play an essential role in the green transition.

Large scale rechargeable batteries is one solution to store energy. An extensive effort into battery development has been conducted, however many problems remain. The main drawbacks are low capacity and efficiency, high cost, short lifetime, hazardous environmental materials (like lead and sulphuric acid), and specialised manufacturing technologies which make battery products expensive [5]–[7].

Among different sources of energy to utilise in a battery, capturing and storing chemical energy associated with salinity gradients and converting it to electricity was introduced by Pattle in 1954 [8]. In 1970 and 2000 the interest in so-called blue energy (energy driven by osmotic power [9]) increased, which overlaps with increased oil prices [10], [11]. This type of energy has many advantages compared to other renewable energy sources, e.g. its continuity with respect to time, unlike wind or solar energy which have a cyclic nature.

Available energy from a salinity gradient as a function of concentrations has been studied by several research groups [8], [12]–[15]. Post et al. [14] demonstrated that for every cubic meter of river water mixed with seawater, 2.3 MJ of available energy is released. In other words, the osmotic pressure corresponds to the pressure from a water column of 250 m. In this perspective, the available energy is comparable to the pumped hydro that already exists. Using a combination of saturated and highly diluted NaCl solutions, the available energy is 15 MJ m^{-3} [14], which is comparable to compressed hydrogen at 3 bar. Since other salts are usable in the same setup, the energy density could potentially be even higher.

A salinity gradient energy storage system (SGESS) can be charged using a desalination technology, increasing the concentration difference between two solutions, while the discharging process is through a mixing technology, decreasing the concentration difference between the two solutions. Given the use of the same solutions throughout the charging-discharging cycle, this storage technology could be a closed system, where effects of biofouling can be made negligible, and the temperature is easy to control. An illustration of an energy storage system utilising salinity gradients is shown in Fig. 1.1.
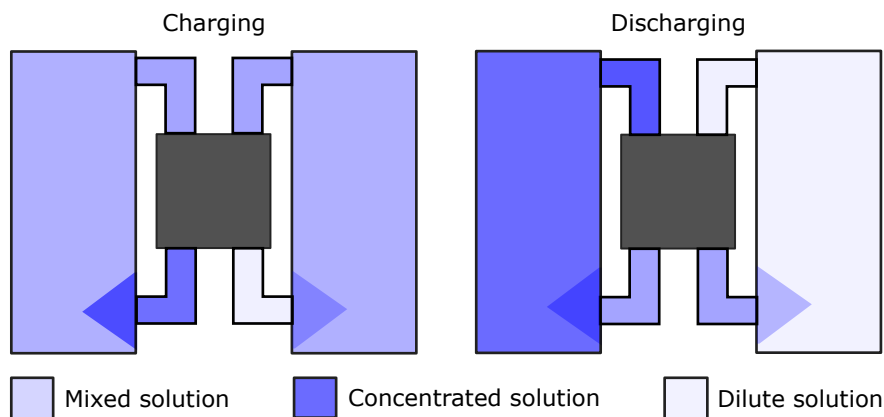
Fig. 1.1: Schematic diagram of a salinity gradient energy storage system. During charging, energy is stored in the form of higher concentration difference, while discharging is the mixing of the two solutions, and electric energy is generated.

Examples of combined mixing and desalination systems are reverse electrodialysis (RED) and electrodialysis (ED), pressure retarded osmosis (PRO) and reverse osmosis (RO), and capacitive Donnan potential (CDP) and membrane capacitive deionisation (MCDI). The separated mixing and desalination technologies have been discussed in various literature for energy generation [5], [11], [14], [16]–[19], but so far RED/ED is the only technology mentioned as a pair [5], [20].

To evaluate the potential and power available in the three suggested coupled systems, a model was made where input parameters for the three systems were kept as equal as possible. For the electrodialytic energy storage system (EESS), experimental data on membrane and stack performance is obtained to evaluate the available power density, and for using RED as a hydrogen-producing unit. In addition, two different process that use heat to separate the mixed salt solutions are evaluated.

To determine the charging and discharging conditions for a SGESS the duck curve constraint was used [21]. This constraint is evident in the net electric load of the grid

system in California [22] which includes a forecast for 2020. The data is plotted in Fig. 1.2. Due to installation of solar cells, the energy peak during midday decreases from 2012 to 2020, while the power peak in the evening remains, resulting in a so-called duck curve. During the low power at midday energy can be stored for use during peak demand in the evening. The peak in the evening is approximately half of the peak at midday, which indicates the need of a charging current density half the discharging current density.
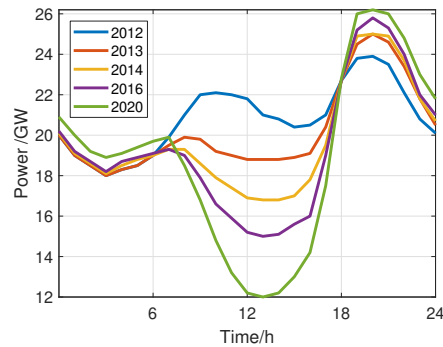
Fig. 1.2: California net electricity load requirement [22] with forecasts for 2020.

The driving force of an EESS, the liquid junction potential, increases with temperature [20], where surplus waste heat can be used to increase the temperate of the solutions in EESS. In Norway alone, the annual available waste heat between 25 °C and 140 °C is 20 TWh [23]–[25]. Given the high availability of more or less free thermal energy, all modelling and experiments were carried out at elevated temperatures in addition to room temperature.

1.1 Aims of this Thesis

This PhD thesis aims to develop new large scale energy storage systems using the available energy in salinity gradients. The overall aim of this thesis can be limited to the following goals:

- Build and optimise test stations for membranes and stack measurements for SGESSs.

- Present and compare possible combinations of mixing technologies and desalination technologies to form SGESSs.

- Conduct stack, permselectivity and membrane ion conductivity measurements at relevant temperatures and concentrations for the SGESSs.

- Investigate alternative charging mechanisms for the SGESSs.

- Investigate the use of RED as a hydrogen-producing unit.

Background

<div style="text-align: right; font-size: 2em;">2</div>

2.1 Donnan Potential

The potential between two solutions with different concentrations is called the liquid junction potential [26, p.107]. If the solutions are separated by a semi-permeable membrane the potential is referred to as a Donnan potential. The open-circuit voltage (OCV) is given as:

$$E_{\text{OCV}} = \overline{\alpha} \frac{RT}{zF} \ln\left(\frac{a_{\text{c}}}{a_{\text{d}}}\right), \tag{2.1}$$

where R is the ideal gas constant, T is the temperature in Kelvin, F is Faraday constant, z is the valence number, and a_{c} and a_{d} are the activities of the concentrated and dilute solutions respectively. The average permselectivity, $\overline{\alpha}$, is defined in the next section.

2.1.1 Permselectivity

The permselectivity expresses the ability to discriminate between ions with different charge. It is highly depended on solution concentration and transport number of salt and water, but it is less dependent on solution temperature [27], and normally within in the range of 0.9 to 1 [27]–[29] for concentrations resembling those of sea and river water. The theoretical permselectivity for an ion exchange membrane (IEM) is given in Eq. (2.2) [27]:

$$\begin{aligned} \alpha &= t_s - t_w \times M_W \times \frac{b_1 - b_2}{\ln((b_1 \times \gamma_1)/(b_2 \times \gamma_2))} \quad (b_1 \neq b_2) \\ \alpha &= t_s - t_w \times M_W \times b_1 \qquad\qquad\qquad\quad (b_1 = b_2), \end{aligned} \tag{2.2}$$

where t_s and t_w are the transport number of salt and water respectively, M_w is the molar weight of water (0.018 kg mol^{-1}), and b_1 and b_2 are the molalities of the solutions on each side of the membrane. Given a constant transport number

of salt and water, the permselectivity will rise with an increasing difference in concentration.

The transport number of salt is defined as the fraction of the total current carried by the counterion [30]. If more co-ions are transported along the salt gradient, the transport number decreases. The amount of co-ions in the membrane is dependent on the external salt concentrations and the concentration of fixed charges in the membrane [30]. An anion exchange membrane (AEM) and a cation exchange membrane (CEM) from Fumatech (FAS-50 and FKS-50) has an average of 0.13 mol and 0.10 mol fixed charges per square meter membrane, respectively [28], [29].

Zlotorowicz et al. [27] measured the transport number of NaCl in the membranes FAD and FKD from Fumatech at a concentration up to 0.6 M, and found the transport numbers 0.93 and 0.998 for CEM and AEM, respectively. Długołęcki et al. [31] modelled the transport number of NaCl in the same membranes as Zlotorowicz et al. [27], where linear regression gives these salt transport numbers for FKS and FAD from Fumatech (NaCl):

$$
\begin{aligned}
t_s^{\text{AEM}} &= -0.09 \times c + 1 \text{ mol L}^{-1} \\
t_s^{\text{CEM}} &= -0.03 \times c + 1 \text{ mol L}^{-1}
\end{aligned}
\tag{2.3}
$$

where c is the molarity of the solution. For our use, c is set to be the mean value of the solutions on each side of the membrane. It should be emphasised that both Długołęcki et al. [31] and Zlotorowicz et al. [27] operated at low NaCl concentrations (0.5 M and 0.6 M), whereas in this thesis, the concentrations range from 0.05 M to 5 M. However, it should be noted that Eq. (2.3) is solely used for calculating a point of reference for the measurements.

The water transport number is affected by osmosis and electroosmosis [32]. The water transport due to osmotic forces is from the dilute to the concentrated solution, and this reduces the permselectivity. The electro-osmotic water transport is water carried as a hydration shell around the ions (hydration number), mainly going from the concentrated to the diluted solution, increasing the permselectivity. The osmotic effect increases with difference in concentration, while the number of water molecules per ion is lowered with concentration [33]. Zlotorowicz et al. [27] measured the transport number of water to be 8 and 6 for CEM and AEM respectively. The permselectivity is plotted in Fig. 2.1, with a salt transport number given Eq. (2.3), water transport number equal to 5, and activity coefficients equal to unity.
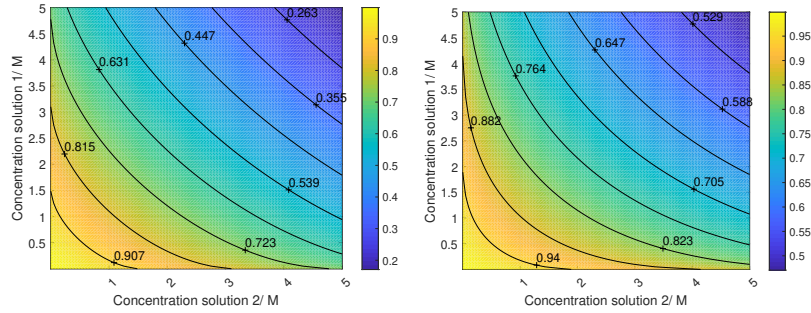
Fig. 2.1: Permselectivity for AEM (left) and CEM (right). Water transport number equal to 5 and transport number of salt given by Eq. (2.3) and activity coefficient equal to unity.

2.1.2 Activity

The activity of a solution is the product of the concentration, b (mol kg^{-1}), and the activity coefficient, γ. The activity coefficient is typically set to 1 for low concentrations (<0.1 M) [26]. For most of the work carried out in this PhD the concentrations exceed this limit and reach an upper limit of 5 M. Activity coefficients for solutions with concentrations greater than 1 M lie beyond Debye-Hückel, Davies and Truesdell-Jones models limitations. The Stokes-Robinson equation is therefore used [34], [35]:

$$\gamma_{\pm} = exp\left(\frac{A \times z_{\pm}^2 \times \sqrt{I}}{1 + B \times a_i\sqrt{I}} - \frac{h}{\nu}\ln(a_w) - \ln(|1 + (M_{\mathrm{w}}(\nu - h) \times b|) \right) \qquad (2.4)$$

where I is the ionic strength, with 1 mol kg^{-1} as reference, $z_{\pm}^2$ is the mean valence number of the anion and cation (1 for NaCl) and ν is the number of ions per molecule (2 for NaCl). h is the hydration number and a_i is the distance of the closest approach (the minimum distance between the center core of two particles before it is reflected). h and a_i for NaCl are found to be 5.2 and 0.42 nm from curve fitting to data from [36] using Eq. (2.4). The hydration number is dependent on temperature and concentration [33]; this is however not taken into consideration for the modelling in this thesis. The variables A and B from Eq. (2.4) are temperature dependent and

given in Eq. (2.5) ($A = 1.18$ (kg/mol)$^{1/2}$ and $B = 3.29 \times 10^9$ (kg/mol)$^{1/2}$ m^{-1} at 25 °C [37]).

$$
\begin{aligned}
A &= (2\pi N_A \rho_w)^{1/2} \left(\frac{e^2}{4\pi\epsilon_0\epsilon_{r,w}k_B T} \right)^{3/2} \\
B &= e \left(\frac{2N_A\rho_w}{\epsilon_0\epsilon_{r,w}k_B T} \right)^{1/2},
\end{aligned}
\tag{2.5}
$$

where N_A is Avogadro's constant, ρ_A is the density of the solvent (here water and set to be 1000 kg m^{-3} for simplicity), e is the elementary charge, ϵ_0 is permittivity of vacuum and k_B is Boltzmann constant. $\epsilon_{r,w}$ is the dielectric constant of the solvent [38] and given in Eq. (2.6) (rewritten to use Kelvin instead of Celsius):

$$
\begin{aligned}
\epsilon_{r,w} = 87.74 &- 0.4008(T - 273.2) + 9.398 \times 10^{-4}(T - 273.2)^2 \\
&- 1.410 \times 10^{-6}(T - 273.2)^3 \quad (2.6)
\end{aligned}
$$

In Eq. (2.4), a_w is the water activity as a function of the salt concentration given in Eq. (2.7) [39]:

$$
\begin{aligned}
a_w &= \gamma_w \times x_w, \text{ where} \\
\gamma_w &= \alpha_{a_w} x_s^2 + \beta_{a_w} x_s^3, \\
x_s &= \frac{b}{b + 1/M_w} \text{ and} \\
x_w &= \frac{1/M_w}{b + 1/M_w},
\end{aligned}
\tag{2.7}
$$

where γ_w is the activity coefficient of water (equal to 1 with no salt present), x_w is the mole fraction of water, x_s is the mole fraction of salt, α_{a_w} and β_{a_w} are constants found by Miyawaki to be 1.825 and -20.78 respectively for NaCl [39].

The predicted activity coefficient for NaCl from the Stokes-Robinson equation (Eq. (2.4)) is plotted in Fig. 2.2 together with the data from Pytkowicz [36].

One reason for the deviation between the activity coefficients predicted by the Stokes-Robinson equation and the measured activity coefficient for NaCl is the assumption of no temperature or concentration dependency in the hydration number.
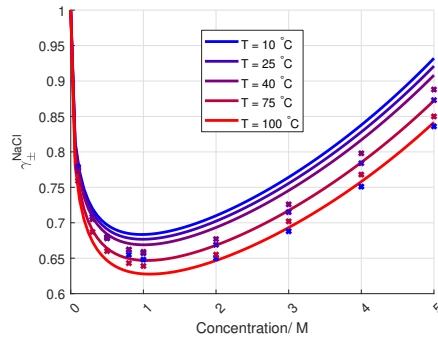
Fig. 2.2: Predicted activity coefficient for NaCl for different concentrations and temperatures, together with data from [36]. The model follows the Stokes-Robinson equation, with a_{NaCl} and h_{NaCl} found by curve fitting to data from [36].

Afanasiev et al. [40] suggest an exponential dependence on concentration and and a negligible dependence on temperature, while Onori [41] gives a linear dependence on concentration and states that the hydration number is dependent on temperature. For simplicity, neither the dependence on temperature nor concentration is taken into consideration for this work. The difference between measured and modelled data increases with increasing concentration and decreasing temperature and is a maximum of 11 % (at 5 M and 10 °C).

Increasing the difference in solution activity in the EESS will increase the OCV and thus the power density. The activity is also affected by the temperature, but the impact is less than that of the concentration.

2.1.3 Solution Density

When combining equations which use molality (mol kg⁻¹) with equations using molarity (mol L⁻¹), there is a need for an equation to transpose between the mass of the solvent (in molality) and the volume of the solution (molarity). From [42] wt%, density and molarity of NaCl is given at 25 °C. The temperature dependence on the density is not taken into consideration, whereas the change is approximately 4 % from 0 to 100 °C [43]. The density of a NaCl solution is then given as:

$$\rho_{\text{NaCl}} = 0.03709 \times c + 1.002 \text{ kg L}^{-1} \tag{2.8}$$

For all the calculations using KNO_3 the concentrations were in molality.

2.2 Salinity Gradient Energy Storage Systems

Three SGESS are investigated in this PhD. The first and most in-depth investigated is an EESS. The second is an osmotic energy storage system (OESS), and the third one is a capacitive energy storage system (CESS). These three systems are described in detail in this section.

2.2.1 Electrodialytic Energy Storage System

An EESS combines ED (charging) and RED (discharging) [5], [20], [21]. Alternating AEMs and CEMs separate flow channels with alternating concentrated and dilute solutions. At each end of the membrane stack, a redox solution is circulating at the electrodes, converting the ionic current to an electric current. When the system is charged, external power is used to force the ions from the dilute solution to the concentrated solution, where the membranes induce a net migration of anions towards the cathode and a net migration of cations towards the anode [21]. During discharge the ionic current is reversed and a voltage over the electrodes can be utilised. An illustration of RED, with NaCl as the driving salt and $FeCl_2$ and $FeCl_3$ as the redox couple, is given in Fig. 2.3.
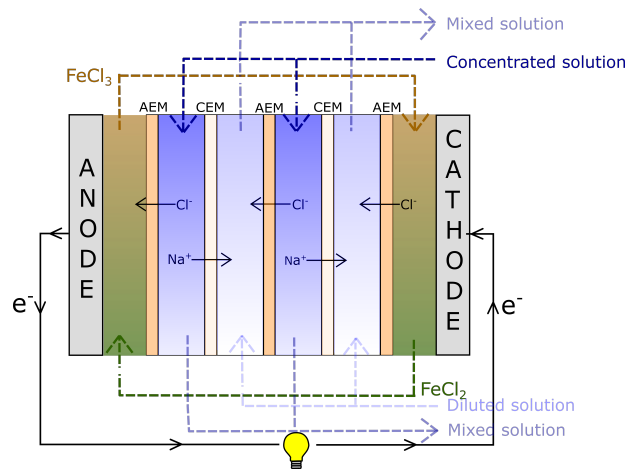
Fig. 2.3: The figure illustrates a RED cell stack which utilises the salinity gradient between two solutions with different concentrations. To convert from a flow of ions to a flow of electron, $FeCl_2$ and $FeCl_3$ is used as a redox couple at the electrodes .

An advantage with RED and ED is the flexible operation with a wide range of suitable inorganic salts and the possibility of being run in reverse without the need for exchanging chemicals or the cell stack. ED is most widely used in the food

industry and desalination. This technology is also proposed and developed for the mining industry when enriching minerals in process streams (cf. [44] for more information on this topic). The technology where ED shows the most potential is in the use of salinity gradient between sea and river water [26].

When the system is discharged, chloride ions migrate from the redox to the membrane stack at the cathode, while the chloride ions migrate from the membrane stack to the redox at the anode side. The reactions at each electrode are:

$$
\begin{aligned}
\text{Anode: } Fe^{2+} &\rightarrow Fe^{3+} + e^- \\
\text{Cathode: } Fe^{3+} + e^- &\rightarrow Fe^{2+}
\end{aligned}
\tag{2.9}
$$
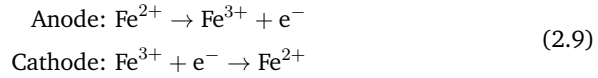
When charging the EESS electrons are forced from the anode to the cathode using an external power source, reversing the reactions given in Eq. (2.9).

The driving potential of the EESS is the liquid junction potential, E_{OCV}, given in Eq. (2.1). The total cell potential for charging and discharging is given in (2.10):

$$
\begin{aligned}
E^{\text{charging}} &= E_{\text{OCV}} + r_\Omega \cdot i^{\text{charging}} \\
E^{\text{discharging}} &= E_{\text{OCV}} - r_\Omega \cdot i^{\text{discharging}}
\end{aligned}
\tag{2.10}
$$

where i is the current density per membrane area and r_Ω is the ohmic resistance ($\Omega\,m^2$) of a unit cell. The latter is the sum of the resistance of one AEM, one CEM, one compartment of dilute and one compartment of concentrated solution. The electrode resistance, $r_{\text{electrode}}$, can be assumed to be negligible for a stack containing a large number of cell pairs [16], but at laboratory scale, it needs to be considered. The ohmic resistance in one unit cell is given in Eq. (2.11) [45]:

$$
r_\Omega = \frac{r_{\text{AEM}}}{(1-\beta)} + \frac{r_{\text{CEM}}}{(1-\beta)} + \frac{d}{\rho_d \epsilon^2} + \frac{d}{\rho_c \epsilon^2},
\tag{2.11}
$$

where r_{AEM} and r_{CEM} ($\Omega\,m^2$) are the ohmic resistances of the AEM and CEM respectively, β (dimensionless) is the spacer shadow [46] or the part of the membrane covered by a spacer, d (m) is the thickness of the spacer, ϵ (dimensionless) is porosity or the factor to correct for the occupied volume by the spacer and equal to 1 with no spacer. The porosity is defined as 1 minus the volumetric ratio (ratio of apparent gravity and the specific gravity of the spacer) [47]. ρ_d and ρ_c are the resistivity of the dilute and concentrated solutions respectively ($\Omega\,m$). Theoretical values are

deduced from conductivity measurement of NaCl in water at 25 °C from [48] (wt% to mol L^{-1} and μS cm^{-1} to S m^{-1}), and fitted to the Kohlrausch's equation given in [30, p.22]:

$$\sigma_{\text{sol},25}^{\text{NaCl}} = k_1 \times c - k_2 \times c^{3/2} \tag{2.12}$$
$$k_1 = 11.8 \pm 0.2 \text{ S m}^{-1} \text{ L mol}^{-1}$$
$$k_2 = 2.7 \pm 0.1 \text{ S m}^{-1} \left(\text{L mol}^{-1}\right)^{3/2}$$

where $\sigma_{sol,25}^{\text{NaCl}}$ is the conductivity of a NaCl solution at 25 °C (S m^{-1}) and c is the molarity. The effect of temperature on resistance was correlated via the following relationship [49]:

$$\rho_{\text{sol}}^{\text{NaCl}} = \frac{1}{\sigma_{sol,25}^{\text{NaCl}}} \frac{46.5 \text{ K}}{T - 251.5 \text{ K}} \tag{2.13}$$

where the equation is rewritten to use Kelvin instead of Celsius.

The conductivity of a solution with KNO$_3$ is found from Isono [50]. The relevant temperatures for this salt is 25 °C and 40 °C, where Isono [50] measured the conductivity at 25 °C, 35 °C and 45 °C (amongst others). The conductivity at 40 °C is taken to be the average between the conductivity at 35 °C and 45 °C. Theoretical values are deduced from conductivity measurement of KNO$_3$ from [50], and fitted to Eq. (2.12) with constants equal to:

$$k_1^{25\,°\text{C}} = 12.2 \pm 0.3 \text{ S m}^{-1} \text{ L mol}^{-1}$$
$$k_1^{40\,°\text{C}} = 15.8 \pm 0.4 \text{ S m}^{-1} \text{ L mol}^{-1}$$
$$k_2^{25\,°\text{C}} = 3.4 \pm 0.2 \text{ S m}^{-1} \left(\text{L mol}^{-1}\right)^{3/2}$$
$$k_2^{40\,°\text{C}} = 4.5 \pm 0.3 \text{ S m}^{-1} \left(\text{L mol}^{-1}\right)^{3/2}$$

The power requirement for charging the EESS unit cell and the power gained from the discharging the EESS, excluding pumping power consumption, is the product of the current density and the potential (Eq. (2.10))

$$P_{\text{charging}} = E_{\text{OCV}} i_{\text{charging}} + r_{\Omega} i_{\text{charging}}^2,$$
$$P_{\text{discharging}} = E_{\text{OCV}} i_{\text{discharging}} - r_{\Omega} i_{\text{discharging}}^2, \tag{2.14}$$

while the reversible power density is given as:

$$P^{\text{rev}} = i E_{\text{OCV}}. \tag{2.15}$$

The derivative of Eq. (2.14) is used to find the current at peak power density for the discharging process:

$$i_{\text{discharging}}^{\text{peak power}} = \frac{E_{\text{OCV}}}{2r_{\Omega}}, \tag{2.16}$$

while the peak power density is (inserted Eq. (2.16) into Eq. (2.14)):

$$P_{\text{discharging}}^{\text{peak}} = \frac{E_{\text{OCV}}^2}{4r_{\Omega}}. \tag{2.17}$$

The charging current is set to be half the discharging current, explained in the introduction. This give a power density for charging equal to:

$$P_{\text{charging}} = \frac{5E_{\text{OCV}}^2}{16r_{\Omega}}. \tag{2.18}$$

2.2.2 Osmotic Energy Storage System

An OESS uses RO to charge and PRO to discharge. Semipermeable membranes are used where water is transported through the membranes, while the salt is stopped. The water transport is spontaneous from dilute to concentrated solution (PRO), but needs an applied pressure that exceeds the osmotic pressure to go from the concentrated to the dilute solutions (RO).

Reverse osmosis was developed around 1960 for water desalination [51], where the first plant was build in Kuwait speeding up the research on osmotic membranes [52], [53]. Over 60 % of today's capacity on desalination is with RO [54]. A high-pressure pump and vessel provides pressure higher than the osmotic pressure, typically 20-25 bar between the river water and seawater [14]. A typical operating pressure in RO is around 60-80 bar when using a conversion system of seawater to freshwater utilising commercial membranes [53]. When water is transported through the membrane, demineralised water is accumulated on one side of the membrane and impurities and salt are left on the other side.

Pressure retarded osmosis was invented by Prof. Sidney Loeb in 1973 [55], [56], but got most attention after the first plant opened in Norway in 2009 [56], [57]. In PRO water diffuses through the membrane from a low salinity solution to a high salinity solution due to the driving force of the chemical potential gradient across the membrane. The pressure is lower in PRO than in RO. A simplified sketch of an OESS is shown in Fig. 2.4.
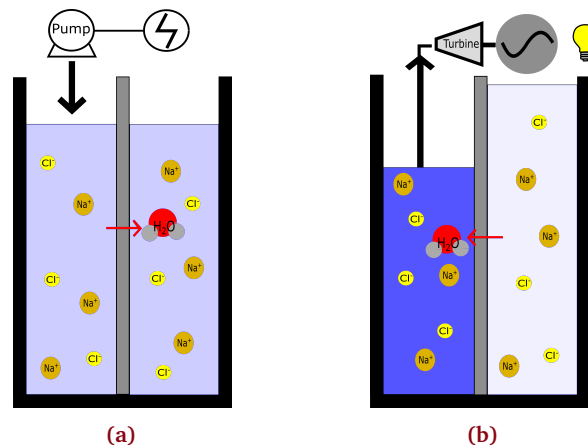
Fig. 2.4: The figure shows a schematic of the OESS where (a) illustrates the charging mode (RO) and (b) illustrates the discharging mode (PRO). Darker colour indicates higher salt concentration.

The driving force in OESS is the pressure difference between the two solutions and it is defined as [16]:

$$E_{\text{RO/PRO}}^{\text{drive}} = \Delta\pi = 2RT(c_{\text{c}} - c_{\text{d}}), \tag{2.19}$$

where $\Delta\pi$ is the osmotic pressure, and c_c and c_d are the concentration of the concentrated and the dilute solutions respectively ($[c]=$ mol m^{-3} $=1000$ M).

The hydrostatic pressure for charging and discharging the OESS can be calculated by [16]:

$$
\begin{aligned}
\Delta p_{\text{h,charging}} &= \Delta\pi + \frac{J_{\text{charging}}}{K_\text{w}}, \\
\Delta p_{\text{h,discharging}} &= \Delta\pi - \frac{J_{\text{discharging}}}{K_\text{w}},
\end{aligned}
\tag{2.20}
$$

where J is the water flux and K_w is the water permeability of the membrane. The water permeability for osmotic membranes typically varies between 0.41 and 10 pm (Pa s)$^{-1}$ [16], [58], [59], and is dependent on diffusivity inside the membrane, membrane swelling and density of solution which all are temperature dependent [60]. However, in the modelling of the OESS, the water permeability is independent of both temperature and concentration.

The power density is the product of water flux across the membrane and the hydrostatic pressure drop (analogous to the electric current and potential in RED/ED) according to Eq. (2.21):

$$
\begin{aligned}
P_{\text{charging}} &= J_{\text{charging}}\Delta p_{\text{h,charging}} = J_{\text{charging}}\left(\Delta\pi + \frac{J_{\text{charging}}}{K_\text{w}}\right) \\
P_{\text{discharging}} &= J_{\text{discharging}}\Delta p_{\text{h,discharging}} = J_{\text{discharging}}\left(\Delta\pi - \frac{J_{\text{discharging}}}{K_\text{w}}\right),
\end{aligned}
\tag{2.21}
$$

The derivative of the discharging power density in Eq. (2.21) is used to find the water flux at peak power density for the discharging process:

$$
J_{\text{discharging}}^{\text{peak power}} = \frac{K_\text{w}}{2}\Delta\pi
\tag{2.22}
$$

This way to express the water flux is to keep an analogy to EESS and CESS. The water flux while charging is set to half the water flux while discharging, due to the

duck curve constraint [21]. The peak power density for charging and discharging is calculated as:

$$P_{\text{charging}} = 2 \times \frac{5K_{\text{w}}}{16} \Delta \pi^2$$
$$P_{\text{discharging}}^{\text{peak}} = 2 \times \frac{K_{\text{w}}}{4} \Delta \pi^2, \tag{2.23}$$

The factor two in Eq. (2.23) and (2.24) is to keep the analogy to the two other energy storage systems; one membrane is needed per unit cell for the OESS, while two membranes are needed for the current density used in EESS and CESS. The reversible power density is defined as:

$$P^{\text{rev}} = 2 \times J \Delta \pi \tag{2.24}$$

2.2.3 Capacitive Energy Storage System

A third energy storage technique analysed in this PhD is a CESS, combining MCDI and CDP. During both charging and discharging, ions enter and leave two porous electrodes [61]–[63].

The charging of the system is based on MCDI, first introduced by Claude et al. [64], [65]. Membrane capacitive deionisation is used for desalination, as in RO and ED, but it is also used in insulin purification, and in general as an assistant in multiple separation processes [54]. An illustration of the MCDI system is provided in Fig. 2.5. An AEM and a CEM are placed on each electrode, enabling selective ion transport.

There are four steps in one cycle of MCDI. In the first step, there is no current flowing (open circuit), and the chambers between the electrodes are filled with a mixed solution. During the second step the circuit is closed and a potential is applied over the electrodes. The positive ions flow to the negative electrode and negative ions to the positive electrode forming an electrical double layer [65], [66] and a Donnan potential over the two membranes. The outlet solutions from the cell are less concentrated than the inlet solutions. The third step happens at open circuit again, and the channel between the electrodes is filled with a new solution. During the fourth step, the outer circuit is closed, and the potential is reversed compared to the second step. Ions are forced from the electrodes to the solution. The outlet solution from the system is now more concentrated than the inlet, where the outlet solution is lead to a new compartment compared to the outlet flow from step two. Continuous alternations between solutions and current directions gradually increase
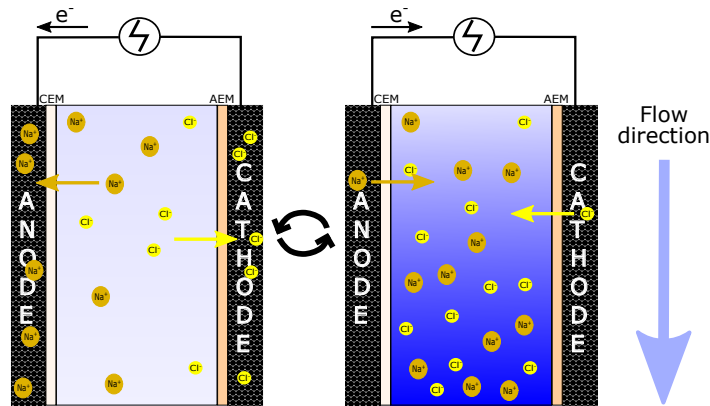
Fig. 2.5: Illustration of the charging of the CESS (MCDI). A solution flows into the
system which alternates between producing a dilute (left) and concentrated
solution (right) by alternating ion exchange with porous electrodes. Elec-
trodes are charged when producing the dilute solution and discharged when
producing the concentrated solution. Each solution is stored in separate
containers.

the concentration difference between the two solutions, and in this way charges the
storage system.

The discharging of the CESS is based on CDP, first proposed by Sales et al. in
2010 [67]. The cell design of CDP can be identical to the cell design of MCDI [68],
promoting a combined energy storage system. An illustration of a CDP system with
ionic flow is shown in Fig. 2.6.

A full CDP cycle has four steps. The first step happens at open circuit, and the
membrane-covered electrodes are polarised by immersing them in a concentrated
solution, resulting in a Donnan potential over each of the membranes. In the second
step, the electrodes are connected to an external load closing the outer circuit and
allowing ions to flow from the concentrated solution in the channel, through the
membranes, to the less concentrated solution in the pores of the electrode. The
flow of electrons and ions stops when the electrodes attain charge neutrality. The
outlet solution from the channel is less concentrated than the inlet solution. In the
third step, the circuit is open again, and a dilute solution replaces the concentrated
solution. The electrode pore concentration is forthwith higher than the concentration
in the channel, promoting ion transport from the pores, through the membranes, to
the channel due to the reversed Donnan potential [69]. In the fourth and last step,
the electrodes are connected to an external load, where the electrons flow in the
opposite direction compared to the second step. The outlet flow of solution from
the channel is more concentrated than the inlet solution. Continuous alternations
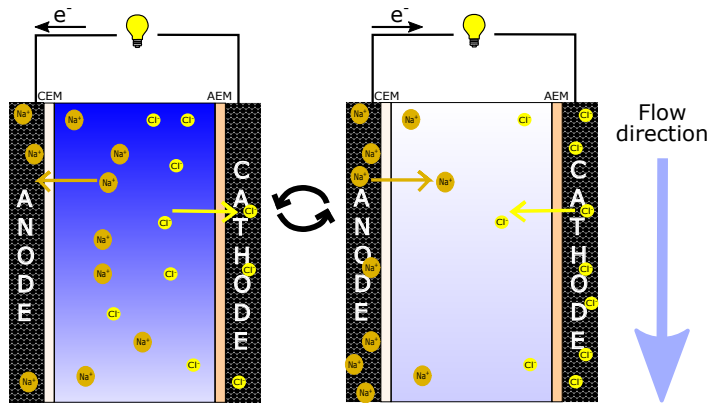
Fig. 2.6: The figure shows an illustration of the CDP technology. Concentrated (left) and dilute (right) solutions flow alternately into the system producing a solution of mixed concentration. Electrodes are charged while the concentrated solution is flowing and discharged to the dilute solution in a spontaneous process.

between concentrated and dilute solution, and alternation of the current directions gradually decreases the concentration difference between the two solutions, and thereby discharging the storage system. [70]

The driving force in CESS stems from the Donnan potential, E_{Donnan}, and from the capacitive potential, E_{c}:

$$E_{\text{MCDI/CDP}}^{\text{drive}} = E_{\text{Donnan}} + E_{\text{c}}, \tag{2.25}$$

Including the ohimc losses the total cell potential in CESS is [70]:

$$E_{\text{MCDI/CDP}} = E_{\text{Donnan}} + E_{\text{c}} - ir_{\Omega}, \tag{2.26}$$

The current density is defined as positive while adding ions to the electrode (see Fig. 2.6) and negative when ions are removed from the electrode. The Donnan potential in the CESS is equivalent to Eq. (2.10), where the concentration difference is between the solution in the electrode and the solution in the flow channel:

$$E_{\text{Donnan}} = 2\overline{\alpha}\frac{RT}{zF}\ln\left(\frac{a_{\text{ch}}}{a_{\text{el}}}\right), \tag{2.27}$$

where a_{ch} is the activity of the solution in the flow channel and a_{el} is the activity of the solution in the electrode pores. During both charging and discharged of the CESS the potential alternates between positive and negative depending on the direction of the salinity gradient between the flow channel and the electrode pores [68], [71].

The capacitive potential for CDP and MCDI is given as:

$$
\begin{aligned}
E_{\text{c,MCDI}} &= E_{\text{c,0}} + \frac{i_{\text{MCDI}}}{C_{\text{MCDI}}} t_{\text{MCDI}} \\
E_{\text{c,CDP}} &= E_{\text{c,0}} - \frac{i_{\text{CDP}}}{C_{\text{CDP}}} t_{\text{CDP}},
\end{aligned}
\tag{2.28}
$$

$E_{\text{c,0}}$ is the initial capacitive potential when charging or discharging the electrodes and C is the capacitance of the unit cell. t_{MCDI} and t_{CDP} is the time it takes from a new solution entering the flow channel until the total potential (Eq. (2.26)) reaches zero:

$$
\begin{aligned}
t_{\text{MCDI}} &= \frac{C}{i} (-E_{\text{d}} - E_{\text{c,0}} + i r_{\Omega}) \\
t_{\text{CDP}} &= \frac{C}{i} (E_{\text{d}} + E_{\text{c,0}} - i r_{\Omega})
\end{aligned}
\tag{2.29}
$$

The ohmic resistance in MCDI and CDP are similar to ED and RED, but the unit cell contains only one compartment. The flow channel concentration is concentrated while adding ions to the electrodes in CDP and while removing ions from the electrodes in MCDI. The resistance is equal to:

$$
r_{\Omega,\text{CDP}}^{\text{add}} = r_{\Omega,\text{MCDI}}^{\text{remove}} = \frac{r_{\text{AEM}}}{1 - \beta} + \frac{r_{\text{CEM}}}{1 - \beta} + \frac{\rho_{\text{c}} h_{\text{c}}}{\epsilon^2} + r_{\text{electrodes}}
\tag{2.30}
$$

The solution in the flow channel is diluted while removing ions from the electrodes in CDP and while adding ions to the electrodes in MCDI. The resistance is, therefore, equal to:

$$
r_{\Omega,\text{CDP}}^{\text{remove}} = r_{\Omega,\text{MCDI}}^{\text{add}} = \frac{r_{\text{AEM}}}{1 - \beta} + \frac{r_{\text{CEM}}}{1 - \beta} + \frac{\rho_{\text{d}} h_{\text{d}}}{\epsilon^2} + r_{\text{electrodes}}
\tag{2.31}
$$

By including the cell resistances (Eq. (2.30) and (2.31)) in the equation for the total cell potential (Eq. (2.26)), the total cell potentials while charging and discharging the OESS are given as:

$$
\begin{aligned}
E_{\text{CDP}}^{\text{add}} &= 2\overline{\alpha}\frac{RT}{F}\ln\left(\frac{c_{\text{sp}}}{c_{\text{el}}}\right) + E_{\text{c},0} - \frac{i}{C}t - i\left(\frac{r_{\text{AEM}}}{1-\beta} + \frac{r_{\text{CEM}}}{1-\beta} + \frac{\rho_{\text{c}}h_{\text{c}}}{\epsilon^2}\right) \\
E_{\text{CDP}}^{\text{remove}} &= 2\overline{\alpha}\frac{RT}{F}\ln\left(\frac{c_{\text{sp}}}{c_{\text{el}}}\right) + E_{\text{c},0} - \frac{i}{C}t - i\left(\frac{r_{\text{AEM}}}{1-\beta} + \frac{r_{\text{CEM}}}{1-\beta} + \frac{\rho_{\text{d}}h_{\text{d}}}{\epsilon^2}\right) \\
E_{\text{MCDI}}^{\text{add}} &= 2\overline{\alpha}\frac{RT}{F}\ln\left(\frac{c_{\text{sp}}}{c_{\text{el}}}\right) + E_{\text{c},0} + \frac{i}{C}t - i\left(\frac{r_{\text{AEM}}}{1-\beta} + \frac{r_{\text{CEM}}}{1-\beta} + \frac{\rho_{\text{d}}h_{\text{d}}}{\epsilon^2}\right) \\
E_{\text{MCDI}}^{\text{remove}} &= 2\overline{\alpha}\frac{RT}{F}\ln\left(\frac{c_{\text{sp}}}{c_{\text{el}}}\right) + E_{\text{c},0} + \frac{i}{C}t - i\left(\frac{r_{\text{AEM}}}{1-\beta} + \frac{r_{\text{CEM}}}{1-\beta} + \frac{\rho_{\text{c}}h_{\text{c}}}{\epsilon^2}\right).
\end{aligned}
\tag{2.32}
$$

The switching of solutions in the flow channel is set to occur when the total potential reaches zero. Fig. 2.7 shows the total potential as a function of time, given constant current for two cycles for CDP and MCDI.

(a) **(b)**
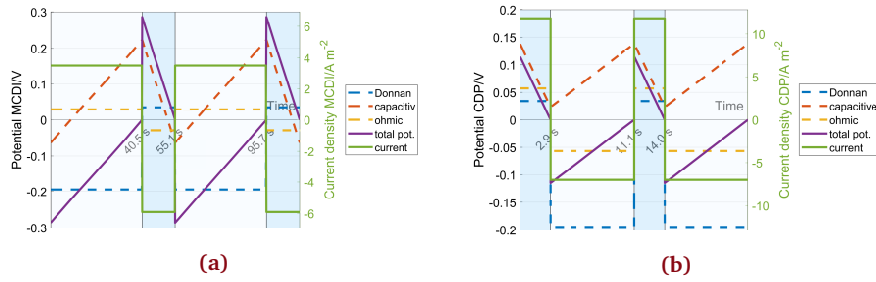
Fig. 2.7: Potential with respect to time in MCDI (a) and CDP (b) for two cycles. Light color indicates a dilute solution, where ions are added to the pores in the electrodes for MCDI and removed in CDP. Dark color indicates a concentrated solution, where ions are removed from the electrode pores for MCDI and added for CDP.

Similarly to the two other SGESS, the current density for discharging set to maximise the power density. This is given in Eq. (2.33):

$$
\begin{aligned}
i_{\text{CDP}}^{\text{add}} &= \frac{E_{\text{Donnan}} + E_{\text{c},0}}{2t^{\text{add}}/C^{\text{add}} + 2r_{\Omega,\text{CDP}}^{\text{add}}} \\
i_{\text{CDP}}^{\text{remove}} &= \frac{E_{\text{Donnan}} + E_{\text{c},0}}{2t^{\text{remove}}/C^{\text{remove}} + 2r_{\Omega,\text{CDP}}^{\text{remove}}},
\end{aligned}
\tag{2.33}
$$

To keep the analogy to the two other SGESS, with fixed current density and water flux with time, comparable conditions are assumed for CESS. The maximum power density and corresponding current density is determined graphically from plots generated by varying t^{add} and t^{remove} in Eq. (2.33). This is illustrated in Fig. 2.8.
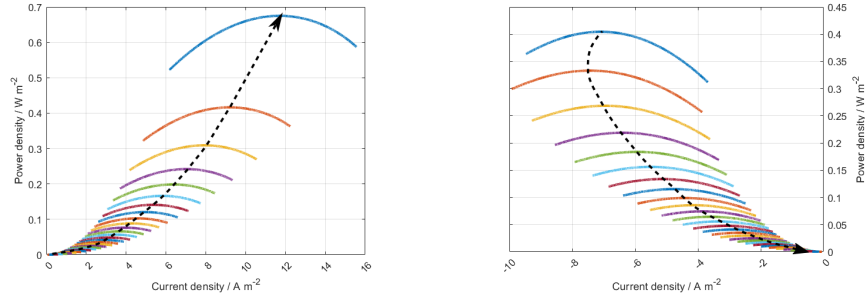
Fig. 2.8: The power density is plotted versus current density to find the peak power current density in CDP. (a) shows the power density while adding ions to the electrodes and (b) shows the power density while removing the ions from the electrode. The arrow indicates direction of increasing concentration.

The discharging current is half of the charging current and vice versa:

$$
\begin{aligned}
i_{\mathrm{MCDI}}^{\mathrm{add}} &= -\frac{i_{\mathrm{CDP}}^{\mathrm{remove}}}{2} \\
i_{\mathrm{MCDI}}^{\mathrm{remove}} &= -\frac{i_{\mathrm{CDP}}^{\mathrm{add}}}{2},
\end{aligned}
\tag{2.34}
$$

The time average of the power density between adding and removing ions from the electrodes, in both CDP and MCDI, is:

$$
\overline{P} = \frac{1}{\Delta t} \int_{t_1}^{t_2} P \, dt = \frac{1}{\Delta t^{\mathrm{add}} + \Delta t^{\mathrm{remove}}} \left(\int_{t_1^{\mathrm{add}}}^{t_2^{\mathrm{add}}} P^{\mathrm{add}} dt + \int_{t_1^{\mathrm{remove}}}^{t_2^{\mathrm{remove}}} P^{\mathrm{remove}} dt \right),
\tag{2.35}
$$

where $\Delta t^{\mathrm{add}} = t_2^{\mathrm{add}} - t_1^{\mathrm{add}}$ and $\Delta t^{\mathrm{remove}} = t_2^{\mathrm{remove}} - t_1^{\mathrm{remove}}$ are the times required to add and remove ions from the electrodes respectively before reaching zero potential.

The reversible power density in CESS is the product of the reversible/driving potential and the current density:

$$\overline{P}_j^{\text{rev}} = \frac{1}{\Delta t} \int_{t_1}^{t_2} i_j (E_{\text{Donnan}} + E_{\text{c}}) dt \tag{2.36}$$

2.2.4 Energy Efficiency of the Three SGESS

The energy density from each of the three SGESS, W_i, is the integrated power density over the total time, t:

$$W = \int_0^t P(t) dt = \overline{P} \Delta t \tag{2.37}$$

$\overline{P}$ is the time average of the power density and t is the total processing time for each system.

For the EESS, the efficiency for charging and discharging, and the total round-trip efficiency, is given in Eq. (2.38). The energy is found by integration as shown in Eq. (2.37), and the pumping energy is given in the papers.

$$\eta_{\text{charging}}^{\text{EESS}} = \frac{W_{\text{charging}}^{\text{rev}}}{W_{\text{pump}} + W_{\text{charging}}}$$

$$\eta_{\text{discharging}}^{\text{EESS}} = \frac{W_{\text{discharging}}^{\text{peak}} - W_{\text{pump}}}{W_{\text{discharging}}^{\text{rev}}} \tag{2.38}$$

$$\eta_{EESS} = \eta_{\text{charging}}^{\text{EESS}} \eta_{\text{discharging}}^{\text{EESS}} = \left(\frac{W_{\text{discharging}}^{\text{peak}} - W_{\text{pump}}}{W_{\text{charging}} + W_{\text{pump}}} \right) \left(\frac{i_{\text{charging}}}{i_{\text{discharging}}} \right),$$

Converting the maximum power density from EESS given in Eq. (2.17) and (2.18) to energy density defined in Eq. (2.37), and using $i_{\text{charging}} = 0.5 \times i_{\text{discharging}}^{\text{peak power}}$ (following from the duck-curve), the the maximum efficiency for charging the EESS is 4/5, while the maximum efficiency for discharging the EESS is 1/2. It follows that the maximum round-trip efficiency of the EESS is 0.4.

For the OESS, the efficiency for charging and discharging, and the total round-trip efficiency, is demonstrated in Eq. (2.39).

$$
\begin{aligned}
\eta_{\text{charging}}^{\text{OESS}} &= \frac{W_{\text{charging}}^{\text{rev}}}{(W_{\text{pump}} + W_{\text{charging}})} \\
\eta_{\text{discharging}}^{\text{OESS}} &= \frac{(W_{\text{discharging}}^{\text{peak}} - W_{\text{pump}})}{W_{discharging}^{\text{rev}}} \\
\eta_{\text{OESS}} &= (\frac{W_{\text{discharging}}^{\text{peak}} - W_{\text{pump}}}{W_{\text{charging}} + W_{\text{pump}}}) \left(\frac{J_{\text{charging}}}{J_{\text{discharging}}} \right),
\end{aligned}
\tag{2.39}
$$

Converting the maximum power density from OESS given in Eq. (2.23) to energy density (Eq. (2.37)), and substituting J_{charging} with $0.5 \times J_{\text{discharging}}^{\text{peak power}}$ (following from the duck-curve), the the maximum efficiency for charging the OESS is 4/5 and the maximum efficency for discharging the OESS is 1/2. It follows that the maximum round-trip efficiency of the OESS is 0.4.

Corresponding to the other technologies, the relevant efficiencies in CESS are given as Eq. (2.40):

$$
\begin{aligned}
\eta_{\text{charging}}^{\text{CESS}} &= \frac{W_{\text{charging}}^{\text{rev}}}{W_{\text{charging}} + W_{\text{pump}}} \\
\eta_{\text{discharging}}^{\text{CESS}} &= \frac{W_{\text{discharging}}^{\text{peak}} - W_{\text{pump}}}{W_{\text{discharging}}^{\text{rev}}} \\
\eta_{\text{CESS}} = \eta_{\text{charging}}^{\text{CESS}} \, \eta_{\text{discharging}}^{\text{CESS}} &= \frac{W_{\text{discharging}}^{\text{peak}} - W_{\text{pump}}}{W_{\text{discharging}}^{\text{rev}}} \frac{W_{\text{charging}}^{\text{rev}}}{W_{\text{charging}} + W_{\text{pump}}}
\end{aligned}
\tag{2.40}
$$

Neglecting the pumping losses, the maximum efficiency can be found to be equal to the other technologies, i.e. 0.5 for discharging, 0.8 for charging and 0.4 for the round-trip efficiency.

2.3 Separation Techniques

As described in the previous sections, external power is used to increase the concentrations difference between the two outlet solutions. However, the separation of the streams can also be done with phase change, adding and removing thermal energy. Two processes using waste heat are suggested in this thesis; water evaporation and salt precipitation. The motivation for using thermal energy is the availability of

waste heat from industry, as mentioned in the introductions; particularly in Norway where this work is conducted.

The two techniques are explained briefly below. Neither of the techniques are tested experimentally, but one challenge with the precipitation system is addressed by measurements, and calculation of the hydrogen production and energy demands is conducted for both systems.

2.3.1 Water Evaporation

In the evaporation process the concentrated outlet solution from RED is decompressed to evaporate water at room temperature. Before compressing the steam back to atmospheric pressure, the steam is heated to avoid condensation in the compressor. The thermal energy in the high-temperature steam can then be used to heat the decompressed concentrated solution through a heat exchanger, resulting in condensation of the steam. This heat exchanger is needed due to a drop in temperature as water evaporates; thus, more thermal energy is required to continue the evaporation. The water is added back to the dilute outlet solution from RED, and the concentrated outlet solution is circulated back to the RED stack; the net result of the process is an increased concentration difference between the two solutions. A schematic of a separation system using evaporation is shown in Fig. 2.9.
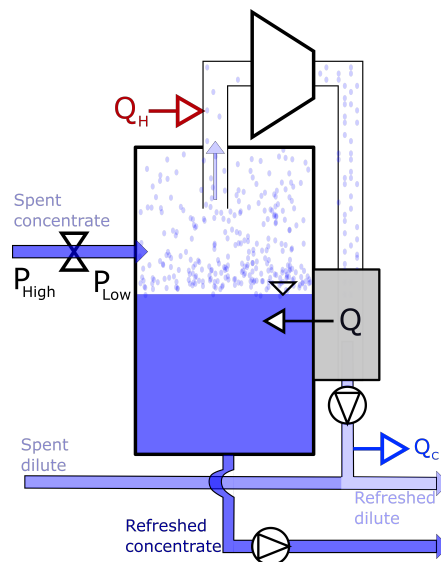
Fig. 2.9: Sketch of principle of separation by evaporation

The energy needed for maintaining the evaporation in this technique is substantial. However; assuming the thermal energy would be lost if not used, the energy input can be neglected.

The concentration difference between the inlet solutions have no restraint due to the separation system, and the limitation is therefor on the resistance of the dilute inlet solutions and the solubility of the inlet concentrated solution.

2.3.2 Salt Precipitation

In the precipitation process thermal energy is removed from the dilute outlet solution from RED to precipitate salt. The salt is then transported from the dilute solution and added to the concentrated outlet solution from RED using an Archimedes pump or screw pump based transport unit. To reduce losses, the energy removed from the dilute outlet solution can be added back to the refreshed dilute solution, after the salt slurry is removed. However, some heat needs to be added to the concentrated solution to heat and dissolve the newly added salt and water. An illustration of the precipitation system is given in Fig. 2.10.
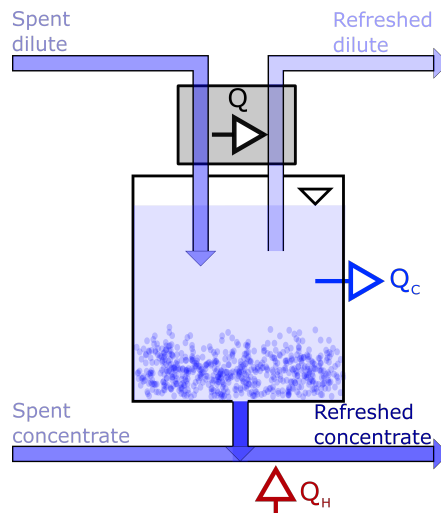
Fig. 2.10: Sketch of principle of separation by precipitation

The solubility of the salt determines the choice of concentration for the precipitation system. The inlet concentration should be at the solubility limit of the operating temperature in RED (40 °C due to the membranes), while the dilute concentration needs to be higher than the solubility at the temperature of the cooled dilute outlet solution. If the dilute concentration is lower than this limit, no salt will be removed

in the precipitation process. To minimise energy consumption while cooling, natural cooling systems can be used, e.g. seawater, at a temperature around 10 °C.

For NaCl the solubility changes with less than 0.5 g L^{-1} from 10 to 40 °C (see Fig. 2.11) corresponding to 0.004 V per unit cell. With this unit cell potential, the RED stack needs to have (theoretical) 290 unit cells to potentially split water. Due to the small change in solubility other salts were considered for use with the precipitations process, where KNO$_3$ had a change in solubility from 250 to 650 g L^{-1} (see Fig. 2.11), corresponding to 0.05 V per unit cell. With this unit cell potential, the RED stack needs to have ten times fewer unit cells than if NaCl is to be used.
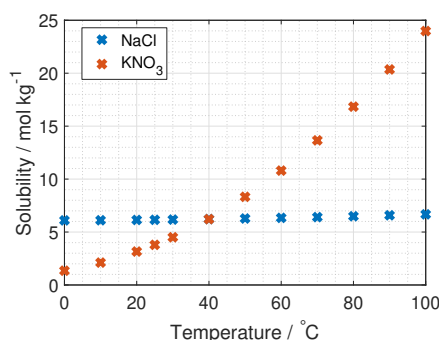
Fig. 2.11: Solubility of KNO$_3$ and NaCl at different temperatures.

2.4 Hydrogen Production with RED

The theoretical potential in one RED unit cell at 25 °C using seawater and river water is 0.14 V (see Eq. (2.1)), where stacking multiple unit cells increases the electrode potential. If the potential is raised over the potential needed for splitting water, hydrogen can be produces at the cathode [72], [73]. The electrode reactions are as follow:

$$\text{Anode: } 4\text{OH}^- \rightarrow 2\text{H}_2\text{O} + \text{O}_2 + 4\text{e}^-$$
$$\text{Cathode: } 4\text{H}_2\text{O} + 4\text{e}^- \rightarrow 2\text{H}_2 + 4\text{OH}^-$$

$$(2.41)$$
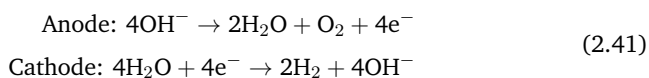
Hydrogen has been produced from RED earlier. Tufa et al. combined RED with an alkaline polymer electrolyte water electrolysis for a hydrogen production of 50 cm^3 h^{-1} cm^{-2} [74], and Raka et al. did an economical evaluation of hydrogen production with RED using amonium bicarbonate [75].

Methodology

Important factors affecting the driving potential, peak power and peak power current density of the SGESS are the permselectivity and the ohmic resistance, where the membrane resistance is a significant part of the stack resistance. Methods for measuring theses factors are described in this chapter. Operating conditions like flow, electrode kinetics and transport phenomena are investigated from EESS stack measurements, whose methodology is included at the end of this chapter.

3.1 Permselectivity

The membrane being analysed was placed between two glass containers, while rubber rings on each side of the membrane prevented leakage. Two solutions with different salt concentrations were added to the glass containers and stirred with magnetic stirrers throughout the experiments. A salt bridge was placed in each glass container, with half of each salt bridge containing 3 M KCl agar and the other half being filled with solution from the glass container. The end of the salt bridge containing the agar was placed in a saturated KCl solution together with a double-junction Ag/AgCl reference electrode. The permselectivity setup can be seen in Fig. 3.1.
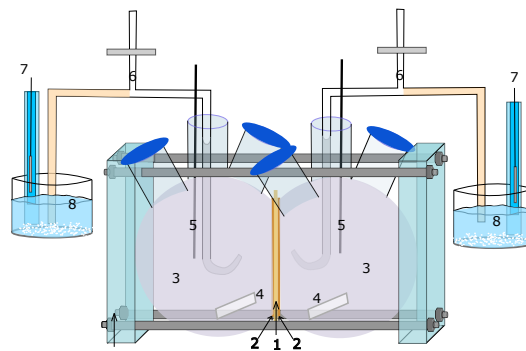
Fig. 3.1: The setup used for measuring the permselectivity of membranes, inspired by [27]. In the figure 1) is the membrane, 2) are the sealing rings, 3) are the glass containers with solutions, 4) are the magnets for stirring, 5) are the thermometer, 6) are the Agar/KCl-salt bridges, 7) are the double junction Ag/AgCl reference electrodes and 8) are the saturated KCl solutions.

The OCV was measured for a minimum of one hour between the reference electrodes by a 5000E Interface Gamry Potentiostat. The measured potential was divided by the available theoretical potential given in Eq. (2.1) (divided by 2 to represent the potential across one membrane).

3.2 Membrane Ion Conductivity

The membranes tested in this work (FAS-50 and FKS-50 from Fumatech [28], [29]) were delivered dry with Br^- and H^+ as counterions. These ions were substituted by soaking the membranes in large containers with a solution containing the ions of interest for at least 48 hours. The containers were kept in a temperature regulated cabinet holding the desired temperature.

The setup used for measuring ion conductivity was developed in-house, and membrane conductivities were tested for known conductivities and compared to literature. For further details concerning the ion conductivity test see [76]. An illustration of the setup is given in Fig. 3.2, where the membranes are placed between two platinum disk electrodes of area 3.14 cm^2 and thickness of 1 mm. Platinum wires connect the platinum disk electrodes to the potentiostat, with hard polyester shells protecting the wires. The design of the setup is close to what is used in literature [77], [78].
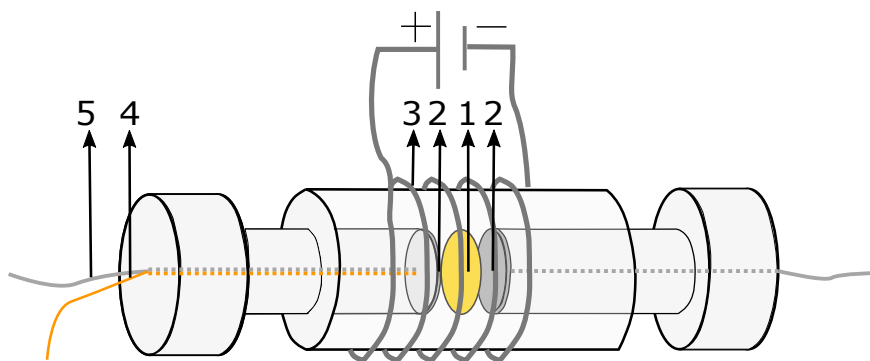
Fig. 3.2: The cell used for measurements of conductivity. In the figure 1) is the membrane, 2) are the platinum disc electrodes, 3) is the heating coil, 4) is the thermocouple and 5) are the platinum wires connecting the disc electrodes to the potentiostat.

The pressure on the membrane was equal in each test. Constant pressure was achieved by placing the setup in a holder with a screw-clamp on a bolt at one end. A torque wrench was used to fix the torque in each experiment.

A thermocouple was in contact with one of the platinum disks to control the temperature. At 40 °C the setup was placed in a heating cabinet, but for increased effect, a heating coil was added to the setup (see Fig. 3.2).

The thickness of the membranes was measured three places on the membrane right after they were removed from the solution. Before placing the membranes in the measurement setup, they were dipped in the solution to prevent drying. When pressure was applied, excess solution flowed out of the cell shell.

The bulk resistance of the membrane was established using electrochemical impedance spectroscopy (EIS) with a Gamry 5000E Interface potentiostat (see Sec. 3.2.1). Three tests were carried out to examine stability. An impedance test over the cell without the membrane follows each test of membranes, to eliminate the impedance of the electrodes and wires, and the internal inductance in the potentiostat.

The impedance of the blank cell (without membrane) was subtracted from the impedance of the cell with the membranes, using Impedance Subtraction software from Gamry Analyst. The membrane resistance was found as described in Sec. 3.2.1.

Each membrane type was measured with 1, 3 and 5 membranes in the cell, subsequently the area resistance is plotted versus the total membrane thickness of the membranes measured. The slope of the curve gives the membrane resistivity, with the membrane conductivity being the inverse of this resistivity.

Between each experiment (1, 3 and 5 membranes) the electrodes were polarised between 0.1 and 1.6 V_{SHE} until a stable polarisation curve was achieved or for a minimum of 30 cycles. The platinum electrodes were polished in case of non-stabilising polarisation curves.

3.2.1 Electrochemical Impedance Spectroscopy

Electrochemical impedance spectroscopy is an analysis technique where the current (or voltage) oscillates at a certain frequency, and the amplitude and phase shift of the potential (or current) is measured. From this data the impedance of the system can be obtained.

A system consisting of two electrodes separated by a membrane has three main contributors to the impedance: Two electrode-membrane interfaces and the impedance of the membrane. The electrode-membrane interface consists of a double layer capacitance, but the double layer is not a perfect capacitor and are therefor usually

represented by a constant phase element (CPE) in the equivalent circuits [79]. The impedance from a CPE is:

$$Z_{\text{CPE}}(w) = \frac{1}{(iwC_{\text{dl}})^n},$$
(3.1)

were w is the frequency, C_{dl} is the double layer capacitance and n represent the degree of deviation from a perfect capacitor (between 1/2 and 1, where $n = 1$ is a pure capacitor).

The membrane contributes to the impedance with a bulk resistance, R_{b}, in parallel with a capacitor, C_{b}, representing the double layer in the pores and cavities inside the membrane. The impedance from the membrane is given as:

$$Z_{\text{mem}}(w) = \left(\frac{1}{R_{\text{b}}} + iwC_{\text{b}}\right)^{-1}.$$
(3.2)

The total impedance of the system is:

$$Z(w) = \left(\frac{1}{R_{\text{b}}} + iwC_{\text{b}}\right)^{-1} + \frac{1}{(iwC_{\text{dl}})^n}.$$
(3.3)

Plotting the real and imaginary part of Eq. (3.3), gives the Nyquist plot in Fig. 3.3
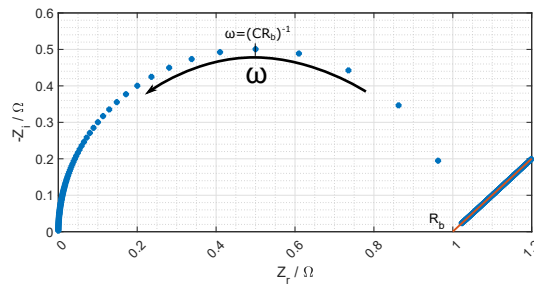
Fig. 3.3: The theoretical Nyquist plot of two electrodes separated by a membrane. The equation for the plot is given in Eq. (3.3), where R_{b} is the bulk resistance of the membrane. (In the figure $R_{\text{b}}=1$, $C_{\text{b}}=10^{-6}$, $C_{\text{dl}}=1$ and $n=0.5$.)

At low frequencies, the electrode-membrane interface dominates the impedance, shown as a straight line. At increased frequency, the double layer at the electrode will be similar to a well-conducting wire, and the impedance of the membrane is

the only contributor. At high frequencies (around 1 MHz), the capacitor effects from the membrane dominate the impedance response [79]. To find the bulk resistance of the membrane, the frequency should be varied, and the result can be read from where the impedance is (close to) the real axis (see R_b in Fig. 3.3).

The setup used for the EIS measurements is provided in Tab. 3.1.

Tab. 3.1: EIS settings for the potentiostat

Variable	Value
AC current [A rms]	**0.001**
DC current [mV rms]	**0**
Initial frequency [Hz]	**1 000 000**
Final frequency [Hz]	**5**
Points/decade	**10**

3.3 Stack Measurements

Stack measurement of the EESS was carried out with an ED stack from Fumateck (ED-40). The stack contained FAS-50 and FKS-50 membranes separated by a combined layer functioning as a spacer (polyester) and gasket (polyvinyl chloride), and electrodes of titanium and iridium plasma coated stainless steel. The stack was pressed together by two endplates of polyether ether ketone (PEEK). An illustration of the setup is shown in Fig. 3.4.
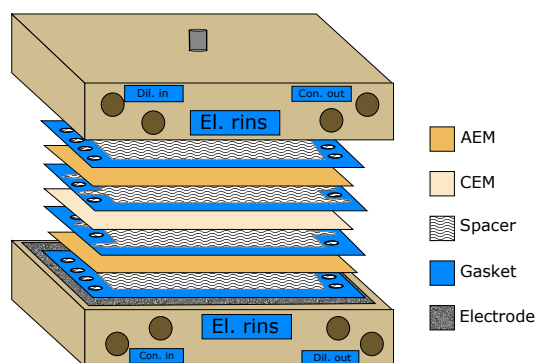
Fig. 3.4: The EESS cell stack and the connection to the potentiostat.

The dilute and concentrated solutions entered the stack through two separate openings at the endplate. Inside the cell, the solutions entered the flow compartments through two holes, and the spacer distributes the solutions over the membranes. Every second spacer had an opening to let either the dilute or the concentrated solution enter the flow compartment, resulting in alternating dilute and concentrated

solutions in the compartments. Both solutions emerge from the cell through two holes at the opposite end plate (see Fig. 3.4). The redox solution, which enters the electrode flow compartments through two different holes, is distributed over the electrodes by a spacer and leave the cell on the opposite side of the electrode from where it entered (same side of the stack).

The ED-40 cell was delivered with a NaCl solution, therefore no substitution of ions in the membranes was necessary. Before each experiment, the solutions to be tested was circulated in the cell until a stable OCV was obtained.

Linear sweep voltammetry (LSV) [80, p.178] was used to record the current at different voltages. The current-voltage curve was used to find the OCV and the ohmic resistance of the RED-stack. Chronopotentiometry measurements of the cell containing the electrodes, redox solution and one AEM was carried out to compensate for the potential losses at the electrode. The current steps were randomised and maintained for 1000 s. Between every current step, the current was set to zero for 100 s. At the end of every step, the resistance was found by dividing potential by the current. The resistance was plotted versus the current density to find the ohmic region and its ohmic resistance, R_{blank}. The unit cell potential is then found from

$$E_{\text{uc}} = \frac{E_{\text{total}} - R_{\text{blank}} \times I}{N} \tag{3.4}$$

where E_{total} is the total stack potential, R_{blank} is the total resistance of the wires, electrodes redox-solution and one AEM, I is the current (A) and N is number of unit cells.

Paper Summaries

<div style="text-align: right">4</div>

4.1 Paper I

In paper I three SGESSs are presented, namely the combination of RED and ED, PRO and RO, and CDP and MCDI. All of these membrane systems can be used to store large quantities of energy in the form of two solutions with different salt concentrations. Mathematical models are used to determine the influence of temperature, concentration and residence time on the power densities and efficiencies of the SGESSs. The paper also includes a brief economical analysis of the three systems.

The driving potentials were found to increase with rising temperature and concentration difference for all three SGESS. The contribution to the driving potential in EESS is purely from the Donnan potential, while the driving potential in CESS also has a contribution from the capacitive potential between the porous electrodes which separates each unit cell. The driving force in OESS is the osmotic pressure over the membranes. For EESS and CESS the maximum driving potential per unit cell was found to be 271 mV and 136 mV, and the maximum osmotic pressured per unit cell in OESS was found to be 5.75 MPa.

The ohmic losses (only relevant for EESS and CESS) were found to increase with the concentration difference (due to a decrease in concentration for the dilute solution), but decrease with increasing temperature. The dependency on concentration and temperature is more pronounced for the EESS resistance than the CESS resistance, due to the substantial contribution from the unit cell electrode resistance in CESS which is affected by neither the temperature nor the concentration.

Peak power density was calculated from the driving potentials and pressure, and the ohmic and water permeability losses. The results are given in Tab. 4.1. The pumping losses are calculated using the flow channel geometry, flow velocity and viscosity of the solutions. From the power densities and the pumping losses, the efficiencies for the three SGESS are calculated and given in Tab. 4.1.

The calculation of the power density is used for a cost evaluation for each technology, presented in Fig. 4.1. There is a threshold for the cost of different membranes at 5.2, 3.7 and 0.43 \$ m^{-2} for the EESS, OESS and CESS respectively.

Tab. 4.1: Peak power densities and total efficiencies from all three SGESSs (maximum efficiencies are 0.4)

T	P_{RED}^{max}	P_{PRO}^{max}	P_{CDP}^{max}	$\eta_{ED\text{-}RED}^{Pmax}$	$\eta_{RO\text{-}PRO}^{Pmax}$	$\eta_{MCDI\text{-}CDP}^{Pmax}$
°C	W m^{-2}	W m^{-2}	W m^{-2}	#	#	#
10	3.18	4.36	0.403	0.390	0.393	0.364
25	4.69	4.83	0.503	0.395	0.396	0.379
40	6.28	5.33	0.593	0.397	0.397	0.387
60	8.54	6.04	0.708	0.399	0.398	0.393
80	11.0	6.78	0.823	0.399	0.399	0.395

Fig. 4.1: Cost of electric energy generation ($ kWh^{-1}) for RED, PRO and CDP at 25 °C and 60 °C compared to the energy price in EU and USA. Residence time is 20 s.

Paper I concludes that there is a comparable power output at room temperature for the EESS and the OEES, while the CEES is 10 % of their output. The EESS outranks the OESS using solutions at temperatures exceeding 40 °C, since the power output increases by a factor of 3 from 10 °C to 80 °C, while the OESS and the CESS increasing by a factor of 2. The reason for the increase in power with temperature is an increase in the OCV (EESS and CESS) and the osmotic pressure (OESS) and the reduction in the ohmic resistance (EESS and CESS) in the cell. The water permeability of the osmotic membranes is also affected by the temperature (see Section 2.2.2), however this is not taken into consideration for the model. The viscosity is also reduced with rising temperature, decreasing the pumping losses for all three systems. Reducing the residence time by a factor 10 reduces the pumping losses by a factor of 100. By increasing the temperature from 25 °C to 40 °C, the osmotic membrane price can be 25 % higher and still be economically viable, while the ionic exchange membrane for the EESS and CESS can be 80 % and 40 % higher and still be economically viable. There is a need for a significant reduction of the membrane cost in all mentioned SGESS.

4.2 Paper II

Paper II presents two separation methods for the outlet solutions from RED using low-grade energy (waste heat). The first method is precipitation of salt by lowering the temperature of the solution. The precipitated salt is removed from one solution and added to another, increasing the concentration difference between the solutions. Waste heat is used to dissolve the salt and to heat the total solution to the operation temperature in RED. The second separation technique is to use waste heat to evaporate water from the outlet concentrated solution and add the water to the spent dilute solution, increasing the concentration difference. The two separation techniques are shown in Fig. 2.9 and 2.10 in Section 2.3.

For the precipitation process, a salt with a pronounced SCTD is needed to achieve a high concentration difference between the solutions. The most common salt in RED, NaCl, has a low SCTD, while the salt KNO_3 show higher SCTD values. One of the most significant contributors to the potential losses in RED is the ohmic resistance, where the membrane resistance contributes the most. Therefore membrane conductivity measurements are carried out with KNO_3 and compared to NaCl for the same membranes. The measured membrane conductivities are given in Fig. 4.2.
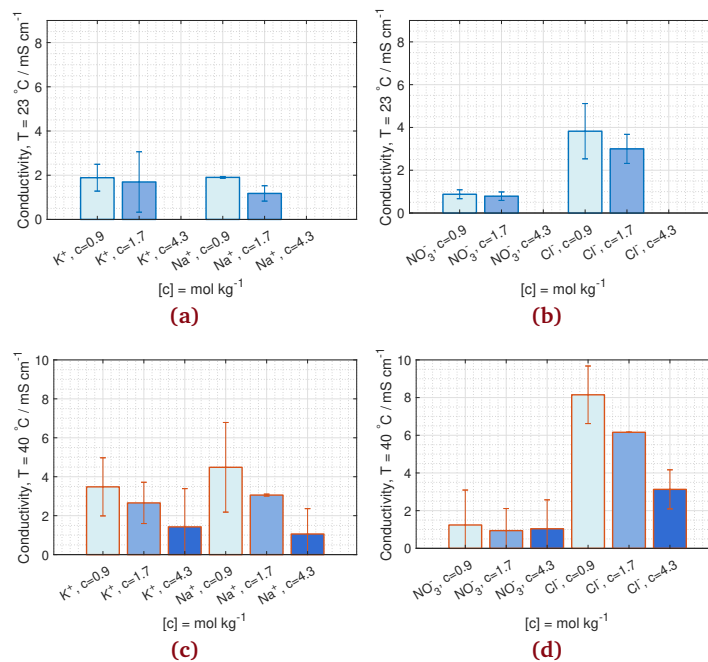
Fig. 4.2: Ion conductivity at 23 °C in a) CEM and b) AEM, and at 40 °C in c) CEM and d) AEM, with 95 % confidence interval.

The conductivity of KNO_3 in CEM was similar to NaCl, while the conductivity of KNO_3 in AEM was significantly lower than of NaCl in AEM. Temperature dependence was only visible for NaCl due to too large deviations in KNO_3 using 95 % confidence interval.

The resistances and the relevant concentrations are used for modelling the OCV and the hydrogen productions from RED. At 40 °C the OCV was found to be 0.18±0.03 V and 0.06±0.01 V for concentrations relevant for the evaporation and precipitation process respectively. The measured membrane resistance, together with the modelled stack resistance and calculated OCV, corresponds to the hydrogen production at peak power current density given in Fig. 4.3. A simplified cost analysis, including the cost of the membrane and the salt, show that the cost per kg hydrogen produced is 56 \$ and 370 \$ for the evaporation and precipitation system.
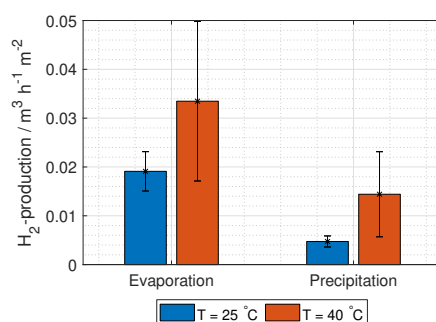
Fig. 4.3: The modelled hydrogen production from RED at peak power current density using concentrations relevant for the precipitaiton and the evapoartion processes.

Paper II also includes an energy evaluation of RED with precipitation and evaporation per mass and volume hydrogen produced. For this analysis the mass flow of solution, salt and water is calculated for each process, and the energy required for separation is calculated. The modelled energy consumption per volume hydrogen produced was found to be 55±22 kWh m^{-3} (700±300 kWh kg^{-1}) for RED using evaporation, which exceeds the energy requirement of PEMWE or alkaline water electrolysis by a factor of 10. The energy consumption per volume hydrogen produced by RED using precipitation is 8.23±0.05 kWh m^{-3} (104.8±0.6 kWh kg^{-1}) which is similar to the energy consumption in PEMWE and alkaline water electrolysis. A significant advantage of the Heat to H_2 system, compared to PEMWE and alkaline electrolysis, is its use of low-grade energy which has limited other applications.

4.3 Paper III

Paper III presents measurements of an energy storage system where RED and ED is combined into an EESS. The EESS is a closed system, where the concentrations can be higher than that of naturally occurring concentrations (e.g. seawater at 0.5 M).

Most research on AEM and CEM to RED or ED is carried out at room temperature and using seawater concentrations. This article presents data from permselectivity measurements of NaCl concentration close to saturation point. The data from the measurements are given in Fig. 4.4.
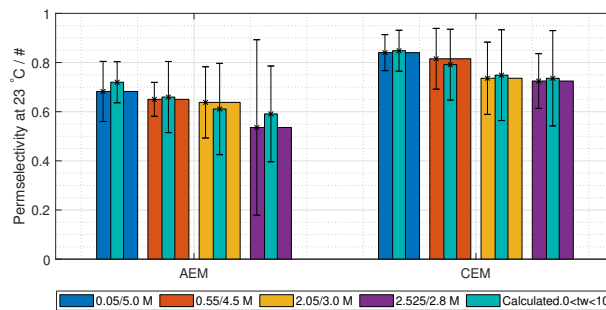
Fig. 4.4: Measured permselectivity of AEM and CEM at 23 °C with 95 % confidence interval. The calculated permselectivities are with water transport number ranging from 0 to 10, and salt transport numbers equal to Długołecki et al. [31].

Measurements show that the mean permselectivity (between AEM and CEM) decreases from 0.95 using seawater, to mean permselectivities ranging from 0.6 to 0.8 using concentration ratios from 2.800 M/2.525 M to 5.000 M/0.05000 M. The decrease in permselectivity with mean external concentration is affected by the osmotic gradient from the membrane pores to the external solution, decreasing the amount of water in the membrane pores. Less water in the pores leads to less ionic conductivity.

Stack measurements of the EESS were conducted with LSV to find the OCV, the stack resistance and the power density. The losses from pumping and the efficiency of the system were calculated. The OCV at 5.000 M/0.05000 M was measured to 115±9 mV at 25 °C and 118±8 mV at 40 °C. The measured OCV was 50 % of the theoretical OCV ($\alpha = 1$). The peak power density and current density from EESS at 40 °C is given in Tab. 4.2. For the higher concentration differences, the efficiency was 0.4 (compared to the reversible potential).

Tab. 4.2: Peak power current density, peak power density and charging power density at different concentration fractions.

c_c/c_d [M/M]	$i^{\text{dischar.}}$ [A m^{-2}]	$P_{\max}^{\text{dischar.}}$ [W m^{-2}]	$P^{\text{char.}}$ [W m^{-2}]
5.000/0.05000	42±7	2.0±0.3	3.8±0.9
4.500/0.5500	21±2	0.58±0.02	0.8±0.1
3.000/2.050	3±2	0.015±0.008	0.019±0.009
2.525/2.525	0.08±0.09	$(1.2\pm0.4)\times10^{-5}$	$(2.2\pm2.1)\times10^{-5}$

A simple LCA was conducted for the EESS. The storage capacity was set to 1 GWh per day, where extraction was assumed to occur during 2 hours in the evening (duck curve constraint), and a lifetime of 20 years. Using the power density measured in this article and the calculated power losses of pumping, the impact on global warming and the CED for producing each component in the EESS as given in Fig. 4.5.
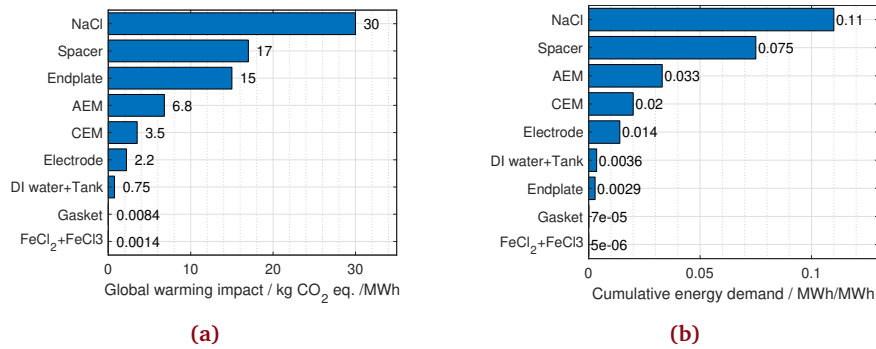
Fig. 4.5: Impact on global warming (kg CO2 eq./MWh) (a) and the CED (MWh/MWh)(b) for each component in the production phase.

The global warming factor was found to be 62-75 kg CO_2 eq. per MWh, which is in the same range as large-scale energy storage with Li-ion batteries (16 and 333 kg CO_2 eq. per MWh [81]–[84]). The cumulative energy demand for the production of EESS is 0.22-0.26 MWh/MWh, mostly lower than the CED from 1 GWh of Li-ion batteries (0.24 to 0.55 MWh/MWh [83]). This study indicates an energy demand for producing the EESS that is the same or smaller compared to the energy demand in Li-ion battery production.

Overall Conclusions

<div style="text-align: right">5</div>

The main objective during this PhD has been to investigate energy storage opportunities using salinity gradient energy and waste heat. Using the energy in salinity gradients and available waste heat for large scale energy storage will help enable the transformation from oil and gas to intermittent renewable energy sources.

By combining a mixing technology (e.g. RED, PRO or CDP) with a desalination technology (e.g. ED, RO or MCDI), electric energy can be stored in salinity gradients for use in periods with low energy production and high energy demands. An EESS and an OESS can produce the same energy per membrane area at room temperature (5 W m^{-2}), while the power density of a CESS is 10 % of the power density of the two other storage systems. If the temperature is increased to 60 °C, the power density of the EESS is 60 % higher than the power density of OESS: 8.54 W m^{-2} for EESS, versus 6.04 W m^{-2} for OESS. With a large amount of waste heat available for heating the solutions in the SGESS, these results show that the EESS will provide the highest power output at elevated temperatures. The output power density of EESS increases with a factor 3 from 10 °C to 60 °C. The results from the modelling were used to determine the maximum cost of membranes for energy production to be economically feasible. The membrane price for EESS needed to be below 5.2 \$ m^{-2} for the system to be economically feasible.

Alternative separation processes for the outlet solutions from RED were investigated and compared. The two methods analysed in this work were the removal of water by evaporation, where the pressure of the concentrated outlet solution from RED was lowered and thermal energy was added to evaporate water, and the removal of salt through precipitation, where thermal energy was removed from the dilute outlet solution from RED to precipitated salt. The evaporation process does not affect which concentrations can be used for the inlet solutions in RED. The precipitation process, however, can only precipitate salt until the solubility limit at the operation temperature of the separation process is reached. Thereby, the two separation methods will produce solutions with different concentrations, and thus the driving potential in RED with the evaporation process will be three times higher than the driving potential in RED using concentrations relevant for the precipitation process (at 40 °C). Due to the demand for a pronounced dependence on saturation concentration temperature in the precipitation process, KNO_3 is recommended to be

used as salt in the process. Conductivity measurements of KNO_3 in IEM are carried out and included in a model to find the power density and hydrogen production of RED using concentrations relevant for the precipitation and evaporation process. The hydrogen production of RED was 2-4 times higher using the evaporation process compared to using concentrations relevant for the precipitation process. However, the energy demand for evaporating water is higher than the energy needed for solution heating and dissolving of salt. The energy demand for the evaporation process per cubic meter of hydrogen produced is 7 times higher than the energy demand per cubic meter hydrogen using the precipitation process. The precipitation process uses 104.8±0.6 kWh per kg of hydrogen, which is comparable to the energy demand in PEMWE or alkaline water electrolysis. A point of interest is the loss of energy quality in PEMWE and alkaline water electrolysis which uses high-grade energy (electricity), as opposed to the low-grade energy input (heat) of the Heat to H_2 system.

An investigation on how raised concentrations of NaCl affect the permselectivity of the membranes and the stack measurements of RED is conducted. Given a closed energy storage system, the concentration used in RED and ED does not need to be naturally occurring like river water and seawater. However, most work conducted on RED and ED is on concentrations and salts found in nature (typically NaCl at 0.5 M). Using concentrations on the saturation limit, the permselectivity is assumed to change due to changed water up-take and the density of fixed charges, among others. The permselectivity for NaCl at concentrations ranging from 2.8 M/2.525 M to 5.0 M/0.05 M ($c_{concenrated}/c_{dilute}$), was measured to 0.5-0.7 for AEM, and 0.7-0.8 for the CEM, while the permselectivity at 0.5 M is reported to be 0.92-0.96 for AEM and 0.97-0.99 for CEM. The OCV of the RED stack was found to be half of the theoretical OCV, and the maximum power density was 2.0±0.3 W m^{-2} at 40 °C.

A closed EESS is a new (2015) method to store large scale energy, and a brief LCA of the system is therefore conducted to investigate how this large scale energy storage system affects the global warming factor and the amount of energy needed in the EESS production per energy produced. For the production of 1 GWh EESS, with an operating life of 20 years, two hours discharging time every day and with optimised spacer material for lowest impact, the global warming factor is 62 kg CO_2 per MWh energy produced. The energy demand in the production of the EESS is 0.22 MWh per MWh energy produced.

Different measurement setups have been built and optimised within this PhD. The permselectivity setup was changed from two closed glass containers to have a flow-through of solution for reducing diffusion effects from the OCV. New containers with flat surfaces at the bottom were made to make the assembly of the cell easier. Reference electrodes were removed from the test-solutions, to prevent interaction

with the experiments, and connected with salt bridges. The electrode preparation for the membrane conductivity setup has been optimised for reproducibility of the measurements. A new cell was constructed for the electrode polarisation, where a closed container with nitrogen gas reduces the amount of impurities in the electrolyte drastically, and the electrodes were stabilised. The electrode preparations were also standardised to be as equal as possible before each experiment. The assembly of an in-house made RED stack was also heavily optimised. Cutting forms, to be used in a punching machine, for membranes, gaskets and spacers were constructed. Temperature control of the solutions inside the RED-stack was implemented, and the temperature was measured by an optical sensor (fibre Bragg grating), and the temperature was found to drop drastically from the inlet solution to the RED flow channel. Consequently, all measurements above room temperature were conducted in a heating cabinet while the temperature was monitored.

The overall goal of this PhD was to find a way to store a large amount of energy so that when renewable, but intermittent, energy sources are utilised in large scale, there will be an environmentally friendly and easy-to-scale way to store the energy. This PhD has shown the potential of three SGESS, pointed at challenges and given sensitivity to operation temperature, residence time and concentration. Thermal separation processes have been analysed for charging the SGESS for areas with available waste heat (e.g. industry areas), and hydrogen has been examined as a product from the SGESS as an alternative to electricity. The work conducted in this PhD has given an overview of the potentials in energy storage by salinity gradients.

Further Work

<div style="text-align: right; font-size: 3em;">6</div>

The permselectivity of the two tested IEMs was lower for NaCl concentrations close to saturation (5 M) compared to the permselectivity measured using concentrations close to seawater (0.5 M). For use in a closed SGESS where high concentrations are beneficial, other IEMs should be tested to find membranes with higher permselectivity. The closed system also opens for using different salts, which could be tested to see if the permselectivity could be improved. The setup to measure permselectivity can be even more optimised, to lower the uncertainty and thereby make it possible to measure the transport number of salt and water. Another factor affecting the permselectivity is the water uptake and the swelling factor. These factors would have been highly interesting to measure if time had been available.

The conductivity of NO_3^- in the AEM tested in this thesis were low compared to the conductivity of Cl^-. A screening test at a relevant concentration could be carried out for various salts with pronounced change in solubility with temperature (e.g $CaCl_2$, NaOH or KI), and for multiple membranes. The membrane resistance was found to have a significant impact on the power density from RED, making it essential to minimise the losses of the membranes. The electrode preparation procedure and the measurement setup are reliable and do not need any immediate improvements.

The model made for the three SGESS gives a good insight into OCV and power output from the systems, and how they vary with concentration and temperature. The calculations in the model are easy to follow; however, they should be extended to include the concentration polarisation, which will give valuable information regarding the ideal flow velocity. The model should also take into consideration the change in solution concentration from inlet to the outlet from the RED-stack, like the model of the mass flow carried out for the hydrogen production system does.

Prototypes of the precipitation process and evaporation should be constructed to verify the mass flow of water and solutions, and to do the next step in the proof of concept started in this PhD. The hydrogen production from a RED stack should also be measured to verify the model.

References

[1] S. R. Weart, *The discovery of global warming*. Harvard University Press, 2008.

[2] International Energy Agency (IEA), *Key World Energy STATISTICS*. International energy agency, 2017.

[3] DNV-GL, *Energy transition outlook 2017*. DNV-GL, 2017.

[4] NVE, *NVE Nasjonal ramme for vindkraft*, 2019.

[5] R. S. Kingsbury, K. Chu, and O. Coronell, „Energy storage by reversible electrodialysis: The concentration battery", *Journal of Membrane Science*, vol. 495, pp. 502–516, 2015.

[6] K. Bradbury, L. Pratson, and D. Patiño-Echeverri, „Economic viability of energy storage systems based on price arbitrage potential in real-time US electricity markets", *Applied Energy*, vol. 114, pp. 512–519, 2014.

[7] B. Dunn, H. Kamath, and J.-M. Tarascon, „Electrical energy storage for the grid: a battery of choices", *Science*, vol. 334, no. 6058, pp. 928–935, 2011.

[8] R. E. Pattle, „Production of electric power by mixing fresh and salt water in the hydro-electric pile", *Nature*, vol. 174, no. 4431, p. 660, 1954.

[9] *What is Blue Energy?*, `https://www.electrochem.org/redcat-blog/what-is-blue-energy/`, Accessed: 2019-07-18.

[10] A. Achilli and A. E. Childress, „Pressure retarded osmosis: From the vision of sidney loeb to the first prototype installation", *Desalination*, vol. 261, no. 3, pp. 205–211, 2010.

[11] M. F. M. Bijmans, O. S. Burheim, M. Bryjak, A. Delgado, P. Hack, F. Mantegazza, S. Tenisson, and H. V. M. Hamelers, „Capmix-deploying capacitors for salt gradient power extraction", *Energy Procedia*, vol. 20, pp. 108–115, 2012.

[12] G. L. Wick, „Power from salinity gradients", *Energy*, vol. 3, no. 1, pp. 95–100, 1978.

[13] N. Y. Yip, D. Brogioli, H. V. M. Hamelers, and K. Nijmeijer, „Salinity gradients for sustainable energy: primer, progress, and prospects", *Environmental science & technology*, vol. 50, no. 22, pp. 12 072–12 094, 2016.

[14] J. W. Post, J. Veerman, H. V. M. Hamelers, G. J. W. Euverink, S. J. Metz, K. Nymeijer, and C. J. N. Buisman, „Salinity-gradient power: Evaluation of pressure-retarded osmosis and reverse electrodialysis", *Journal of Membrane Science*, vol. 288, no. 1-2, pp. 218–230, 2007.

[15] Y. Mei and C. Y. Tang, „Recent developments and future perspectives of reverse electro-dialysis technology: A review", *Desalination*, vol. 425, no. October 2017, pp. 156–174, 2017.

[16] G. Z. Ramon, B. J. Feinberg, and E. M. V. Hoek, „Membrane-based production of salinity-gradient power", *Energy & Environmental Science*, vol. 4, no. 11, p. 4423, 2011.

[17] J. Maisonneuve, P. Pillay, and C. B. Laflamme, „Pressure-retarded osmotic power system model considering non-ideal effects", *Renewable Energy*, vol. 75, pp. 416–424, 2015.

[18] S. Senthil and S. Senthilmurugan, „Reverse Osmosis–Pressure Retarded Osmosis hybrid system: Modelling, simulation and optimization", *Desalination*, vol. 389, pp. 78–97, 2016.

[19] M. M. Fernández, R. M. Wagterveld, S. Ahualli, F. Liu, A. V. Delgado, and H. V. M. Hamelers, „Polyelectrolyte-versus membrane-coated electrodes for energy production by capmix salinity exchange methods", *Journal of Power Sources*, vol. 302, pp. 387–393, 2016.

[20] W. J. van Egmond, U. K. Starke, M. Saakes, C. J. N. Buisman, and H. V. M. Hamelers, „Energy efficiency of a concentration gradient flow battery at elevated temperatures", *Journal of Power Sources*, vol. 340, pp. 71–79, 2017.

[21] Z. Jalili, K. W. Krakhella, K. E. Einarsrud, and O. S. Burheim, „Energy generation and storage by salinity gradient power: A model-based assessment", *Journal of Energy Storage*, vol. 24, p. 100 755, 2019.

[22] P. Denholm, M. OConnell, G. Brinkman, and J. Jorgenson, *Overgeneration from solar energy in california: A field guide to the duck chart*, National Renewable Energy Laboratory, 2015.

[23] S. C. Schlemminger, *From waste heat to a resource*, 2015.

[24] Enova, „Annual report 2009 - results and activities", Enova, 2010.

[25] S. Brueckner, L. Miró, L. F. Cabeza, M. Pehnt, and E. Laevemann, „Methods to estimate the industrial waste heat potential of regions–a categorization and literature review", *Renewable and Sustainable Energy Reviews*, vol. 38, pp. 164–171, 2014.

[26] O. S. Burheim, *Engineering energy storage*. Academic Press, 2017.

[27] A. Zlotorowicz, R. V. Strand, O. S. Burheim, Ø. Wilhelmsen, S. Kjelstrup, Wilhelmsen, and S. Kjelstrup, „The permselectivity and water transference number of ion exchange membranes in reverse electrodialysis", *Journal of Membrane Science*, vol. 523, no. October 2016, pp. 402–408, 2017.

[28] FuelCellStore, *Fumasep fas-50*, 2019.

[29] FuelCellStore, *Fumasep fks-50*, 2019.

[30] C. H. Hamann, A. Hamnett, and W. Vielstich, *Electrochemistry*. Wiley-VCH, 1998.

[31] P. Długołecki, B. Anet, S. J. Metz, K. Nijmeijer, and M. Wessling, „Transport limitations in ion exchange membranes at low salt concentrations", *Journal of Membrane Science*, vol. 346, no. 1, pp. 163–171, 2010.

[32] L. Giorno, E. Drioli, and H. Strathmann, „Water transport in ion-exchange membranes", in *Encyclopedia of Membranes*. Berlin, Heidelberg: Springer Berlin Heidelberg, 2016, pp. 2011–2015.

[33] K. S. Pitzer and R. T. Pabalan, „Thermodynamics of nacl in steam", *Geochimica et Cosmochimica Acta*, vol. 50, no. 7, pp. 1445–1454, 1986.

[34] R. H. Stokes and R. A. Robinson, „Ionic hydration and activity in electrolyte solutions", *Journal of the American Chemical Society*, vol. 70, no. 5, pp. 1870–1878, 1948.

[35] E. Glueckauf, „The influence of ionic hydration on activity coefficients in concentrated electrolyte solutions", *Transactions of the Faraday Society*, vol. 51, pp. 1235–1244, 1955.

[36] R. Pytkowicz, *Activity coefficients in electrolyte solutions*, ser. Activity Coefficients in Electrolyte Solutions v. 2. CRC Press, 1979.

[37] A. C. F. Ribeiro, V. M. M. Lobo, H. D. Burrows, A. J. M. Valente, A. J. F. N. Sobral, A. M. Amado, C. I. A. V Santos, and M. A. Esteso, „Mean distance of closest approach of potassium, cesium and rubidium ions in aqueous solutions: Experimental and theoretical calculations", *Journal of Molecular Liquids*, vol. 146, no. 3, pp. 69–73, 2009.

[38] C. G. G. Malmberg and A. a. A Maryott, „Dielectric constant of water from 00 to 1000 C", *Journal of research of the National Bureau of Standards*, vol. 56, no. 1, pp. 1–8, 1956.

[39] O. Miyawaki, A. Saito, T. Matsuo, and K. Nakamura, „Activity and activity coefficient of water in aqueous solutions and their relationships with solution structure parameters", *Bioscience, biotechnology, and biochemistry*, vol. 61, no. 3, pp. 466–469, 1997.

[40] V. N. Afanasiev, A. N. Ustinov, and I. Y. Vashurina, „State of hydration shells of sodium chloride in aqueous solutions in a wide concentration range at 273.15- 373.15 k", *The Journal of Physical Chemistry B*, vol. 113, no. 1, pp. 212–223, 2008.

[41] G. Onori, „Ionic hydration in sodium chloride solutions", *The Journal of chemical physics*, vol. 89, no. 1, pp. 510–516, 1988.

[42] AMC-Drilling Optimisation, *AMC Salt Tables*, 2017.

[43] Shapley, Patricia - university of Illinois, *Concentrations of Molecular Solutes*, 2011.

[44] A. H. Galama, G. Daubaras, O. S. Burheim, H. H. M. Rijnaarts, and J. W. Post, „Seawater electrodialysis with preferential removal of divalent ions", *Journal of Membrane Science*, vol. 452, pp. 219–228, 2014.

[45] Y. Mei and C. Y. Tang, „Co-locating reverse electrodialysis with reverse osmosis desalination: Synergies and implications", *Journal of Membrane Science*, vol. 539, no. March, pp. 305–312, 2017.

[46] P. Długołęcki, A. Gambier, K. Nijmeijer, and M. Wessling, „Practical potential of reverse electrodialysis as process for sustainable energy generation", *Environmental Science and Technology*, vol. 43, no. 17, pp. 6888–6894, 2009.

[47] J. W. Post, H. V. M. Hamelers, and C. J. N. Buisman, „Energy recovery from controlled mixing salt and fresh water with a reverse electrodialysis system", *Environmental Science and Technology*, vol. 42, no. 15, pp. 5785–5790, 2008.

[48] EXW Foxboro, *CONDUCTIVITY ORDERING GUIDE*, 1999.

[49] Schlumberger, *Resistivity of NaCl Solutions*, 2017.

[50] T. Isono, „Density, viscosity, and electrolytic conductivity of concentrated aqueous electrolyte solutions at several temperatures. alkaline-earth chlorides, lanthanum chloride, sodium chloride, sodium nitrate, sodium bromide, potassium nitrate, potassium bromide, and cadmium nitrate", *Journal of chemical and engineering data*, vol. 29, no. 1, pp. 45–52, 1984.

[51] U. Merten, „Flow relationships in reverse osmosis", *Industrial & Engineering Chemistry Fundamentals*, vol. 2, no. 3, pp. 229–232, 1963.

[52] Z. Amjad, *Reverse osmosis: membrane technology, water chemistry & industrial applications*. Chapman & Hall, 1993.

[53] L. F. Greenlee, D. F. Lawler, B. D. Freeman, B. Marrot, and P. Moulin, „Reverse osmosis desalination: Water sources, technology, and today's challenges", *Water research*, vol. 43, no. 9, pp. 2317–2348, 2009.

[54] F. A. AlMarzooqi, A. A. Al Ghaferi, I. Saadat, and N. Hilal, „Application of capacitive deionisation in water desalination: A review", *Desalination*, vol. 342, pp. 3–15, 2014.

[55] S. Loeb, F Van Hessen, J Levi, and M Ventura, „The osmotic power plant", in *11th Intersociety Energy Conversion Engineering Conference*, 1976, pp. 51–57.

[56] F. Helfer, C. Lemckert, and Y. G. Anissimov, „Osmotic power with pressure retarded osmosis: Theory, performance and trends–a review", *Journal of Membrane Science*, vol. 453, pp. 337–358, 2014.

[57] Reuters - Wojciech Moskwa, *Norway opens world's first osmotic power plant*, 2009.

[58] Z. L. Cheng, X. Li, and T.-S. Chung, „The forward osmosis-pressure retarded osmosis (fo-pro) hybrid system: A new process to mitigate membrane fouling for sustainable osmotic power generation", *Journal of Membrane Science*, vol. 559, pp. 63–74, 2018.

[59] T. Yang, C. F. Wan, J. Xiong, and T.-S. Chung, „Pre-treatment of wastewater retentate to mitigate fouling on the pressure retarded osmosis (pro) process", *Separation and Purification Technology*, 2019.

[60] A. Merdaw, A. Sharif, and G. Derwish, „Water permeability in polymeric membranes, part i", *Desalination*, vol. 260, no. 1-3, pp. 180–192, 2010.

[61] D. Brogioli, „Extracting renewable energy from a salinity difference using a capacitor", *Physical Review Letters*, vol. 103, no. 5, pp. 31–34, 2009.

[62] CAPMIX - Coordinator: Dr. ir. Martijn Bijmans, *The Capacitive Principle*, 2012.

[63] S. Porada, D. Weingarth, H. V. Hamelers, M. Bryjak, V. Presser, and P. Biesheuvel, „Carbon flow electrodes for continuous operation of capacitive deionization and capacitive mixing energy generation", *Journal of Materials Chemistry A*, vol. 2, no. 24, pp. 9313–9321, 2014.

[64] D. D. Caudle, J. H. Tucker, J. L. Cooper, B. B. Arnold, and A Papastamataki, „Electrochemical demineralization of water with carbon electrodes: research and development progress", *United States Department of the Interior*, p. 190, 1966.

[65] Y. Oren, „Capacitive deionization (CDI) for desalination and water treatment - past, present and future (a review)", *Desalination*, vol. 228, no. 1-3, pp. 10–29, 2008.

[66]S. Porada, R. Zhao, A. Van Der Wal, V. Presser, and P. Biesheuvel, „Review on the science and technology of water desalination by capacitive deionization", *Progress in Materials Science*, vol. 58, no. 8, pp. 1388–1442, 2013.

[67]B. B. Sales, M Saakes, J. W. Post, C. J. N. Buisman, P. M. Biesheuvel, and H. V. M. Hamelers, „Direct power production from a water salinity difference in a membrane-modified supercapacitor flow cell.", *Environmental science & technology*, vol. 44, no. 14, pp. 5661–5665, 2010.

[68]R. Rica, R. Ziano, D. Salerno, F. Mantegazza, R. van Roij, and D. Brogioli, „Capacitive mixing for harvesting the free energy of solutions at different concentrations", *Entropy*, vol. 15, no. 4, pp. 1388–1407, 2013.

[69]M. C. Hatzell, R. D. Cusick, and B. E. Logan, „Capacitive mixing power production from salinity gradient energy enhanced through exoelectrogen-generated ionic currents", *Energy & Environmental Science*, vol. 7, no. 3, pp. 1159–1165, 2014.

[70]F. Liu, O. Schaetzle, B. B. Sales, M. Saakes, C. J. N. Buisman, and H. V. M. Hamelers, „Effect of additional charging and current density on the performance of Capacitive energy extraction based on Donnan Potential", *Energy & Environmental Science*, vol. 5, no. 9, pp. 8642–8650, 2012.

[71]O. Burheim, B. B. Sales, O. Schaetzle, F. Liu, and H. V. M. Hamelers, „Auto generative capacitive mixing for power conversion of sea and river water by the use of membranes", in *ASME 2011 International Mechanical Engineering Congress and Exposition*, American Society of Mechanical Engineers, 2011, pp. 483–492.

[72]R. A. Tufa, E. Rugiero, D. Chanda, J. Hnàt, W. van Baak, J. Veerman, E. Fontananova, G. Di Profio, E. Drioli, K. Bouzek, *et al.*, *Journal of Membrane Science*, vol. 514, pp. 155–164, 2016.

[73]Y. Kim and B. E. Logan, *Proceedings of the National Academy of Sciences*, vol. 108, no. 39, pp. 16 176–16 181, 2011. eprint: `http://www.pnas.org/content/108/39/16176.full.pdf`.

[74]R. A. Tufa, J. Hnát, M. Němeček, R. Kodỳm, E. Curcio, and K. Bouzek, „Hydrogen production from industrial wastewaters: An integrated reverse electrodialysis-water electrolysis energy system", *Journal of cleaner production*, vol. 203, pp. 418–426, 2018.

[75]Y. D. Raka, H. Karoliussen, K. M. Lien, and O. S. Burheim, „Opportunities and challenges for thermally driven hydrogen production using reverse electrodialysis system", *International Journal of Hydrogen Energy*, 2019.

[76]E. S. Skilbred, K. W. Krakhella, I. J. M. Haga, J. G. Pharoah, M Hillestad, G del Alamo Serrano, and O. S. Burheim, „Heat to H2: Using Waste Heat to Set Up Concentration Differences for Reverse Electrodialysis Hydrogen Production", *ECS Trans. 2018,* vol. 85, no. 13, pp. 147–161, 2018.

[77]E. Barsoukov and J. R. Macdonald, *Impedance spectroscopy: theory, experiment, and applications*. John Wiley & Sons, 2005.

[78]F. Müller, C. A. Ferreira, D. S. Azambuja, C. Alemán, and E. Armelin, „Measuring the proton conductivity of ion-exchange membranes using electrochemical impedance spectroscopy and through-plane cell", *The Journal of Physical Chemistry B*, vol. 118, no. 4, pp. 1102–1112, 2014.

[79] T. Soboleva, Z. Xie, Z. Shi, E. Tsang, T. Navessin, and S. Holdcroft, „Investigation of the through-plane impedance technique for evaluation of anisotropy of proton conducting polymer membranes", *Journal of Electroanalytical Chemistry*, vol. 622, no. 2, pp. 145–152, 2008.

[80] D. Pletcher, R Greff, R Peat, L. M. Peter, J Robinson, and J Pletcher, Derek and Greff, R and Peat, R and Peter, LM and Robinson, *Instrumental methods in electrochemistry*. Elsevier, 2001.

[81] L. A.-W. Ellingsen, C. R. Hung, and A. H. Strømman, „Identifying key assumptions and differences in life cycle assessment studies of lithium-ion traction batteries with focus on greenhouse gas emissions", *Transportation Research Part D: Transport and Environment*, vol. 55, pp. 82–90, 2017.

[82] H. C. Kim, T. J. Wallington, R. Arsenault, C. Bae, S. Ahn, and J. Lee, „Cradle-to-gate emissions from a commercial electric vehicle li-ion battery: A comparative analysis", *Environmental science & technology*, vol. 50, no. 14, pp. 7715–7722, 2016.

[83] R. Arvidsson, M. Janssen, M. Svanström, P. Johansson, and B. A. Sandén, „Energy use and climate change improvements of li/s batteries based on life cycle assessment", *Journal of Power Sources*, vol. 383, pp. 87–92, 2018.

[84] C. Samaras and K. Meisterling, *Life cycle assessment of greenhouse gas emissions from plug-in hybrid vehicles: Implications for policy - supporting online information*, 2008.

Part II

Papers

This part of the thesis contains the three papers conducted during this PhD work:

1. Z. Jalili, K.W. Krakhella, K. E. Einarsrud and O.S. Burheim, "Energy Generation and Storage by Salinity Gradient Power: A Model-Based Assessment", *Journal of Energy Storage, vol. 24, 2019*

2. K.W. Krakhella, R. Bock, F. Seland, O.S. Burheim and K. E. Einarsrud. "Heat to h2: Using waste heat for hydrogen production through reverse electrodialysis", *Journal of Energies, 12(18):3428, 2019*

3. K.W. Krakhella, M. A. M. Arancibia, R. Bock, F. Seland, K. E. Einarsrud and O.S. Burheim, "Electrodialytic Energy Storage System: IEM Permselectivity, Stack Measurements and LCA", *Manuscript*

PAPER I
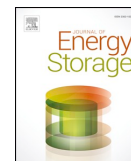
Energy generation and storage by salinity gradient power: A model-based assessment☆

Zohreh Jalili[a,b], Kjersti Wergeland Krakhella[a,b], Kristian Etienne Einarsrud[a], Odne Stokke Burheim[b,*]

[a] *Department of Materials Science and Engineering, Norwegian University of Science and Technology (NTNU), NO-7491 Trondheim, Norway*
[b] *Department of Energy and Process Engineering, Norwegian University of Science and Technology (NTNU), NO-7491 Trondheim, Norway*

ABSTRACT

Three energy storage systems based on mixing and desalination of solutions with different salt concentrations are presented, namely, reverse electrodialysis, pressure retarded osmosis and capacitive Donnan potential, coupled to their corresponding desalination technologies: electrodialysis, reverse osmosis and membrane capacitive deionisation.

Conceptual mathematical models are used to assess power densities and efficiency, and to address the influence on the performance of factors such as temperature and residence time. The maximum power densities for electrodialysis, osmotic and capacitive energy storage systems are calculated as 4.69, 4.83 and 0.503 $\mathrm{W\,m^{-2}}$, respectively, at 25 °C and residence time of 20 s, corresponding to an average fluid velocity of 5 mm/s. In order to achieve competitive economic energy (in the EU) with this power density, the membrane price needs to be lower than 2.9, 3.0 and 0.31$ $\mathrm{m^{-2}}$, for each of the technologies. Utilisation of waste heat to increase the temperature to 60 °C increases the power density to 8.54, 6.04 and 0.708 $\mathrm{W\,m^{-2}}$, which allows for 25% higher osmotic membrane price (3.7$ $\mathrm{m^{-2}}$), and over 80% and 40% higher price (5.2 and 0.43$ $\mathrm{m^{-2}}$) for the ionic exchange membrane used in the electrodialytic and capacitive energy storage system respectively, while still having economic energy production. Advantages and disadvantages of the proposed energy storage systems are discussed, along with the cost evaluation for each technology.

1. Introduction

In order to secure a more sustainable energy supply, reduce carbon emissions and dependency of fossil fuels, renewable energy sources have received considerable attention in research and industrial developments over the last decades. Significant technological improvements have been made, enabling energy production utilising wind, solar, tidal, geothermal and salinity gradient power sources (SGP) [1–4]. A study and forecast made by DNV-GL [5] on the global energy production from 2015 to 2050 is shown in Figure 1.

Fig. 1 indicates a steady increase in energy production and that the growth mainly will be in photovoltaics and wind, both of which depend on large-scale storage due to their intermittent nature [6]. Large-scale energy storage is also expected to play a role in resolving issues related to peak energy consumption and production typically being out of phase. Fig. 2 shows the net electric load (electricity demand minus the

renewable energy supply) for the California grid system operator, with forecasts for 2020 [7]. Data for 2012 and 2013 indicate that the energy demand has two distinct peaks, one in the morning and one during the evening. Following 2014, the net energy demand is decreasing during the daytime, due to increased photovoltaic capacity, resulting in the so-called duck curve [7]. Extrapolating beyond 2020 it is possible to imagine a potential over the generation of energy during daytime hours, followed by an abrupt ramp in demand during the evening.

Energy storage is a viable solution for smoothing out the duck curve, allowing for energy to be generated when it is available and dispatched when and where it is needed. Despite recent advances in battery technology for small and medium scale applications, achieving low cost, high-efficiency large-scale energy storage systems with long life cycles remains a challenge [8,9]. Energy storage based on salinity gradients can potentially overcome some of these challenges.

The energy that can be stored in solutions with different salinity can

Nomenclature

|	
α	membrane permselectivety
N_m	number of membranes
F	Faraday constant
A_m	membrane area
$\Delta\pi$	osmotic pressure
R	universal gas constant
T	temperature
ΔP_h	hydrostatic pressure
ρ	density
ρ_c	conductivity concentrated solution
ρ_d	conductivity dilute solution
Re	Reynold number
K_w	permeability of membrane respect to the water
J_w	water flux across the membrane
c_d	concentration for dilute solution
c_c	concentration for concentrated solution
E_{OCP}	open circuit potential
i	current density
R_Ω	ohmic resistance
R_{AEM}	ohmic resistance in AEM
R_{CEM}	ohmic resistance in CEM
β	shadow factor of the spacer on the membranes
h_d	height of the dilute flow channel
h_c	height of the concentrated flow channel
ϵ	porosity spacer
P	power density
μ	viscosity
l	length flow channel
t_{res}	residence time
d_h	hydraulic diameter
S_{sp}	surface of the spacer filaments
V_{sp}	volume of the spacer filaments
W	work density
η	efficiency
E_{Donnan}	the Donnan potential
E_c	capacitive potential
$E_{c,0}$	start capacitive potential
t	time
C	capacitance of porous electrodes (MCDI and CDP)
$R_{electrode}$	resistance porous electrodes (MCDI and CDP)
t_{cycle}	cycle time for MCDI and CDP
m_m	mass salt transported through membrane
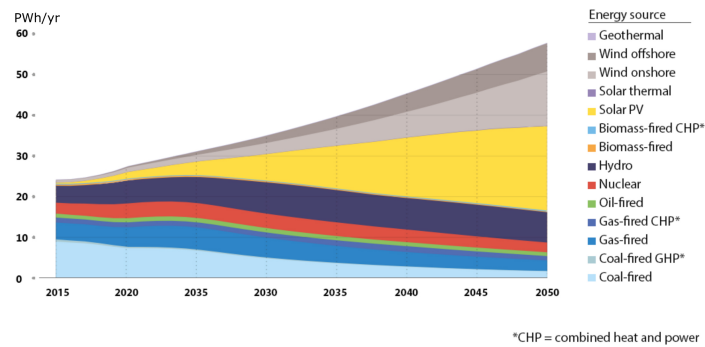
Fig. 1. Forecast of global energy production towards 2050 as of DNV-GL [5].

be significant, depending upon the relative salt concentrations. For instance, the energy released when mixing river- and seawater is around 2 kJ/l of river water, approximately equivalent to a 200 m head of water [1,10]. In that perspective, the energy potential is comparable to that from pumped hydro [2]. Harvesting this energy by membrane-
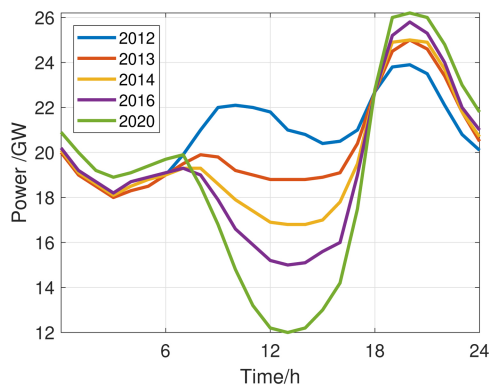

Fig. 2. California net electricity load requirement [7] with forecasts for 2020.

based techniques such as reversed electrodialysis (RED), pressure re-tarded osmosis (PRO) and capacitive Donnan potential (CDP) has been described by several authors, demonstrating the potential for power generation [1–4,11–17]. For a system consisting of 0.5 and 0.05 M NaCl solutions, Post et al. [2] demonstrated maximum power densities of over 2.0 W m^{-2} for RED and 1.2 W m^{-2} for PRO, albeit with similar average power densities due to differences in discharge times. The power density of CDP is expected to be lower, 0.05 W m^{-2} as of Hatzell et al. [15].

Combining SGP technologies with corresponding desalination technologies allow for scalable and sustainable energy storage, as proposed by Yip et al. [18]. Kingsbury et al. [8] and Egmond et al. [19] have both demonstrated a concentration battery based on (reverse) electrodialysis ([R]ED), a concept further developed by Li et al. [20], demonstrating the potential for large-scale storage. An alternative has been proposed by Skilbred et al. [21], suggesting an energy storage system based on RED as a hydrogen production unit, combined with precipitation and evaporation for desalination, with a maximum power density of 28.1 W m^{-2} using KNO$_3$ at 40 °C. Raka et al. conducted an economic study of hydrogen production with RED and ammonium bi-carbonate finding an upper limit for the membrane cost of 20 €/m2 [94].

Enhanced performance relies upon further development in membrane technology as well as optimising system chemistry and geometry.

However, as each of the technologies considered have been developed separately for other applications than energy storage, optmisation has so far been done only for specific technologies and not for combinations. Considering for instance reverse osmosis (RO), the membrane must have high salt rejection while an optimised membrane for PRO should have high water permeation. Since the premises for salinity gradient energy storage is to produce power in high demand periods and utilise cheap electricity when demand is low, optimisation with respect to PRO is more critical than RO, as long as the salt rejection does not become so low that separation in RO is impeded.

For energy storage systems based on ED-RED, the principal focus should be on system characteristics such as stack resistivity [22,4,23], closely related to flow conditions. As demonstrated in simulations by Jalili et al. [24], flow promoters in the dilute solution channels reduce the stack resistivity, while the opposite effect was found in the concentrated channel.

Capacitive systems, i.e. membrane capacitive deionisation (MCDI) and CDP are also strongly influenced by flow conditions, in particular with regard to phenomena related to the inherent switching between concentrated and diluted streams [25,26].

Each of technologies considered are to some extent influenced by concentration polarisation, which reduces mass transport rate through the membranes [27–29] and thereby also the attainable power density. The influence of concentration polarisation was investigated with respect to water flux and power density for PRO by Achilli et al. [30]. The maximum power density was $10.2\,W\,m^{-2}$ for a system with 1.02 and 0.04 M NaCl solutions when concentration polarisation was neglected, and $6.2\,W\,m^{-2}$ when included. Corresponding effects have been identified by several authors [31–37] indicating that concentration polarisation reduces the efficiency of PRO by at least 30%. Changing the solutions into hypersaline solutions increases the energy densities, potentially overcoming energy losses and costs, but such salinities requires further advances in the membrane design. For RED additional losses occur due to co-ion transport and electro-osmosis, most notably at low current densities [4].

Pretreatment of water and bio-fouling are the other practical and operational challenges that have to be considered in membrane-based technologies, as well as reduced membrane lifetime due to high salinity [38,39]. Fouling is considered less relevant for the closed systems considered here.

The present work aims to present conceptual mathematical models of three closed salinity gradient energy storage systems (SGES); ED-RED, RO-PRO and MCDI-CDP, allowing for parametric studies of how parameters such as concentration, residence time or temperature impact on the system performance, i.e. peak power densities. A round-trip efficiency will be calculated for each proposed energy storage system to compare the performance and operational ranges. Also, applicability will be identified, and scientific challenges will be highlighted, aiming to describe system specific challenges rather than challenges related to isolated technologies.

2. Principles of salinity gradient energy storage

A general schematic of an SGES is shown in Fig. 3, in which darker colours indicate higher concentrations. In a closed system, the concentration difference out of the cell stack is not dissipated, but fed back into the reservoirs, an essential advantage of SGES, improving the efficiency compared to salinity gradient energy.

In order to arrive at a model framework in which the different technologies can be compared, the following assumptions were made:

1. The concentration range is limited up to 1 M, considering the range of concentration of ions in river/freshwater and seawater. Egmond et al. [19] showed that there is an additional energy loss in RED because of osmotic water transport for concentrations > 1 M NaCl. Consequently, 1 M is chosen for the maximum concentration in the concentrated solution channel. As the system is considered to be closed, the sum of concentrations in dilute and concentrated streams is always 1 M, i.e. concentrations are varied from 0.01 M to 0.5 M for the dilute solution and from 0.99 M to 0.5 M for the concentrated solution.

2. The power consumption related to pumping of the solutions is assumed to be identical for all three systems, as described below.

3. The solutions are assumed to be ideal, and concentrations are used rather than activity coefficients. The impact of this assumption is investigated in Appendix B, showing that power densities at most are changed by 16%.

4. Membranes are assumed to be semi-ideal in the sense that salt transport through RO-PRO membranes, and water transport through the ED-RED and MCDI-CDP membranes is neglected.

5. Concentration polarisation is not considered in the current work model for all different types of the studied concentration energy storage system. Although the effect of polarisation is considerable, resulting in at least 30% loss in efficiency [32], it is expected that losses are similar for all three technologies – thus not influencing the comparison.

6. The influence of fouling is neglected as the system is considered to be closed.

7. The membrane selectivity is assumed to be temperature and concentration independent as data for his dependency is scarce in our concentration region of operation [40].

8. The models developed consider only a unit cell, and losses which do not scale linearly with the number of unit cells are not considered (e.g. electrode losses for ED-RED).

9. The remaining losses are assumed to be proportional to the relevant membrane fluxes, i.e. current density in ED-RED and MCDI-CDP (Ohmic losses) and water flux in RO-PRO.

10. The energy demand is shown in Fig. 2 is assumed to be representative of the current case, implying that the peak energy demand occurs over a shorter time period than that of low demand. This is interpreted as a constraint on fluxes related to charging and discharging – the flux related to charging is assumed to be half of
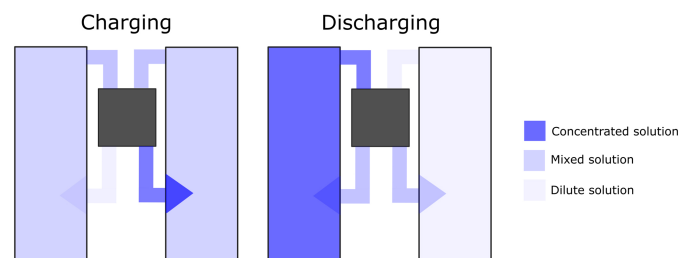
Fig. 3. The figure shows a schematic diagram of the concentration energy storage system. While charging (left), energy is stored in the form of chemical potential by creating low and high salinity solutions. While discharging (right), two feed solutions with different concentrations are mixing, and energy is produced.

that related to discharge.

For each of the proposed technologies, the (ideal) driving force $\mathcal{E}_i^{\text{drive}}$ (e.g. potential or pressure), in combination with resistance $\mathcal{R}_i$ and flux $\mathcal{F}_i$ gives a power density on the form

$$P_i = \mathcal{E}_i^{\text{drive}}\mathcal{F}_i \pm \mathcal{R}_i\mathcal{F}_i^2, \tag{1}$$

where '+' is used when charging and '−' when discharging the system. Differentiation with respect to the flux allows for determination of the peak power density, P_i^{peak}, as well as the corresponding flux, $\mathcal{F}_i^{\text{peak}}$. Fluxes and driving forces are used to define a reversible power density,

$$P_i^{\text{rev}} = \mathcal{E}_i^{\text{drive}}\mathcal{F}_i, \tag{2}$$

which is interpreted as the theoretical maximum power density, used as a normalisation factor to determine efficiencies.

The pump power density can be obtained by Eq. (3) as a function of the solution viscosity, μ, hydraulic diameter of the compartments, D_h and residence time, t_{res}, of solutions flowing in the channels [41]:

$$P_{\text{pump}} = f_{\text{pump}} \frac{48\mu l^2 h\epsilon}{t_{\text{res}}^2 d_h^2} \tag{3}$$

In the above equation, l and h are the length and height of the flow channel respectively, and f_{pump} is a factor accounting for the electrical efficiency of the pump, set to 1.5 based on the study by Daniilidis et al. [42] for a RED system. The average flow velocity is given as $\bar{u} = l/t_{\text{res}}$.

The viscosity of the solution, μ (Pa s), is defined as [43]:

$$\mu = 1.234 \times 10^{-6} e^{0.00212c\,M + 1965/T}, \tag{4}$$

where c is given in M, T is the temperature in Kelvin, and M is the molar mass. Finally, the hydraulic diameter of the channel is defined as [41]:

$$d_h = \frac{4\epsilon}{2/h + (1 - \epsilon)\left(\frac{S_{sp}}{V_{sp}}\right)}, \tag{5}$$

where $\frac{S_{sp}}{V_{sp}}$ is the ratio between the surface and volume of the spacer filaments.

The energy density, W_i, is calculated by integrating the power density with respect to the time:

$$W_i = \int_0^t P_i(t)\mathrm{dt} = \bar{P}_i\Delta t, \tag{6}$$

where $\bar{P}$ is the average power density and t is the total processing time. The energy densities are used to determine the efficiencies of charging by process i and discharging by process j, as well as corresponding round-trip efficiency for the combined process ij:

$$\eta_j^{\text{charge}} = \frac{W_i^{\text{rev}}}{W_{\text{pump}} + W_j} \tag{7}$$

$$\eta_i^{\text{discharge}} = \frac{W_i^{\text{peak}} - W_{\text{pump}}}{W_i^{\text{rev}}} \tag{8}$$

$$\eta_{ij}^{\text{round-trip}} = \eta_j^{\text{charge}}\eta_i^{\text{discharge}} = \frac{W_i^{\text{peak}} - W_{\text{pump}}}{W_{\text{pump}} + W_j}\left(\frac{W_j^{\text{rev}}}{W_i^{\text{rev}}}\right) \tag{9}$$

In the following sections, application specific derivations are given for each of the systems considered.

2.1. Electrodialytic energy storage system; ED-RED

A schematic of an electrodialytic energy storage system is shown in Fig. 4. Charging is performed by ED, while the corresponding discharging process is performed by RED.

Electrodialysis is a membrane-based demineralisation process realised by an imposed electric potential. The conventional ED system consists of a series of anion and cation-exchange membranes (AEM and CEM) alternately placed between two electrodes. A cell pair (unit cell) is the assembly of a CEM, a concentrated solution compartment, an AEM and a dilute solution compartment. In industrial applications, an ED stack consists of 100–200 cell pairs [44].

In a RED cell, ion-exchange membranes separate the channels in which concentrated and dilute solutions are fed in an alternating pattern. Anions migrate through the AEM towards the anode and cations move through the CEM towards the cathode. As a result of the migration of cations and anions in opposite directions, a net ionic current is produced. Simultaneously, the chemical potential difference between the concentrated and dilute solutions generates a voltage across each membrane. Thus, a portion of the Gibbs free energy of mixing is converted to electrical energy and can be harvested continuously [1,22].

2.1.1. Charging the electrodialytic energy storage system

Charging of the electrodialytic energy storage system occurs through the movement of ions from the dilute to the concentrated solution. The driving force opposing this transport is the open circuit potential, E_{OCP}, given as [45,8]:
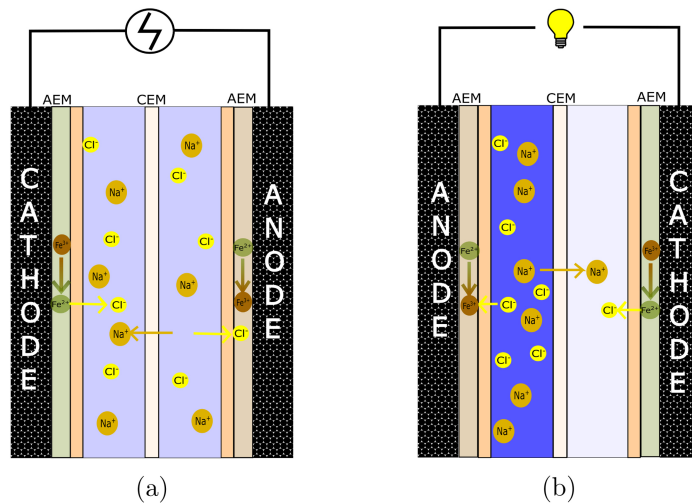
Fig. 4. The figure shows a schematic of the electrodialytic energy storage system. (a) During charging by ED, ions move from dilute solution towards the concentrated solution. (b) During discharging by the RED process, the electrical current is reversed, and ions move back from the concentrated to dilute solution, eventually re-establishing the initial condition.

$$\mathcal{E}_{\text{ED/RED}}^{\text{drive}} = E_{\text{OCP}} = 2N_m \frac{\bar{\alpha}RT}{F}\ln\left(\frac{c_c}{c_d}\right), \tag{10}$$

where c_c and c_d are concentrations of the concentrated and dilute solutions respectively, F is Faraday's constant, T is temperature, R is the universal gas constant, N_m is number of membrane pairs and $\bar{\alpha}$ is the average permselectivity. The permselectivity expresses the capability of the membrane to transport a specific type of ion, either cation or anion.

The power requirement for an ED unit cell, excluding pumping power consumption, is:

$$P_{\text{ED}} = E_{\text{OCP}}i_{\text{ED}} + R_\Omega i_{\text{ED}}^2, \tag{11}$$

where i is the current density (e.g. flux of charge) and R_Ω is the ohmic area resistance for a ED-RED unit cell, calculated as [41]:

$$R_\Omega = \frac{R_{\text{AEM}}}{1-\beta} + \frac{R_{\text{CEM}}}{1-\beta} + \frac{\rho_c h_c}{\epsilon^2} + \frac{\rho_d h_d}{\epsilon^2}, \tag{12}$$

where R_{AEM} and R_{CEM} are the area resistances of the AEM and CEM respectively and β is the mask fraction or spacer shadow factor [8]. h_d and h_c are the heights of the dilute and concentrated solution channels, ϵ is the porosity (open area) of the spacer, where the spacers keep the CEM and AEM apart and enhance the mixing of the solutions [46]. ρ_c and ρ_d are the resistivity of the concentrated and dilute feed, respectively, given as:

$$\rho_{\text{sol},10} = a \cdot c^b$$
$$a = 0.1476 \pm 0.0077\Omega\text{m}$$
$$b = -0.959 \pm 0.013\Omega\text{m}, \tag{13}$$

based on data from [47], where $\rho_{sol,10}$ is the solution resistivity at 10 °C (Ωm) and c is the concentration (M) (the concentration is rewritten from ppm to M using [48]). The theoretical temperature effect on the resistivity is also obtained from [47]:
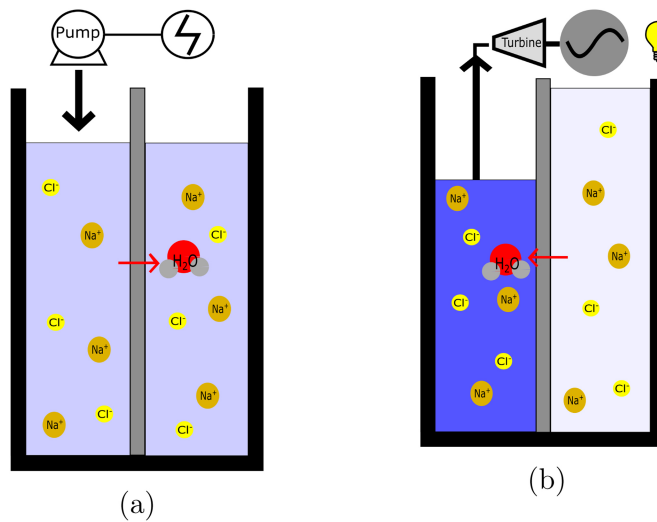
$$\rho_{\text{sol}} = \rho_{\text{sol},10}\frac{31.1\text{K}}{T - 251.5\text{K}}, \tag{14}$$

where T is the temperature in Kelvin. The reversible power density is given as:

$$P_{\text{ED}}^{\text{rev}} = i_{\text{ED}}E_{\text{OCP}}. \tag{15}$$

2.1.2. Discharging the electrodialytic storage system

Discharge of the electrodialytic energy storage system occurs through the (spontaneous) movement of ions from the concentrated to the dilute solution. The power density is expressed as:

$$P_{\text{RED}} = E_{\text{OCP}}i_{\text{RED}} - R_\Omega i_{\text{RED}}^2, \tag{16}$$

where E_{OCP} is obtained using Eq. (10). The current density corresponding to the peak power density of the discharging process is:

$$i_{\text{RED}}^{\text{peakpower}} = \frac{E_{\text{OCP}}}{2R_\Omega}, \tag{17}$$

where the peak power density is:

$$P_{\text{RED}}^{\text{peak}} = \frac{E_{\text{OCP}}^2}{4R_\Omega}. \tag{18}$$

It is worth mentioning that Eqs. (17) and (18) are valid if the stack and load resistances are equal [4,6].

2.1.3. Efficiencies for the electrodialytic energy storage system

Integration as of Eq. (6) gives the following charging efficiency:

$$\eta_{\text{ED}} = \frac{W_{\text{ED}}^{\text{rev}}}{W_{\text{pump}} + W_{\text{ED}}} \tag{19}$$

Correspondingly, substituting $i_{\text{ED}} = 0.5 \times i_{\text{RED}}^{\text{peakpower}}$ (following from the duck-curve) and neglecting pumping losses, the maximum efficiency of ED can be expressed as:

$$\eta_{\text{ED}}^{\text{max}} = \frac{i_{\text{ED}}E_{\text{OCP}}}{E_{\text{OCP}}i_{\text{ED}} + R_\Omega i_{\text{ED}}^2} = \frac{E_{\text{OCP}}^2/4R_\Omega}{E_{\text{OCP}}^2/4R_\Omega + E_{\text{OCP}}^2/16R_\Omega} = \frac{4}{5} \tag{20}$$

The efficiency of the discharging process is given as:

$$\eta_{\text{RED}} = \frac{W_{\text{RED}}^{\text{peak}} - W_{\text{pump}}}{W_{\text{RED}}^{\text{rev}}}, \tag{21}$$

expressing the ratio of the net energy generated by RED and the (potential) chemical energy between two solutions. Neglecting the pumping losses, the efficiency can be expressed as:

$$\eta_{\text{RED}}^{\text{max}} = \frac{E_{\text{OCP}}^2/4R_\Omega}{E_{\text{OCP}}^2/2R_\Omega} = \frac{1}{2}, \tag{22}$$

i.e., the maximum efficiency of RED is 0.5, considering the proposed definition of efficiency [6].

The round-trip efficiency of the electrodialytic energy storage system is:

(a)

(b)

Fig. 5. The figure shows a schematic of the osmotic energy storage system. (a) During charging by RO, ions concentration is increased in one solution compared to the other solution due to water movement from high salinity solution towards to low salinity solution. (b) During discharging by PRO, the water flux is reversed, and water moves back from the dilute to concentrated solution, eventually re-establishing the initial condition. Further details of RO-PRO with pressure exchanger (PX) and all flow streams can be found in [13,51].

$$\eta_{\text{ED-RED}} = \eta_{\text{ED}}\eta_{\text{RED}} = \left(\frac{W_{\text{RED}}^{\text{peak}} - W_{\text{pump}}}{W_{\text{ED}} + W_{\text{pump}}}\right)\left(\frac{i_{\text{ED}}}{i_{\text{RED}}}\right), \tag{23}$$

which, as of Eqs. (20) and (22) has a maximum efficiency of 0.4.

2.2. Osmotic energy storage system; RO-PRO

Reverse osmosis is a separation method using semipermeable membranes, where water is transported through the membrane when a pressure exceeding the osmotic pressure is applied. The technology was developed in the late sixties for desalination [49,12].

An operating pressure around 30–80 bar is typically used for a conversion system of seawater to freshwater utilising commercial membranes [49]. In RO, water is transported through the membrane; thus, demineralised water is accumulated in one side of the membrane and impurities are left in the other side.

Pressure retarded osmosis is the opposite process of RO [2,50]. Water diffuses through the membrane from a low salinity solution to a high salinity solution due to the driving force of the chemical potential gradient across the membrane. An illustration of the osmotic energy storage system is shown in Fig. 5.

Reverse osmosis applies hydrostatic pressure as the driving force for separation, which has to counteract the osmotic pressure that would otherwise favour water flux from the dilute to the concentrated solution. Accordingly, in RO, there is a need for a high-pressure pump and high-pressure vessel to provide a level of energy that can overcome natural osmotic pressure; typically 20–25 bar between the fresh water and seawater [2]. The efficiency can be increased by implementing pressure exchangers (PX) which transfer energy from the high-pressure stream to a low-pressure stream. In the RO-PRO energy storage system, the low-pressure feed stream into RO (high salinity) can be pressurised by the high-pressure draw stream exiting from PRO, reducing the required energy by up to 60% [13,51].

The power needed for pumping water through the two channels in the RO-PRO system is considered to be the same for both channels. This simplification underestimates the power required because the flow velocity is different in the two channels. Consider for example the flow at the end of the membrane in a PRO module; because 70–80% of the feed solution ends up in the draw solution, the flow rate at the outlet becomes 7 times larger on the salty side than on the water side (1.75/0.25 = 7). Because pumping power is proportional to the square of the velocity, the pumping power in the end region of the draw side becomes 3 times (1.75^2) higher at the outlet than at the inlet. Even if the pumping power at the outlet of the waterside lowers to 0.06 (0.25^2) of the inlet need, the total pumping power needs increases by up to 50% compared to the simplified assessment in this study. Because of the non-linearity of this type of calculation, we consider the selected simplification to be sufficient. We find this because the pumping power is typically less than 10% [3] of the system power output so that the net power output only varies with a few percentages (up to 5%).

2.2.1. Charging the osmotic energy storage system

The charging step of the proposed energy storage system is performed by RO. The pressure difference between the two solutions acts as the driving force for this process and is defined as [4]:

$$\mathcal{E}_{\text{RO/PRO}}^{\text{drive}} = \Delta\pi = 2\text{RT}(c_{\text{c}} - c_{\text{d}}), \tag{24}$$

where $\Delta\pi$ is the osmotic pressure, c_{c} and c_{d} are the concentration of concentrated and the dilute solutions respectively (with unit mol/m^3, equal to 1000 M), R is universal gas constant and T is temperature.

The hydrostatic pressure for RO can be calculated by:

$$\Delta P_{\text{h}} = \Delta\pi + \frac{J_{\text{RO}}}{K_{\text{w}}}, \tag{25}$$

and the corresponding power density is:

$$P_{\text{RO}} = J_{\text{RO}}\Delta P_{\text{h}} = \Delta\pi J_{\text{RO}} + \frac{J_{\text{RO}}^2}{K_{\text{w}}}, \tag{26}$$

where J_{RO} is the water flux and K_{w} is the permeability of the membrane with respect to water. The reversible power density is:

$$P_{\text{RO}}^{\text{rev}} = \Delta\pi J_{\text{RO}} \tag{27}$$

It should be noted that the water flux is normally expressed as a function of hydrostatic and osmotic pressure, cf. [4,2,3,50], however, to keep an analogy to ED-RED and MCDI-CDP the reverse relation is used in the current work.

2.2.2. Discharging the osmotic energy storage system

Discharging the osmotic energy storage system occurs when water from the low salinity solution diffuses to the high salinity solution. Contrary to RO, PRO is a low-pressure process. In PRO, the applied hydrostatic pressure, which is needed to pressurise the high salinity solution, is described by Eq. (28) [4]:

$$\Delta P_{\text{h}} = \Delta\pi - \frac{J_{\text{PRO}}}{K_{\text{w}}} \tag{28}$$

The power density of PRO is the product of water flux across the membrane and the hydrostatic pressure drop according to Eq. (29):

$$P_{\text{PRO}} = J_{\text{PRO}}\Delta P_{\text{h}} = \Delta\pi J_{\text{PRO}} - \frac{J_{\text{PRO}}^2}{K_{\text{w}}} \tag{29}$$

The peak power density is obtained when the water flux is defined as Eq. (30):

$$J_{\text{PRO}}^{\text{peakpower}} = \frac{K_{\text{w}}}{2}\Delta\pi, \tag{30}$$

analogous to Eq. (17) when determining the current density in RED.

The corresponding peak power density is given as [4]:

$$P_{\text{PRO}}^{\text{peak}} = \frac{K_{\text{w}}}{4}\Delta\pi^2, \tag{31}$$

while the reversible power density is defined as:

$$P_{\text{PRO}}^{\text{rev}} = \Delta\pi J_{\text{PRO}} \tag{32}$$

2.2.3. Efficiencies for the osmotic energy storage system

Following the definitions introduced earlier, the efficiency for PRO is given as:

$$\eta_{\text{PRO}} = \frac{(W_{\text{PRO}}^{\text{peak}} - W_{\text{pump}})}{W_{\text{PRO}}^{\text{rev}}}, \tag{33}$$

again expressing the ratio of (the net) energy generated by PRO and the (potential) chemical energy between two solutions. Neglecting the pumping losses, the maximum efficiency can be expressed as:

$$\eta_{\text{PRO}}^{\text{max}} = \frac{K_w\Delta\pi^2/4}{K_w\Delta\pi^2/2} = \frac{1}{2}, \tag{34}$$

corresponding to that found for RED.

The efficiency of RO is expressed as:

$$\eta_{\text{RO}} = \frac{W_{\text{RO}}^{\text{rev}}}{(W_{\text{pump}} + W_{\text{RO}})}. \tag{35}$$

Substituting $J_{\text{RO}} = 0.5 \times J_{\text{PRO}}^{\text{peakpower}}$ and neglecting pumping losses, the efficiency of RO under the prescribed conditions is:

$$\eta_{\text{RO}} = \frac{J_{\text{RO}}\Delta\pi}{J_{\text{RO}}\Delta\pi + J_{\text{RO}}^2/K_w} = \frac{K_w\Delta\pi^2/4}{K_w\Delta\pi^2/4 + K_w\Delta\pi^2/16} = \frac{4}{5} \tag{36}$$

The efficiency of the osmotic energy storage system (η_{RO-PRO}) can be defined as Eq. (37) as a measure of the fraction of the power densities by discharging and charging.

$$\eta_{RO-PRO} = \left(\frac{W_{PRO}^{peak} - W_{pump}}{W_{RO} + W_{pump}}\right)\left(\frac{J_{RO}}{J_{PRO}}\right), \tag{37}$$

again limited to maximum efficiency of 0.4 at when following the duck-curve constraint and peak-power discharge water flux.

2.3. Capacitive energy storage system; MCDI-CDP

A third technique to store energy via salinity gradients can be realised by combining MCDI and CDP. During both charging and discharging, ions enter and leave the porous electrodes [52–54]. Consequently, the capacitance of the system is playing an essential role in the performance of this energy storage system.

2.3.1. Charging the capacitive energy storage system

The charging of the system is based on MCDI, first introduced by Claude et al. [55,56], as illustrated in Fig. 6. An AEM and a CEM are placed on each electrode, enabling selective ion transport.

Membrane capacitive deionisation consists of four steps. In the first step, a mixed solution flows between two membrane-covered electrodes at open circuit. During the second step, a potential is applied over the electrodes, making the positive ions flow to the negative electrode and vice versa, forming an electrical double layer [57,56] and a Donnan potential, where the outlet solution is less concentrated than the inlet. In the third step, the outer circuit is opened again, letting some ions travel from the electrodes to the solution. During the fourth step the potential is reversed compared to the second step, and the ions are forced from the electrodes to the solution. The outlet solution from the system is now more concentrated than the inlet and is led to a new compartment.

During addition and removal of ions, step 2 and step 4, the time-dependent capacitive potential gradually reduces the drive potential.

2.3.2. Discharging the capacitive energy storage system

Capacitive Donnan potential was first proposed by Sales et al. in 2010 [58] and can be realised with a cell design corresponding to MCDI [59]. An illustration of a CDP system with the ionic flow is shown in Fig. 7.

The CDP process consists of four steps. In the first step, the membrane-covered electrodes are polarised by immersing them in a concentrated solution at open circuit, resulting in a Donnan potential at each electrode. In the second step, the electrodes are connected to an external load allowing a flow of an electric current in an outer circuit, until electrodes attain charge neutrality. In the third step, the circuit is open again, and the concentrated solution is replaced by a dilute solution. The concentration in the electrodes is now higher than the concentration in the solution, promoting ion transport to the solution due to the reversed Donnan potential [60]. In the last step, the

electrodes are connected to an external load again, where the electrons flow in the opposite direction compared to the second step.

2.3.3. Potential from CDP and MCDI

The model of the capacitive energy storage system takes the second and fourth step into account, while excluding the two steps in which the solution in the cell is changed. The driving force is the sum of the Donnan-, E_{Donnan}, and capacitive potential, E_c, i.e.

$$\mathcal{E}_{MCDI/CDP}^{drive} = E_{Donnan} + E_c, \tag{38}$$

while the cell potential is expressed as [25]:

$$E_{MCDI/CDP} = E_{Donnan} + E_c - iR_\Omega, \tag{39}$$

where i is the current density, defined as positive when adding ions to the electrode and negative when ions are removed, and R_Ω is the ohmic resistance. The Donnan potential is calculated as:

$$E_{Donnan} = 2\bar{\alpha}\frac{RT}{zF}\ln\left(\frac{c_{sp}}{c_{el}}\right), \tag{40}$$

differing slightly from the Nernst equation (Eq. (10)), due to the specification of the concentration in the spacer, c_{sp}, and electrode, c_{el}. The potential in MCDI and CDP alternates between positive and negative depending on whether the concentration is highest in the spacer or in the electrode [59,61]. The capacitive potential for CDP and MCDI is given in Eqs. (41) and (42), respectively:

$$E_{c,CDP} = E_{c,0} - \frac{i_{CDP}}{C_{CDP}}t_{CDP} \tag{41}$$

$$E_{c,MCDI} = E_{c,0} + \frac{i_{MCDI}}{C_{MCDI}}t_{MCDI}, \tag{42}$$

where $E_{c,0}$ is the initial capacitive potential at the start of a new step in the cycle, C is the capacitance of the unit cell and t_{MCDI} and t_{CDP} is the time between a new concentration entering the cell, until the total potential reaches zero, i.e.:

$$t_{MCDI} = \frac{C}{i}(-E_d - E_{c,0} + iR_\Omega) \tag{43}$$

$$t_{CDP} = \frac{C}{i}(E_d + E_{c,0} - iR_\Omega) \tag{44}$$

When adding ions to the electrodes in CDP and removing ions from the electrodes in MCDI, the solution in the spacer is concentrated. The resistance is in this case given as:

$$R_{\Omega,CDP}^{add} = R_{\Omega,MCDI}^{remove} = \frac{R_{AEM}}{1-\beta} + \frac{R_{CEM}}{1-\beta} + \frac{\rho_c h_c}{\epsilon^2} + R_{electrodes} \tag{45}$$

Correspondingly, while both removing ions from the electrodes in CDP and adding ions to the electrodes in MCDI, the solution in the spacer is

Flow direction
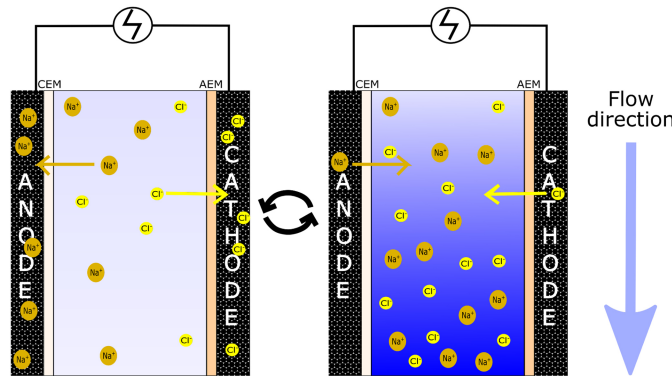
Fig. 6. The figure shows an illustration of the MCDI technology. A solution flows into the system which alternates between producing a diluted (left) and concentrated solution (right) by alternating ion exchange with porous electrodes. Electrodes are charged when producing the dilute solution and discharged when producing the concentrated solution. Each solution is stored in separate containers.
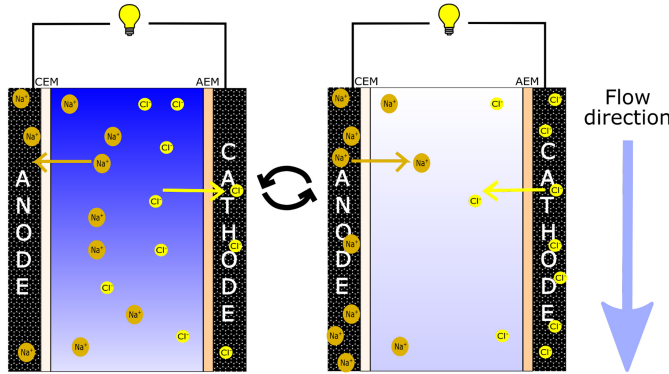
Fig. 7. The figure shows an illustration of the CDP technology. Concentrated (left) and dilute (right) solutions flow alternately into the system producing a solution of mixed concentration. Electrodes are charged while the concentrated solution is flowing and discharged to the dilute solution in a spontaneous (energy producing) process.

dilute, with resistance equal to:

$$R_{\Omega,\text{CDP}}^{\text{remove}} = R_{\Omega,\text{MCDI}}^{\text{add}} = \frac{R_{\text{AEM}}}{1-\beta} + \frac{R_{\text{CEM}}}{1-\beta} + \frac{\rho_{\text{d}} h_{\text{d}}}{\epsilon^2} + R_{\text{electrodes}} \qquad (46)$$

In Eqs. (45) and (46), R_{AEM} and R_{CEM} are the area resistances of the AEM and CEM respectively, β is the shadow factor of the spacer, h_{c} and h_{d} are the heights of the concentrated and dilute compartment respectively, ϵ is the porosity of the spacer and ρ_{c} and ρ_{d} is the resistivity of the concentrated and dilute solution respectively (Eqs. (13) and (14)).

By substitution, the potential adding and removing ions to and from the electrodes for CDP and MCDI is:
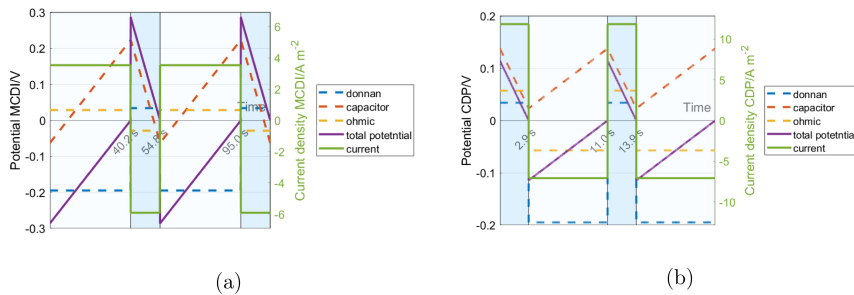
$$E_{\text{CDP}}^{\text{add}} = 2\tilde{\alpha}\frac{RT}{F}\ln\left(\frac{c_{\text{sp}}}{c_{\text{el}}}\right) + E_{\text{c},0} - \frac{i}{C}t - i\left(\frac{R_{\text{AEM}}}{1-\beta} + \frac{R_{\text{CEM}}}{1-\beta} + \frac{\rho_{\text{c}} h_{\text{c}}}{\epsilon^2}\right) \qquad (47)$$

$$E_{\text{CDP}}^{\text{remove}} = 2\tilde{\alpha}\frac{RT}{F}\ln\left(\frac{c_{\text{sp}}}{c_{\text{el}}}\right) + E_{\text{c},0} - \frac{i}{C}t - i\left(\frac{R_{\text{AEM}}}{1-\beta} + \frac{R_{\text{CEM}}}{1-\beta} + \frac{\rho_{\text{d}} h_{\text{d}}}{\epsilon^2}\right) \qquad (48)$$

$$E_{\text{MCDI}}^{\text{add}} = 2\bar{\alpha}\frac{RT}{F}\ln\left(\frac{c_{\text{sp}}}{c_{\text{el}}}\right) + E_{\text{c},0} + \frac{i}{C}t - i\left(\frac{R_{\text{AEM}}}{1-\beta} + \frac{R_{\text{CEM}}}{1-\beta} + \frac{\rho_{\text{d}} h_{\text{d}}}{\epsilon^2}\right) \qquad (49)$$

$$E_{\text{MCDI}}^{\text{remove}} = 2\bar{\alpha}\frac{RT}{F}\ln\left(\frac{c_{\text{sp}}}{c_{\text{el}}}\right) + E_{\text{c},0} + \frac{i}{C}t - i\left(\frac{R_{\text{AEM}}}{1-\beta} + \frac{R_{\text{CEM}}}{1-\beta} + \frac{\rho_{\text{c}} h_{\text{c}}}{\epsilon^2}\right). \qquad (50)$$

Fig. 8 shows the potential with respect to the time, given constant current for two cycles for CDP and MCDI. The solutions are switched when the total potential is zero, and the model is run until the change in initial capacitive potential is less than 0.1%.

2.3.4. Current density in the capacitive energy storage system

The current density for adding and removing ions to and from the electrodes in CDP, is chosen at maximum power density, given in Eqs. (51) and (52):

$$i_{\text{CDP}}^{\text{add}} = \frac{E_{\text{Donnan}} + E_{\text{c},0}}{2t^{\text{add}}/C^{\text{add}} + 2R_{\Omega,\text{CDP}}^{\text{add}}}, \qquad (51)$$

$$i_{\text{CDP}}^{\text{remove}} = \frac{E_{\text{Donnan}} + E_{\text{c},0}}{2t^{\text{remove}}/C^{\text{remove}} + 2R_{\Omega,\text{CDP}}^{\text{remove}}}, \qquad (52)$$

Since a fixed current density and water flux is used in the modelling of ED-RED and RO-PRO, corresponding conditions are assumed for MCDI-CDP for the sake of comparison. The maximum power- and corresponding current density is determined graphically from plots generated by varying t^{add} and t^{remove} in Eqs. (51) and (52). An example of power density as a function of current density at 25 °C for 30 different concentrations between 0 and 1 M is given in Fig. 9.

The discharging current is half of the charging current and visa verse, corresponding to the systems described previously:

$$i_{\text{MCDI}}^{\text{add}} = -\frac{i_{\text{CDP}}^{\text{remove}}}{2} \qquad (53)$$

$$i_{\text{MCDI}}^{\text{remove}} = -\frac{i_{\text{CDP}}^{\text{add}}}{2} \qquad (54)$$

2.3.5. Power and energy density from CDP and MCDI

The average power density, while adding and removing ions from the electrodes in both CDP and MCDI is:

$$\bar{P} = \frac{1}{\Delta t}\int_{t_1}^{t_2} P\,dt = \frac{1}{\Delta t^{\text{add}} + \Delta t^{\text{remove}}}\left(\int_{t_1^{\text{add}}}^{t_2^{\text{add}}} P^{\text{add}}dt + \int_{t_1^{\text{remove}}}^{t_2^{\text{remove}}} P^{\text{remove}}dt\right), \qquad (55)$$

where $\Delta t^{\text{add}} = t_2^{\text{add}} - t_1^{\text{add}}$ and $\Delta t^{\text{remove}} = t_2^{\text{remove}} - t_1^{\text{remove}}$ are the

(a)

(b)

Fig. 8. Potential with respect to the time in MCDI (a) and CDP (b) for two cycles. Light colour indicates a dilute solution, where ions are added to the electrodes for MCDI and removed in CDP. Dark colour indicates a concentrated solution, where ions are removed from the electrodes for MCDI and added for CDP. (For interpretation of the references to colour in this figure legend, the reader is referred to the web version of this article.)
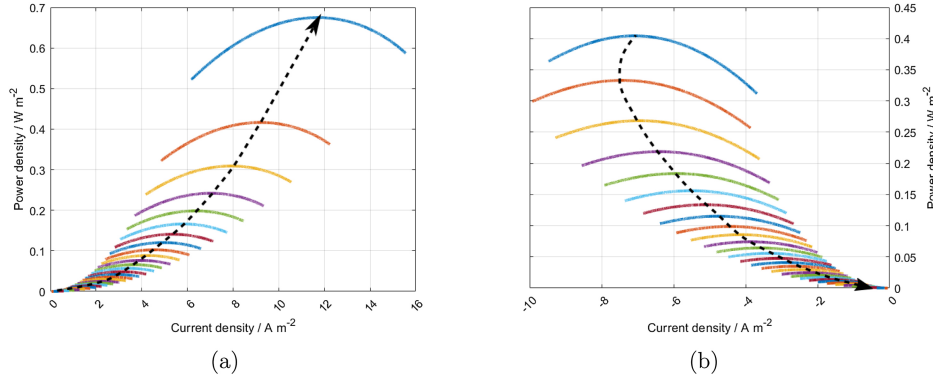
Fig. 9. Power density as a function of current density for CDP while adding ions to the electrodes (a) and removing the ions from the electrode (b). The black dotted lines give the maximum power density, where the arrow indicates direction of increasing concentration. The temperature is 25 °C.

time which take to add and remove ions from the electrode respectively.

The reversible power density from one cycle of CDP and MCDI is the product of the current density and the drive potential, where the latter is the summation of Donnan potential (Eq. (40)) and the capacitive potential (Eq. (41)).

$$\bar{P}_j^{\text{rev}} = \frac{1}{\Delta t} \int_{t_1}^{t_2} i_j (E_{\text{Donnan}} + E_c) dt \tag{56}$$

2.4. Efficiency of CDP and MCDI

Corresponding to the other technologies, the relevant efficiencies are given as:

$$\eta_{\text{CDP}} = \frac{W_{\text{CDP}}^{\text{peak}} - W_{\text{pump}}}{W_{\text{CDP}}^{\text{rev}}}, \tag{57}$$

$$\eta_{\text{MCDI}} = \frac{W_{\text{MCDI}}^{\text{rev}}}{W_{\text{MCDI}} + W_{\text{pump}}} \tag{58}$$

and

$$\eta_{\text{MCDI-CDP}} = \eta_{\text{MCDI}} \eta_{\text{CDP}} = \frac{W_{\text{CDP}}^{\text{peak}} - W_{\text{pump}}}{W_{\text{CDP}}^{\text{rev}}} \frac{W_{\text{MCDI}}^{\text{rev}}}{W_{\text{MCDI}} + W_{\text{pump}}} \tag{59}$$

Neglecting the pumping losses, the maximum efficiency can be found to be equivalent to the other technologies, i.e. 0.5 for CDP, 0.8 for MCDI and 0.4 for the round-trip efficiency.

3. Results and discussion

The following section describes the results for each energy storage system separately, where each subsection contains drive potential, power density and efficiency of the charging and discharging, in addition to the total efficiency. The maximum power density with respect to concentrations is also calculated for each discharging process for temperature varying from 10 °C to 80 °C. Finally, the average electricity price in USA and EU is compared to the cost of all three energy storage system, given different membrane prices. The input parameters for the three models are given in Table 1.

3.1. Electrodialytic energy storage; ED-RED

The open circuit potential with respect to the concentration of dilute solution at different temperatures is demonstrated in Fig. 10, while the ohmic resistance over one unit cell is plotted in Fig. A.25(a) in Appendix A. The main contributor to the resistance is the resistivity of

the dilute solution. The peak power current density to discharge the electrodialytic energy storage system, is depicted in Fig. A.25(b) in Appendix A.

The peak power current density (Eq. (17)) is proportional to the open circuit potential, and inversely proportional to the resistance. As the resistance is increasing faster than the open circuit potential at low concentrations, the overall effect is a reduction in the peak power current densities at these concentrations, as shown in Fig. A.25(b).

The power density of charging and discharging of electrodialytic

Table 1
Input values used for models of the three energy storage systems. A discussion regarding additional parameters is given in Appendix D.

Name	Symbol	Value
Channel height	h	2×10^{-4} m [41]
Channel length	l	0.1 m [41]
Channel width	w	0.1 m [41]
Porosity spacer	ϵ	0.7 [41]
Open area spacer	σ	0.5 [41]
Ratio surface to volume spacer filament	$S_{\text{sp}}/V_{\text{sp}}$	8/h
Hydraulic diameter	D_{h}	See Eq. (5)
Power losses pump	P_{pump}	See Eq. (3)
Mean permselectivity CEM and AEM	$\bar{\alpha}$	0.97 [62–64]
Resistance AEM	r_{AEM}	$1.0 \times 10^{-4}\,\Omega\,\text{m}^2$ [62,63]
Resistance CEM	r_{CEM}	$1.0 \times 10^{-4}\,\Omega\,\text{m}^2$ [62,64]
Concentration, concentrated solution	c_c ($c_c = 1 - c_d$)	0.99–0.51 M
Concentration, dilute solution	c_d	0.01–0.49 M
Conc. porous electrodes (MCDI & CDP)	c_m	0.5 M
Temperature	T	[283 298 313 333 353] K
Viscosity solution	μ	Eq. (4)
Solution resistivity	$\rho_{c/d}$	Eqs. (13) and (14)
Water permeability in membrane	K_w	$4.1 \times 10^{-13}\,\text{m (Pa s)}^{-1}$ [4]
Residence times	t_{res}	[10 20 40 70 100] s [41]ᵃ
Corresponding velocities based on l/t_{res}	$\bar{u}$	[10 5.0 2.5 1.4 1.0] mm/s
Capacitance (CDP &MCDI)	C	$4 \times 10^{-2}\,\text{F m}^{-2}$ [61]
Resistance electrodes (MCDI & CDP)	R_e	$4.4 \times 10^{-3}\,\Omega\,\text{m}^2$ [65]
Molar mass NaCl	M	58.44 mol g⁻¹
Faraday's constant	F	96,485 C mol⁻¹
Universal gas constant	R	8.314 J K⁻¹ mol⁻¹

ᵃ Vermaas et al. [41] considered residence times from 0.5 to 200 s to calculate power density from salinity gradient using RED, demonstrating that both too high and too low values were detrimental for system performance.
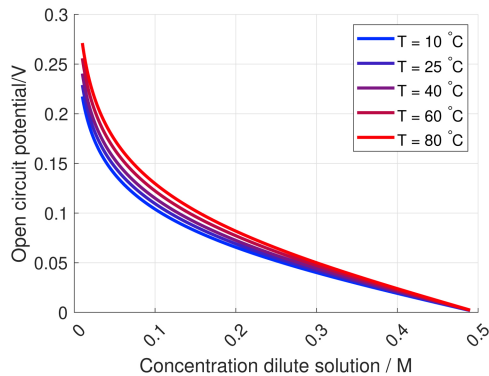
Fig. 10. Open circuit potential for one unit cell of RED and ED. $c_c = 1 - c_d$.

Fig. 12. This figure shows the pumping loss per unit cell area in electrodialytic and osmotic energy storage systems at different temperatures at $C_d = 0.25$ M and $C_c = 0.75$ M.

energy storage system, is presented in Fig. 11. The maximum power density is at a dilute concentration between 0.046 and 0.026 M, where the RED power density is changing from 3.18 to 11.0 W m^{-2}, corresponding to temperatures from 10 °C to 80 °C. The power density at lower dilute concentration is more affected by the drop in current density due to resistance, than the increase in the open circuit potential. The reduction in power density with decreased dilute concentration is in agreement with the theoretical and experimental research by Egmond et al. [19].

The pumping loss as a function of concentration changes less than 0.2% over the total concentration range at fixed temperature and residence time. The pumping loss is plotted as a function of residence time, i.e. the time the fluid spends from inlet to outlet, and temperature in Fig. 12. At lower residence time the influence of temperature on the pump power consumption is greater than at higher residence time. However, at lower temperatures, the influence of residence time is more notable than at higher temperatures. The pumping power loss is reduced by a factor of 100 when increasing the residence time by a factor of 10; from 10 s to 100 s, corresponding to a decrease in velocity of factor 10. Changing the temperature from 10 °C to 80 °C, lowers the pumping loss with a factor 25.

The efficiency of charging and discharging the electrodialytic energy storage system at different residence times is displayed in Fig. 13(a) and (b), while the total efficiency is shown in Fig. 13(c) for a fixed temperature, $T = 25$ °C.

At the beginning of the discharge process, due to the high concentration difference between the two streams, the energy storage
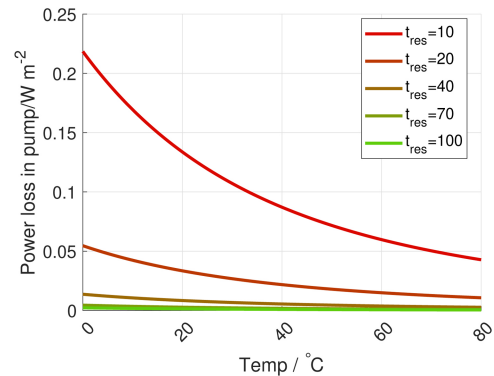
system has a high efficiency where the power generation is higher than the pump power consumption. The efficiency is decreasing as the concentration difference decreases, due to relatively higher energy consumed by the pumps compared to the energy produced. The efficiencies for ED and RED with respect to temperature are given in Fig. 14(a) and (c), respectively. The total electrodialytic energy storage system efficiency, is given in Fig. 14, considering a constant residence time equal to 20 s. The efficiency in RED and ED increases by elevating temperature, due to temperature dependency on drive potential, resistance and pumping losses.

3.2. Osmotic energy storage; RO-PRO

The osmotic pressure difference, $\Delta\pi$, for different temperatures is demonstrated in Fig. 15, while the corresponding water flux for peak power density is shown in Fig. A.26 in Appendix A.

The power densities produced from PRO and consumed in RO are given in Fig. 16. The maximum power density for PRO is changing from 4.36 to 6.78 W m^{-2} corresponding to temperatures from 10 °C to 80 °C, while the pumping losses are the same as for the electrodialytic energy storage system (see Fig. 12).

The efficiency of charging and discharging for different residence times, with respect to the dilute concentration and constant temperature, $T = 25$ °C, is shown in Fig. 17(a) and (b). The total efficiency is given in Fig. 17(c). The efficiencies of PRO and RO are enhanced by
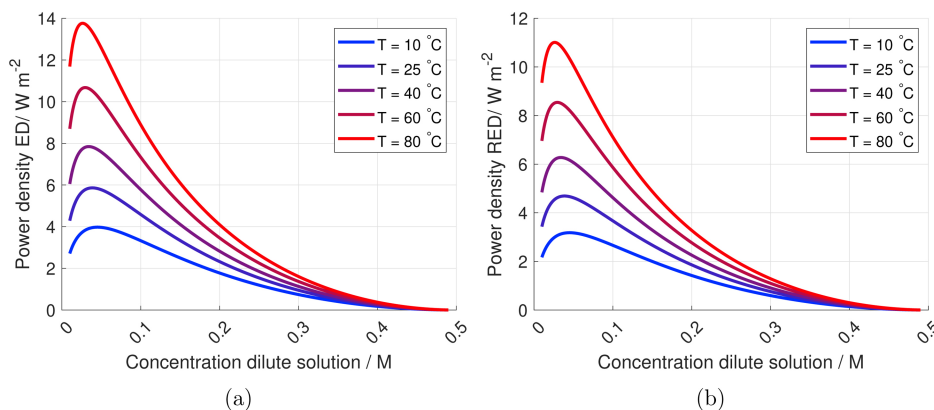

(a)

(b)

Fig. 11. Power per unit cell area while charging (a) and discharging (b) the electrodialytic energy storage system. $c_c = 1 - c_d$.
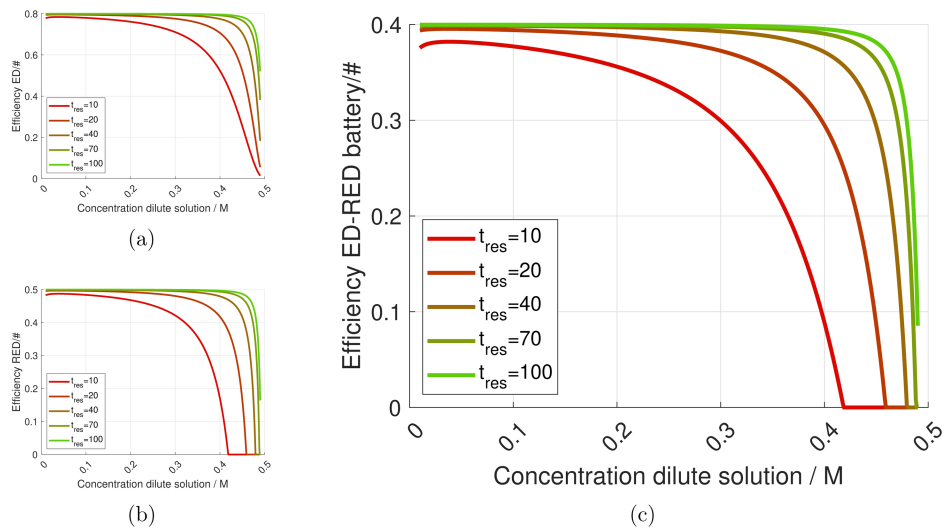
Fig. 13. Efficiency at different residence times for (a) ED, (b) RED and (c) total electrodialytic energy storage system at T = 25 °C and $c_c = 1 - c_d$.

increased residence time, due to the decreasing in pumping losses.

The efficiencies of RO and PRO for different temperatures at fixed residence time, $t_{res} = 20$ s, is shown in Fig. 18(a) and (b), where the total efficiency of osmotic energy storage system is given in Fig. 18(c). The efficiency for PRO and RO increases by elevating temperature, due to the temperature dependency of viscosity and osmotic pressure.

Similarly to the efficiency of the ED-RED energy storage system in Fig. 14, the efficiency of osmotic energy storage system decreases as the concentration difference decreases. The efficiency of the energy storage system is dominated by the PRO process at the early stage of the curve, while the RO energy consumption is controlling the late stage of the curve. Also, as the energy consumption by pump increases (i.e. residence time decreases), the efficiency of osmotic energy storage system decreases at a constant concentration of the dilute solution.

3.3. Membrane capacitive energy storage system; MCDI-CDP

The mean drive potential with respect to time in the membrane capacitive energy storage system is presented in Fig. 19, while the ohmic resistance of a unit cell is presented in Fig. A.27(a) (Appendix A) at different temperatures. The ohmic resistance is higher in the membrane capacitive energy storage system compared to the electrodialytic energy storage system due to the resistance of the porous electrodes included in every unit cell.

Depending on the concentration in the spacer and the state of charge, the current at peak power density changes. The current density decreases at lower concentrations, due to an increased cell resistance. The average power densities gained from CDP and the average consumed power density in MCDI are shown in Fig. 20. The power density obtained from CDP is 0.8 of what is consumed by MCDI.
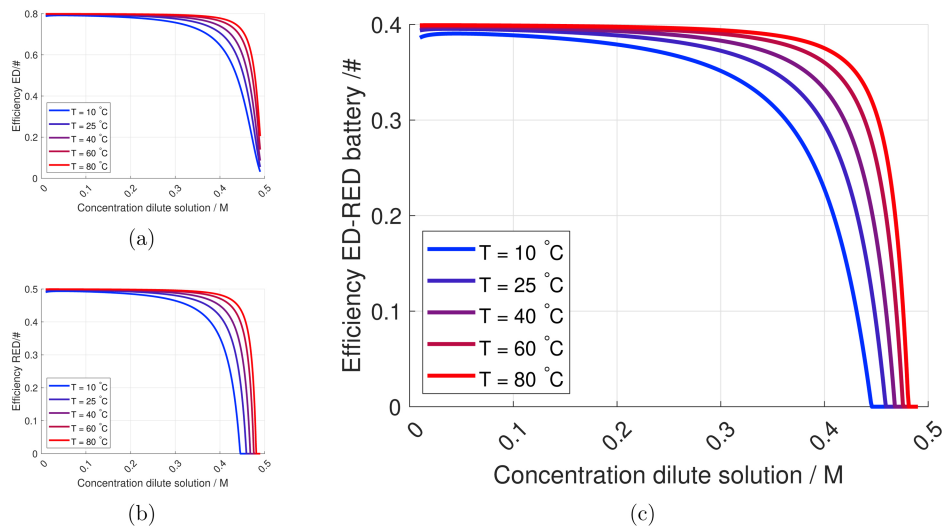

Fig. 14. Efficiency at different temperatures for (a) ED and (b) RED and (c) total electrodialytic energy storage system. $t_{res} = 20$ s and $c_c = 1 - c_d$.
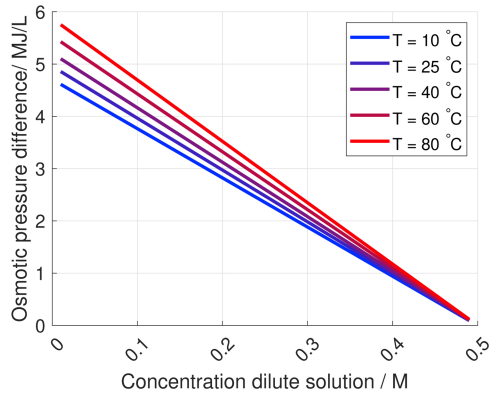
Fig. 15. Osmotic pressure difference for PRO and RO. $c_c = 1 - c_d$.

The pumping power consumption in the capacitive energy storage system is half of the pumping consumption in the electrolytic and osmotic energy storage system, since MCDI and CDP only have one flow compartment per unit cell. The efficiency of MCDI and CDP for different residence time at fixed temperature, $T = 25$ °C, is given in Fig. 21(a) and (b), while the total efficiency is given in Fig. 21(c). The efficiency for MCDI and CDP are decreasing rapidly with residence time due to the increase in power consumption of pump.

The temperature effect on the efficiency of MCDI and CDP at fixed residence time, $t_{res} = 20$ s is given in Fig. 22(a) and (b). The total efficiency of the membrane capacitive energy storage system is given in Fig. 22(c). The efficiency increases by elevating temperature, due to temperature dependency of drive potential, resistance and pump power consumption.

3.4. Energy price and membrane cost

A comparison of minimum, maximum and mean values of energy price between EU and USA are shown in Figure. 23 . The energy cost of each energy storage system needs to be competitive with the energy prices given in Fig. 23 to take its market share. A more optimistic market constraint would consider being paid to dump surplus electricity, as is seen in Europe, cf. Appendix C.

The cost of the membrane for ED and MCDI was reported two or three times higher than that for RO according to Van der Bruggen et al. [68]. Other researchers like Pirsaheb et al. [69] reported that

considering the capital, operational and maintenance costs, ED membranes are more expensive than RO membranes based on a case study. For separation technology, ED has received less attraction compared to RO. Although RO membranes are cheaper than ED membranes, there are several factors which make ED more attractive compared to RO at certain conditions as reviewed by Westerling [70], reporting that ED is more tunable for specific membranes and constant flow rate. ED requires cross-flow separation using ion exchange membranes, and it operates at lower pressure range (approximately 7 bar) which requires less physical space, easier maintenance and longer lifetime compared to RO (typical range of pressure is 30–80 bar).

The capacitive and electrodialytic energy storage systems are using AEMs and CEMs; either as a separate layer or as a coating applied directly onto the electrodes. NAFION 117 is a popular membrane [60] with a cost of approximately 1\$ cm^{-2} [71] (10 000\$ m^{-2}), while membranes from Fumatech is approximately 0.05\$ cm^{-2} (500\$ m^{-2}) at lab scale. The cost of the osmotic membrane is typically 20–50\$ m^{-2} [72,17]. Post claims the electrodialytic membrane is 2–3 times more expensive than the osmotic membrane, but the installed area cost of membranes considering pump, turbine and pressure vessels, evens out this cost difference [23]. Based on a financial feasibility study of a RED power plant by Daniilidis [17], the most influential parameter on the cost is the price of the membranes. For simplicity and initial estimate, all other sources of the cost are neglected. The lifetime for all three batteries is assumed to vary from 3 to 10 years [3,16] for comparison, with 3% down-time [17]. According to the duck curve constraint, the battery is discharging approximately 3 h a day.

The peak power densities from ED-RED, RO-PRO and MCDI-CDP are given in Table 2. The total cost per total membrane area is estimated and is shown in Fig. 24 by varying the cost per membrane area, for a constant temperature of 25 °C and 60 °C and residence time of 20 s.

The maximum energy price in EU is 0.23\$/kWh and in the USA 0.31\$/kWh (see Fig. 23). To generate electricity below these prices by the three storage systems with an operational time of 5 years (3 h per day and 3% downtime), considering power densities given in Table 2 for 25 °C, the membrane cost needs to be lower than 2.9, 3.0, 0.31\$ m^{-2} for RED, PRO and CDP respectively. Increasing the temperature to 60 °C, the membrane can cost up to 5.2, 3.7 and 0.43\$ m^{-2} for RED, PRO and CDP respectively.

3.5. Evaluation of the three energy storage systems

The maximum peak power densities and the total efficiencies at $t_{res} = 20$ s for all three energy storage systems are given in Table 2.
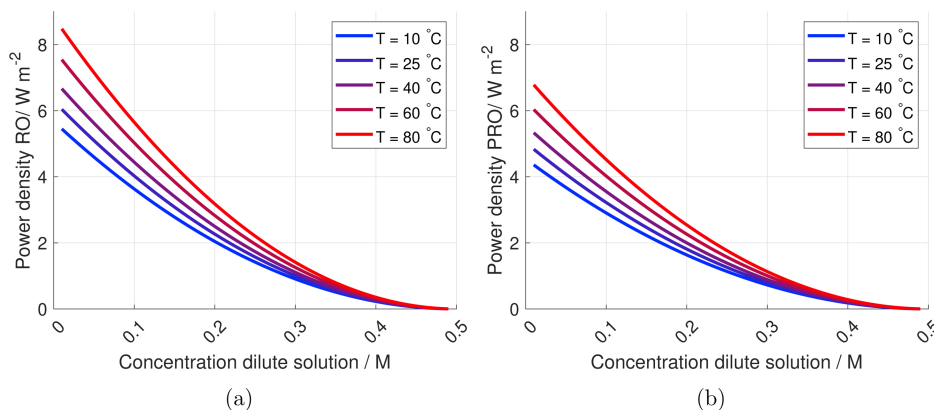

(a)

(b)

Fig. 16. Power per unit cell area used in RO (a) and gained from PRO (b). $c_c = 1 - c_d$.
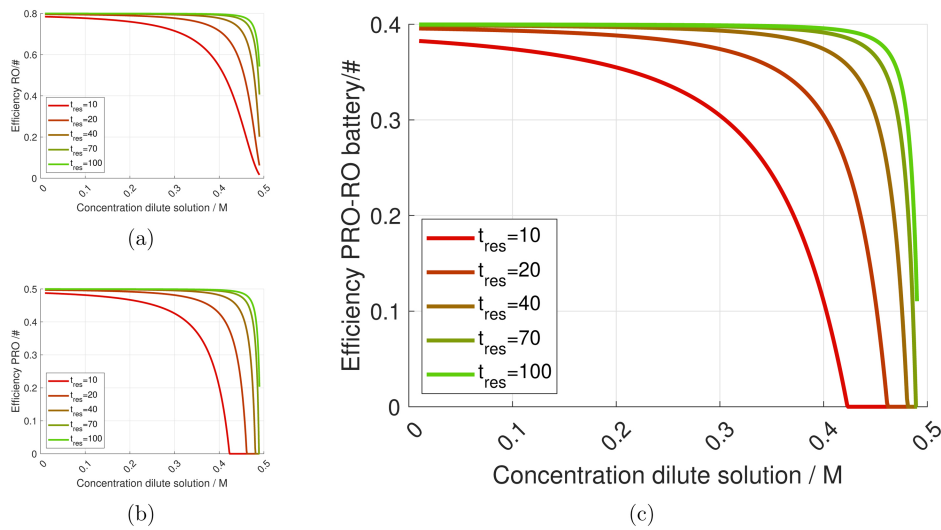
Fig. 17. Efficiency at different residence times for (a) RO, (b) PRO and (c) the total osmotic energy storage system. $T = 25\,°C$ and $c_c = 1 - c_d$.

3.5.1. Power density

The maximum power density of the electrodialytic energy storage systems is higher than the power density of the osmotic energy storage systems at temperatures over 40 °C, while the maximum power density of the capacitive energy storage system is approximately one-tenth of the power density of the other studied discharging processes.

The average discharging power density of the electrodialytic energy storage system by Kingsbury et al. [8], was in the range of 0.07–0.44 W m^{-2}, which is less than the average power density of our electrodialytic energy storage system (1.7 W m^{-2} at 25 °C). The difference in power density is due to difference in the operating conditions like lower temperature (18.5 °C), lower average permselectivity (91%) and lower concentration difference (0.5 M and 0.25 M). They considered pumping losses, Faradaic losses (which is mostly influenced by osmosis) and losses in the model. It is important to mention that

Kingsbury et al. [8] did the first experimental study that demonstrated that ED-RED could be used for energy storage. Also, the Kingsbury et al. study showed that by comparing experimental measurements and modelled results, the performance of the ED-RED battery could be successfully modelled based on known ED-RED and mass transport.

To maximise peak power density in the osmotic energy storage system, membrane characteristics like water permeability, the porous support and membrane structure factor are very important [4,23]. Chemical and mechanical stable materials with desirable separation capability are also desired for the RO membrane due to the operating system in high-pressure condition [50,2]. Yip et al. [50] fabricated a thin-film composite PRO membrane to find a compromise between water permeability and selectivity to maximise the peak power density to 10.0 W m^{-2} for a system containing river and sea water as feed and draw solutions, respectively. Utilising the other manufactured
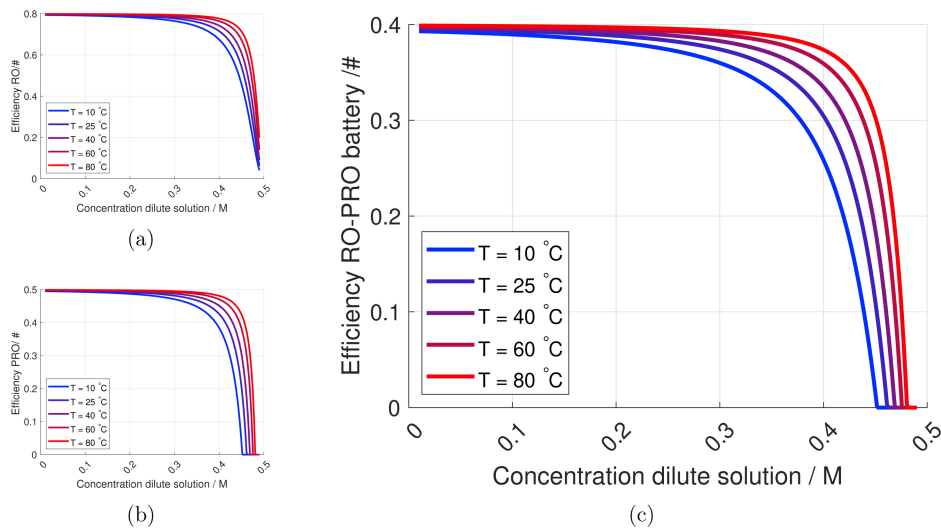

Fig. 18. Efficiency at different temperatures for (a) RO, (b) PRO and (c) the total osmotic energy storage system. $t_{res} = 20\,s$ and $c_c = 1 - c_d$.
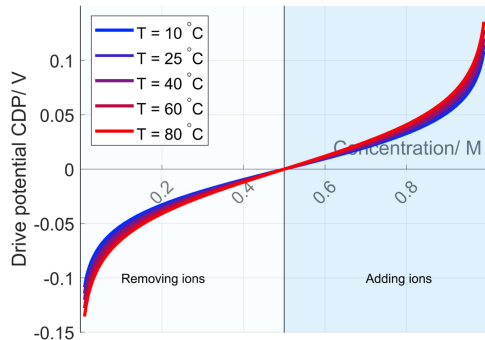
Fig. 19. Drive potential CDP for different temperatures.

membranes with lower salt permeability but with less water permeability resulted in reducing the peak power density as 6.1 W m^{-2} at 25 °C [50]. These values are comparable with the peak power densities achieved at the studied temperature range in our work for PRO (4.83 W m^{-2} at 25 °C), assuming a lower membrane water permeability in our work compared to the water permeability of membrane reported by Yip et al. [50].

One reason for the low power density in CDP is the constant current constraint considering time which is applied in the capacitive energy storage system when the current at peak power of the capacitive energy storage system should be time dependent. Liu et al. reported a maximum power density of 0.205 W m^{-2} using concentration of 0.02 M and 0.5 M and a constant current [25], while Sales et al. [58] had a maximum power density of 0.060 W m^{-2} with the same concentration difference as Liu et al. Hatzell et al. increased the power density from 0.5 W m^{-2} to 0.9 W m^{-2} using ammonium bicarbonate [60].

Another reason for the low power density in the capacitive energy storage system is the much larger unit cell resistance in MCDI-CDP compared to RO-PRO and ED-RED. Considering low power density in CDP, the electrode resistance was neglected for comparison to RED and PRO, giving maximum power densities from 1.30 to 4.10 W m^{-2} at temperatures from 10 °C to 80 °C. It is important to highlight that the maximum power density while adding ions to the electrodes is at the same level as the maximum power densities in RED and higher than PRO (11.0 W m^{-2} at 25 °C from CDP). This is due to lower resistance in the cell with only one compartment with a concentrated solution, leading to a higher current density (130 A m^{-2} at the start of discharge at 25 °C). However, the maximum power density while removing ions in

CDP at 25 °C is 1.21 W m^{-2} which is low compared to the values in RED and PRO. This is due to the high resistance in the cell with only one compartment with diluted solution, leading to a lower current density (15.2 A m^{-2} at the start of discharge at 25 °C). A time-weighted average of maximum power density in CDP is then lower than the maximum power densities in RED and PRO.

Despite low power density and problems with the switching time, the capacitive energy storage system has some advantages over the electrodialytic and osmotic energy storage system. The capacitive system is able to produce electric energy without the need of redox solution (see Fig. 4) used in ED-RED or auxiliary equipment such as a turbine and a pressure exchanger in RO-PRO, thus introducing fewer potential losses in the capacitive systems compared to the other two.

3.5.2. Effect of temperature

In our work, elevating the temperature from 10 °C to 80 °C, increases the power density with more than a factor of 3 for the electrodialytic discharging techniques, while the osmotic and capacitive discharging system increases with a factor 2 for the same temperature increase. The increase in the power density is due to the reduction in the solution resistance and the increase in the drive potential, as well as decreasing of the viscosity and thereby the pumping losses, at elevated temperatures.

Jalili et al. [73] performed a simulation study to investigate the effect of temperature on mass and momentum transport for a dilute channel of a RED system, documenting that increasing Re number as a result of elevated temperature, improves the mass transfer due to enhanced effective diffusivity at higher temperatures. Re number might be increased either by increasing the flow velocity which inturn increases the pressure drop across the channel or reducing the viscosity by enhancing temperature which reduces the pressure drop [73]. Increasing of the temperature can be implemented by utilising the waste heat. Luo et al. [74] and Benneker et al. [75] reported experimentally an increase of the net power density of RED by the usage of the waste heat from industrial processes. Daniilidis et al. [17] performed an experimental investigation for the energy generated by RED using brine at 5 M and reported an increase in power density of almost 80% (from 3.8 to 6.7 W m^{-2}), when temperature was increased from 25 °C to 60 °C. Despite the increase in power density, they also found a decrease in the perm-selectivity of the membrane at higher temperatures. The decrease in perm-selectivity with increased temperatures is something that is not considered in our model. Mei et al. [76] investigated experimentally coupling of RO as a desalination process and RED as a power production unit, but the power gained was low (0.6 W m^{-2} at 60 °C).

Anastasio et al. [77] reported an increase of power density for PRO from 1.3 to 4.0 W m^{-2}, by increasing the temperature from 20 °C to
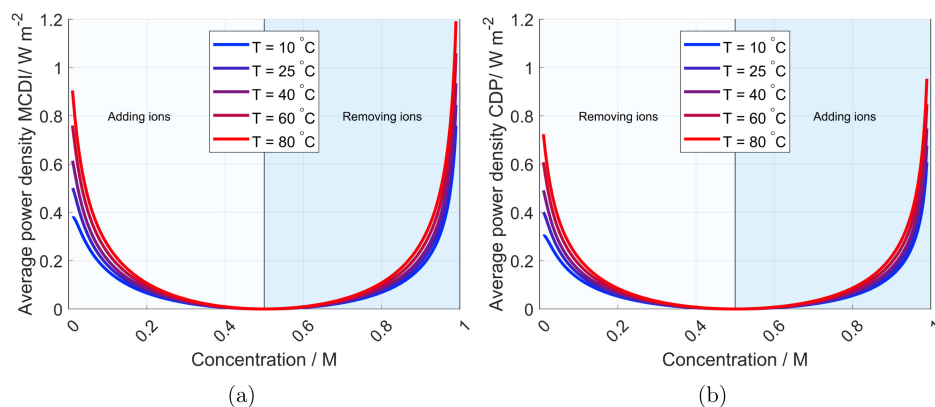

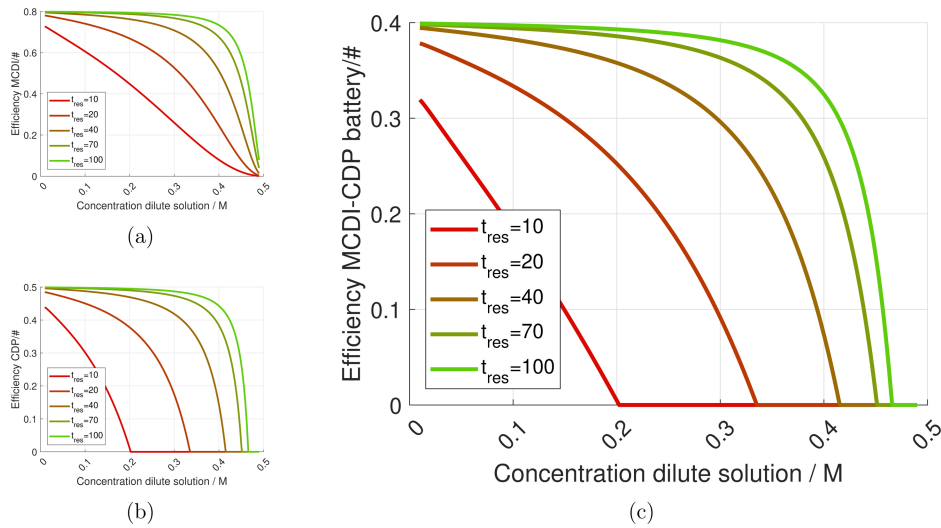**Fig. 20.** Average power per unit cell area for adding and removing ions from electrode for MCDI (a) and CDP (b).

Fig. 21. Efficiency at different residence time for (a) MCDI, (b) CDP and (c) the total capacitive energy storage system. $T = 25\,°C$. $c_c = 1 - c_d$.

40 °C for distilled water and brine (0.5 M). It is reported by Van der Hoek et al. [78] that RO efficiency remains almost constant by temperature changes, as it is a pressure driven process. The RO performance slightly decreases by increasing the temperature due to lower salt rejection at higher temperature and temperature only influences on feed pressure. The salt rejection is not included in our model, and will lower the power density from the osmotic energy storage system. To the author's knowledge, there is no reported research for the temperature effect on the power density generated by CDP. The temperature effect on the power density of RED and PRO found from our model is comparable to the values found in the literature.

Despite enhanced power at elevated temperatures, increasing the temperature has some drawbacks such as thermal degradation of the membranes. However, membranes withstanding temperatures up to 100 °C are reported in the literature [79].

Waste heat could also be utilised in other systems, such as membrane distillation [80,81] (instead of ED) and for instance an organic Rankine cycle [82,83] for power generation. Although efficiencies for both of these technologies can be as high as 90% relative to the Carnot efficiency [81,83], they are not as easily combined into an energy storage system as those proposed here. As such, the utilisation of waste heat to increase the efficiency of the proposed systems is reasonable. It should also be noted that the consumption of waste heat would be low, as the systems are closed and could be designed with minimum heat losses.

3.5.3. Efficiency

From our model, the efficiency of all systems is increased for higher concentration differences due to the increased available potential and consequently generated energy during the discharging process. It is
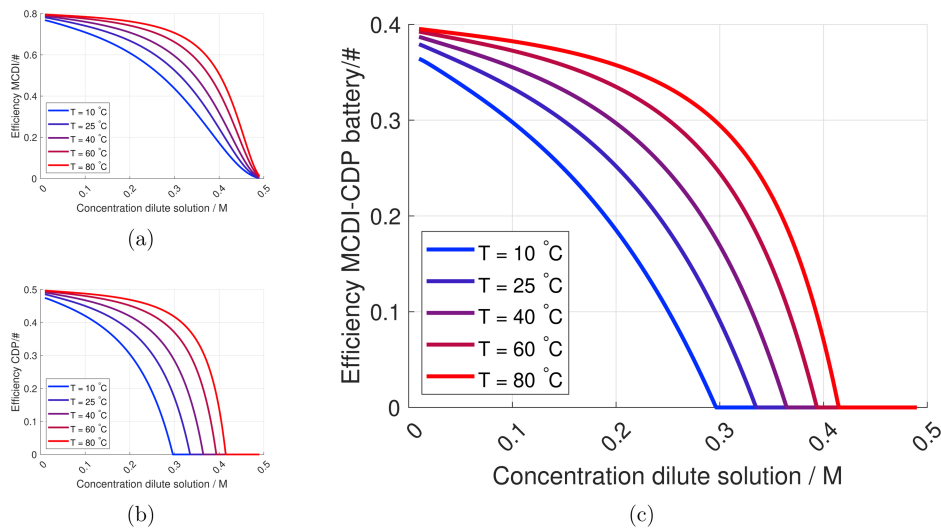

Fig. 22. Efficiency at different temperatures for (a) MCDI, (b) CDP and (c) the total capacitive energy storage system. $t_{res} = 20\,s$ and $c_c = 1 - c_d$.
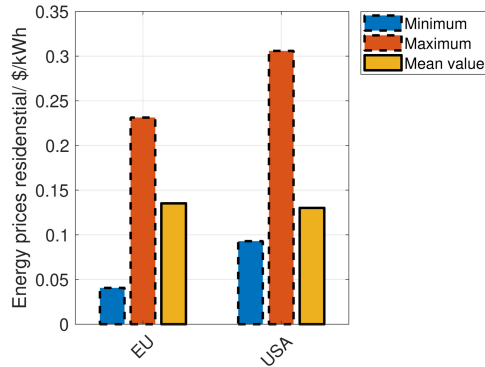
Fig. 23. Electricity prices for residential consumers in USA and EU, with minimum (Louisiana and Ukraine), maximum (Hawaii and Ireland) and mean values averaging over all countries or states [66,67].

important to highlight that the efficiency of the electrodialytic and capacitive energy storage systems are decreasing at lower dilute concentrations, due to the increased ohmic resistance. The relatively high pumping loss in the capacitive energy storage system compared to the power density obtained by CDP, gives a lower efficiency for this system compared to ED-RED and RO-PRO. Increasing the residence time, increases the efficiency of the three types of energy storage systems due to the decrease in pumping losses. Increasing the temperature, increases the efficiency for all systems due to reduced pumping losses and increased power densities.

Kingsbury et al. [8] defined round-trip energy efficiency as the product of current efficiency and voltage efficiency. Despite having the small ohmic loss at low current density, the rate of self-discharging is so high that it results in reducing current efficiency, which gives a low round-trip energy efficiency. At higher current densities, the high ohmic losses lead to a low voltage efficiency and thereby a low round-trip energy efficiency. For that reason, the optimum current density is between 11 and $17\,\mathrm{A\,m^{-2}}$, where the two losses become minimised. Kingsbury et al. reported a round-trip energy efficiency between 21.2 and 34.0% by performing experiments in an electrodialytic energy storage system and neglecting the pumping loss [8]. The efficiency of our studied ED-RED energy storage system was calculated around 40% at starting of discharging and charging. Note that our model does not account losses such as concentration polarisation or osmotic losses by neglecting the water transport through the ionic exchange membranes.

In a review by Yip et al. [18], the efficiency of an energy storage system was expressed as the ratio of the extracted work to Gibbs free energy of two solutions with different salinity. They documented the efficiency of PRO for a system containing sea and river water, as 44% with an average power density of $3.7–5.2\,\mathrm{W\,m^{-2}}$ based on a modelling assessment. However, Yip et al. have used another reference values for efficiency than what is used in our study.

For the discharging of the capacitive energy storage system, energy efficiency up to 46% is reported using wire electrodes in parallel [84].

For the charging part of the capacitive energy storage system, the efficiency is mostly given as the charge efficiency defined as the charge removed from the solution, where Agartan et al. reported an efficiency of MCDI of 49% [85].

It is worth mentioning that to the best of our knowledge; there is no reported round-trip efficiency in the literature, measured experimentally or calculated through modelling approach for RO-PRO or MCDI-CDP concentration batteries.

4. Conclusion

Energy storage systems utilising concentration gradients are one of the solutions to a non-toxic and cheap large-scale energy storage. The current work introduces combined salinity gradient technologies (RED, PRO and CDP) with the corresponding desalination processes (ED, RO and MCDI). Mathematical models were developed for comparing three types of energy storage systems and addressing the influential factors on the performance such as temperature or energy consumption by the pump for the same range of concentrations. Assuming the same pump specifications for all studied systems and isothermal conditions, the maximum power density of an electrodialytic energy storage system is higher than the maximum power density of an osmotic energy storage system at temperatures above 40 °C. The maximum power density of a capacitive energy storage system is approximately one-tenth of the other two systems.

The power densities of the electrodialtic energy storage system increases with more than a factor of 3 by elevating temperature from 10 °C to 80 °C, while the osmotic and capacitive energy storage systems increased by a factor 2. By increasing the temperature, the open circuit potential of ED-RED and MCDI-CDI and the osmotic pressure of RO-PRO increases. Also, the pressure loss of the pump reduces for all three systems at elevated temperature, due to reduced the viscosities. The reduction in the pumping losses at elevated temperatures indicate a potential use for waste heat. Based on our modelling assessment, the efficiencies of the electrodialytic, osmotic and capacitive storage systems are obtained as similar. Therefore, the power density and operational conditions of implementing these energy storage systems define which systems are more effective regarding energy storage.

Pumping energy consumption characterised by residence time and the temperature is another critical parameter for a salinity gradient energy storage system. Increasing the residence time by a factor 10, decreases the pumping power consumption with a factor 100, while increasing the temperature from 10 °C to 80 °C, decreases the power density consumed by pump by a factor 25. Both factors will increase the performance of energy storage systems.

A cost evaluation is presented for each technology. There is a threshold for the cost of different membranes at 5.2, 3.7 and $0.43\,\mathrm{\$\,m^{-2}}$ for the electrodialytic, osmotic and capacitive energy storage system, respectively, at maximum power density at 60 °C. Below this threshold, energy generation is economically feasible, although depending on the operational lifetime of the membrane, downtime, maximum power density and the average electricity price. There is a need for significant reduction of the membrane cost for storing energy through all mentioned concentration energy storage systems.

Table 2
P^{max} for RED, PRO and CDP at $t_{\mathrm{res}} = 20\,s$ and the total energy storage systems efficiencies (recall that the maximum total efficiency for the energy storage systems are 0.4).

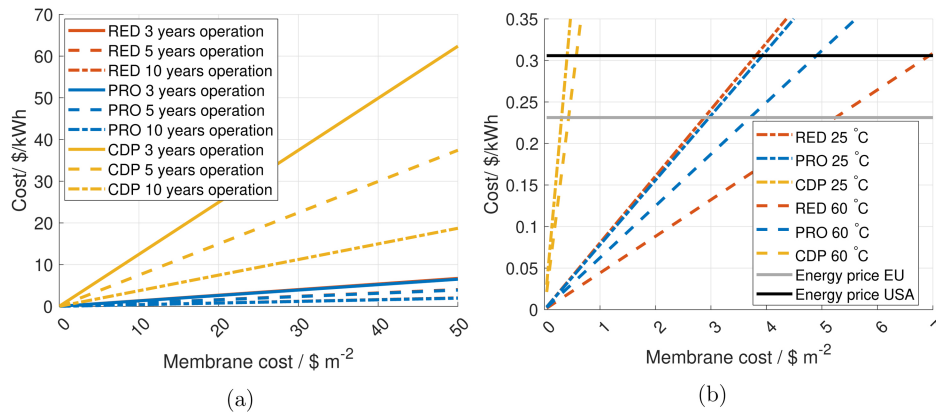| T (°C)	$P_{\mathrm{RED}}^{\mathrm{max}}$ (W m^{-2})	$P_{\mathrm{PRO}}^{\mathrm{max}}$ (W m^{-2})	$P_{\mathrm{CDP}}^{\mathrm{max}}$ (W m^{-2})	$\eta_{\mathrm{ED-RED}}^{\mathrm{Pmax}}$ #	$\eta_{\mathrm{RO-PRO}}^{\mathrm{Pmax}}$ #	$\eta_{\mathrm{MCDI-CDP}}^{\mathrm{Pmax}}$ #
10	3.18	4.36	0.403	0.390	0.393	0.364
25	4.69	4.83	0.503	0.395	0.396	0.379
40	6.28	5.33	0.593	0.397	0.397	0.387
60	8.54	6.04	0.708	0.399	0.398	0.393
80	11.0	6.78	0.823	0.399	0.399	0.395

Fig. 24. Cost of electric energy generation ($/kWh) RED, PRO and CDP at (a) 25 °C and (b) 25 °C and 60 °C compared to the energy price in EU and USA. Residence time is 20 s. Due to the similar power density from RED and PRO at 25 °C, the lines for the two energy generating systems overlap.

Appendix A. Resistance, current density and water flux

The ohmic resistance for the unit cell and the current density at the peak power density in RED, are given in Fig. A.25. The water flux for PRO is given in Fig. A.26. The resistance of CDP and MCDI and the current density at the peak power density in CDP are given in Fig. A.27.
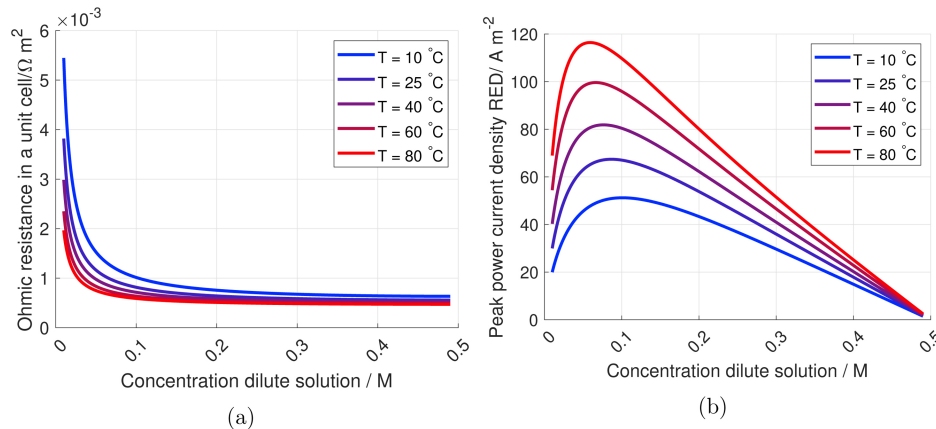

Fig. A.25. The figure shows the ohmic resistance of the ED-RED unit cell (a) and the current at peak power density per RED unit cell area during discharging (b). The current density during charging is considered half of the current density during discharging based on the Duck curve constraint. $c_c = 1 - c_d$.
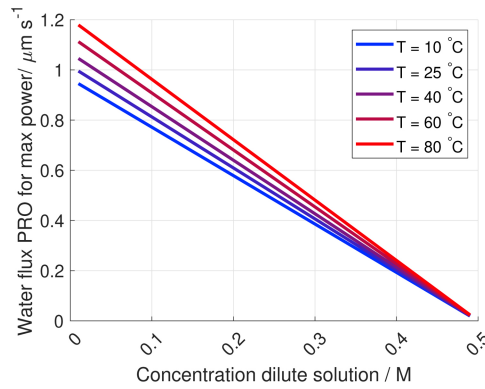
Fig. A.26. Water flux at maximum power density for PRO. $c_c = 1 - c_d$.
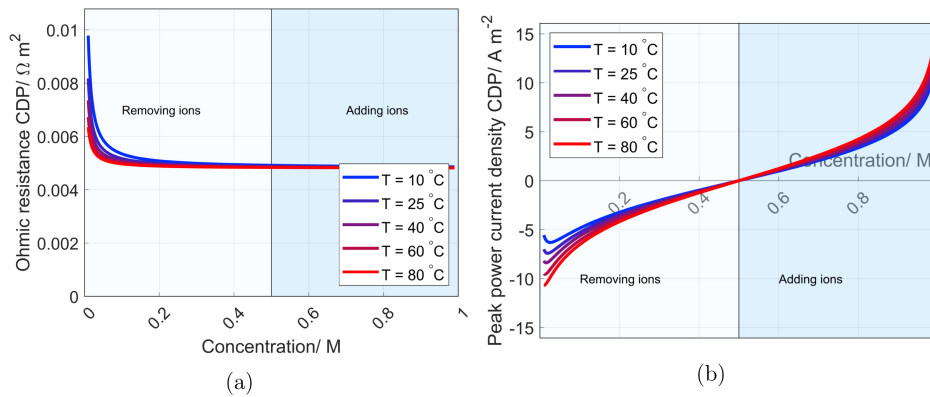

Fig. A.27. The figure shows the ohmic resistance in CDP and MCDI (a), and input peak power current density per unit cell area for CDP for different temperatures (b). The current density during charging is considered half of the current density during discharging for the same concentration, based on the Duck curve constraint.

Appendix B. The relative effect of activity coefficients

The relative effect of the activity coefficients on open circuit potential for the electrolytic and capacitive energy storage system (Fig. B.28), power densities (Fig. B.29) and efficiencies of ED-RED concentration battery (Fig. B.30) at different temperatures are compared to the simplified
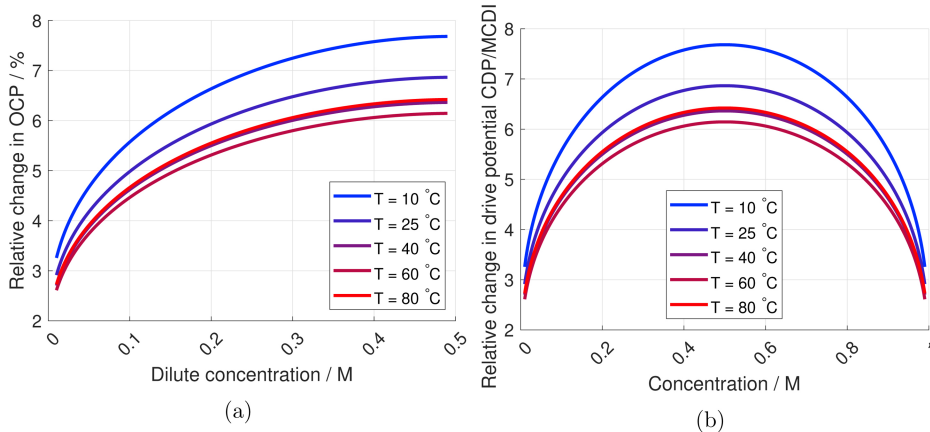

Fig. B.28. The figure shows the relative effect of the activity coefficients on open circuit potential of ED-RED (a) and MCDI-CDP (b) at different temperatures compared to the simplified assumption where concentrations are used instead of activity coefficients.

Fig. B.29. The figure shows the relative effect of the activity coefficients on power densities of ED-RED (a) and MCDI-CDP (b) at different temperatures compared to the simplified assumption where concentrations are used instead of activity coefficients.

Fig. B.30. The figure shows the relative effect of the activity coefficients on the efficiency of ED-RED (a) and MCDI-CDP (b) at different temperatures compared to the simplified assumption where concentrations are used instead of activity coefficients.
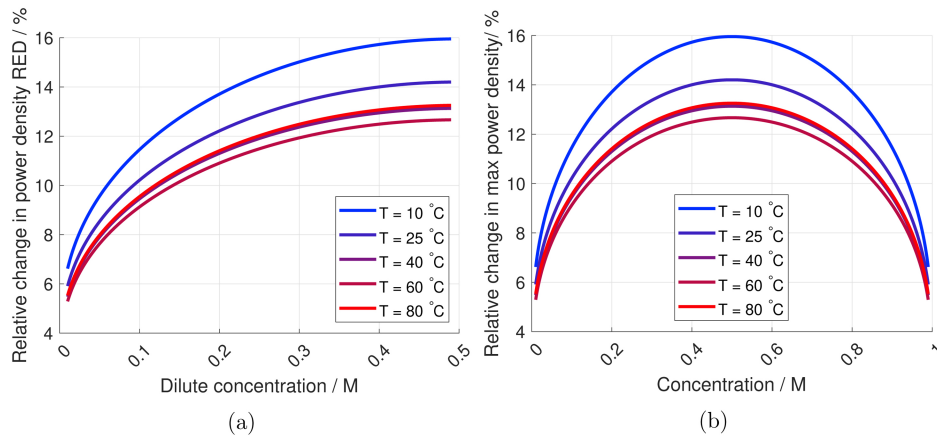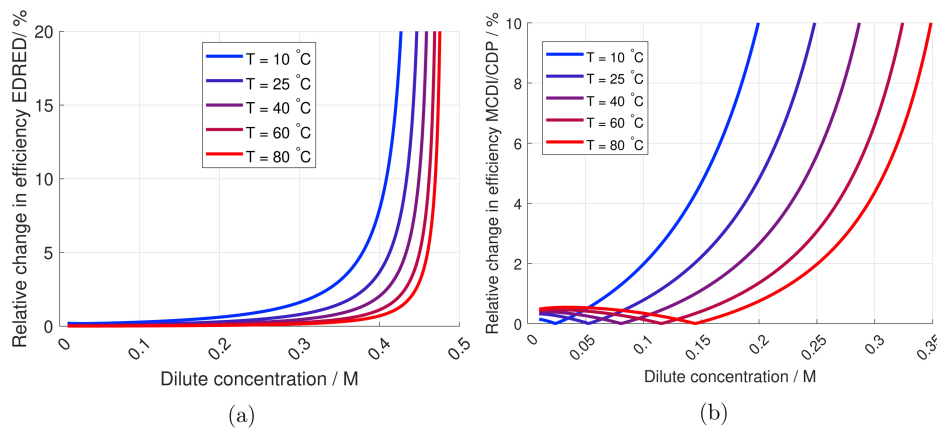
assumption where concentrations are used instead of activity coefficients. The comparison reveals that the power density at most is changing by 16% while the efficiency is not be influenced considerably.

Appendix C. Market case constraint

This study assumes that electricity prices are zero when charging and local high average market when discharging. This free charging and local high market price at discharge should be seen as a moderate market constraint and local low market prices represents non-interesting energy storage markets. This study assumes that electricity prices are zero when charging, and maximum market when discharging. This assumption should be seen as a moderate market constraint. A much more optimistic market constraint would consider on the one hand being paid to dump surplus electricity like seen, e.g. in Europe, where negative electricity prices at the extreme have enabled power to gas (dumping electricity into electrolysis and feeding hydrogen into the natural gas pipeline), and on the other hand, being paid twice (or more) the average electricity price. A pessimistic market constraint would be to consider charging prices half of discharging prices. To justify this, one must look at the difference in electric energy cost for industry and residential, where the industry over the years have had close to constant prices while the residents are on closed to increasing electric energy costs (see Fig. C.31). The difference in price development can be seen as a consequence partly because of the developing duck curve where larger industries can get power purchase agreements based on large volumes, steady load and high degree of predictability on the one hand whereas residential on the other hand represent small consumers with "inconvenient" consumer pattern along with several others.
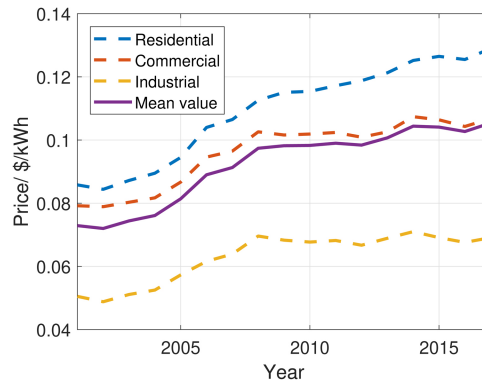
Fig. C.31. Energy prices for different sectors in USA from 2000 to 2017.

Appendix D. Update beyond the review process

This review paper has been written over a long time, in addition to a lengthy review process, and new data has come out on all three energy systems alongside. This is summarised as follows.

Recent reaches state that the ideal channel height should be 200–350 μm [86,87], while Vermass et al. [62] found the optimal channel height to be less than 100 μm. Changing to 300 μm in our model lowers the maximum RED power density up to 30% and CDP up to 20%. The power density in PRO is almost independent of channel height. Correspondingly, reducing the channel height to 100 μm increases the RED power density of RED and CDP up to 60% and 20% respectively. However; since the concentration polarisation is not included in the model, the changes in the channel height does not reflect all the losses in the power density.

The ideal open area of the spacer is found to be 80% [88], and lately (2018) the ideal open area for lowering the ED energy is found to vary with current (tested for 2% and 100% [89]). Given an increase in the open area from 0.5 to 0.8 (assuming spacershadow = 1 − openarea), the RED power density increases with up to 40%, while for CDP it increased with up to 10%. PRO power density is independent of the open area.

Water permeability for osmotic membranes typically varies between 0.41 and 10 pm/(Pa s) [90,91,4], while higher values typically decrease salt rejection. A recent study [91] demonstrates a low-pressure reverse osmosis membrane showing both high water permeability (1.51 pm/(Pa s)) and a high salt rejection (96.1%). Increasing the water permeability from 0.41 to 1.51 pm/(Pa s) increases the maximum power density from PRO with 70%.

The membrane conductivity varies a lot with membrane type. Porada et al. and Güler et al. summarised properties from over 20 different ion exchange membranes, where the membrane resistance was varying between 0.8 and 17 $\Omega \, cm^2$ [92,93]. Given a membrane resistance of 0.8 $\Omega \, cm^2$, increase the RED and CDP power density with up to 10% and 1% respectively. Increasing the membrane resistance to 17 $\Omega \, cm^2$ decreases the RED and CDP power density with up to 80% and 50% respectively. The membrane permselectivity decreases with concentration difference [40], but in the relevant concentration range according to this article, the permselectivity does not deviate much from 1.

It should be highlighted that this is an active field of research where the power and efficiency are always improving, further increasing the potential for these kinds of technologies.

References

[1] R. Pattle, Production of electric power by mixing fresh and salt water in the hydroelectric pile, Nature 174 (4431) (1954) 660.

[2] J.W. Post, J. Veerman, H.V. Hamelers, G.J. Euverink, S.J. Metz, K. Nymeijer, C.J. Buisman, Salinity-gradient power: evaluation of pressure-retarded osmosis and reverse electrodialysis, J. Membr. Sci. 288 (1) (2007) 218–230.

[3] J. Post, C. Goeting, J. Valk, S. Goinga, J. Veerman, H. Hamelers, P. Hack, Towards implementation of reverse electrodialysis for power generation from salinity gradients, Desalination Water Treat. 16 (1–3) (2010) 182–193.

[4] G.Z. Ramon, B.J. Feinberg, E.M. Hoek, Membrane-based production of salinity-gradient power, Energy Environ. Sci. 4 (11) (2011) 4423–4434.

[5] DNV-GL, Energy Transition Outlook 2017, DNV-GL, 2017.

[6] O.S. Burheim, Engineering Energy Storage, Academic Press, 2017.

[7] P. Denholm, M. O'Connell, G. Brinkman, J. Jorgenson, Overgeneration from Solar Energy in California: A Field Guide to the Duck Chart, (2015).

[8] R.S. Kingsbury, K. Chu, O. Coronell, Energy storage by reversible electrodialysis: the concentration battery, J. Membr. Sci. 495 (2015) 502–516.

[9] B. Dunn, H. Kamath, J.-M. Tarascon, Electrical energy storage for the grid: a battery of choices, Science 334 (6058) (2011) 928–935.

[10] N. Boon, R. Van Roij, Blue energy from ion adsorption and electrode charging in sea and river water, Mol. Phys. 109 (7-10) (2011) 1229–1241.

[11] J. Maisonneuve, P. Pillay, C.B. Laflamme, Pressure-retarded osmotic power system model considering non-ideal effects, Renew. Energy 75 (2015) 416–424.

[12] S. Senthil, S. Senthilmurugan, Reverse osmosis-pressure retarded osmosis hybrid system: modelling, simulation and optimization, Desalination 389 (2016) 78–97.

[13] M.F.M. Bijmans, O.S. Burheim, M. Bryjak, A. Delgado, P. Hack, F. Mantegazza, S. Tenisson, H.V.M. Hamelers, CAPMIX – deploying capacitors for salt gradient power extraction, Energy Procedia 20 (2012) 108–115, https://doi.org/10.1016/j.egypro.2012.03.013.

[14] M. Fernández, R. Wagterveld, S. Ahualli, F. Liu, A. Delgado, H. Hamelers, Polyelectrolyte- versus membrane-coated electrodes for energy production by capmix salinity exchange methods, J. Power Sources 302 (2016) 387–393.

[15] M.C. Hatzell, K.B. Hatzell, B.E. Logan, Using flow electrodes in multiple reactors in series for continuous energy generation from capacitive mixing, Environ. Sci. Technol. Lett. 1 (12) (2014) 474–478.

[16] M. Turek, B. Bandura, Renewable energy by reverse electrodialysis, Desalination 205 (1–3) (2007) 67–74, https://doi.org/10.1016/j.desal.2006.04.041.

[17] A. Daniilidis, D.A. Vermaas, R. Herber, K. Nijmeijer, Experimentally obtainable energy from mixing river water, seawater or brines with reverse electrodialysis, Renew. Energy 64 (2014) 123–131.

[18] N.Y. Yip, D. Brogioli, H.V. Hamelers, K. Nijmeijer, Salinity gradients for sustainable energy: primer, progress, and prospects, Environ. Sci. Technol. 50 (22) (2016) 12072–12094.

[19] W.J. van Egmond, U.K. Starke, M. Saakes, C.J.N. Buisman, H.V.M. Hamelers, Energy efficiency of a concentration gradient flow battery at elevated temperatures, J. Power Sources 340 (2017) 71–79, https://doi.org/10.1016/j.jpowsour.2016.11.043.

[20] L. Li, P. Liu, Z. Li, X. Wang, A multi-objective optimization approach for selection of energy storage systems, Comput. Chem. Eng. 115 (2018) 213–225.

[21] E.S. Skilbred, K.W. Krakhella, I.J.M. Haga, J.G. Pharoah, M. Hillestad, G. del Alamo Serrano, O.S. Burheim, Heat to h₂: using waste heat to set up concentration differences for reverse electrodialysis hydrogen production, ECS Trans. 85 (2018)

20

147–161, https://doi.org/10.1149/08513.0147ecst.

[22] R. Lacey, Energy by reverse electrodialysis, Ocean Eng. 7 (1) (1980) 1–47.

[23] J.W. Post, Blue Energy: Electricity Production from Salinity Gradients by Reverse Electrodialysis, Wageningen University & Research, 2009.

[24] Z. Jalili, O.S. Burheim, K.E. Einarsrud, New insights into computational fluid dynamic modeling of the resistivity and overpotential in reverse electrodialysis, ECS Trans. 85 (13) (2018) 129–144.

[25] F. Liu, O. Schaetzle, B.B. Sales, M. Saakes, C.J. Buisman, H.V. Hamelers, Effect of additional charging and current density on the performance of capacitive energy extraction based on Donnan potential, Energy Environ. Sci. 5 (9) (2012) 8642–8650.

[26] O.S. Burheim, F. Liu, B.B. Sales, O. Schaetzle, C.J.N. Buisman, H.V.M. Hamelers, Faster time response by the use of wire electrodes in capacitive salinity gradient energy systems, J. Phys. Chem. C 116 (36) (2012) 19203–19210, https://doi.org/10.1021/jp306522g.

[27] P. Długołęcki, J. Dąbrowska, K. Nijmeijer, M. Wessling, Ion conductive spacers for increased power generation in reverse electrodialysis, J. Membr. Sci. 347 (1-2) (2010) 101–107.

[28] L. Gurreri, A. Tamburini, A. Cipollina, G. Micale, M. Ciofalo, Cfd prediction of concentration polarization phenomena in spacer-filled channels for reverse electrodialysis, J. Membr. Sci. 468 (2014) 133–148.

[29] A. Ahmad, K. Lau, M.A. Bakar, Impact of different spacer filament geometries on concentration polarization control in narrow membrane channel, J. Membr. Sci. 262 (1) (2005) 138–152.

[30] A. Achilli, T.Y. Cath, A.E. Childress, Power generation with pressure retarded osmosis: an experimental and theoretical investigation, J. Membr. Sci. 343 (1-2) (2009) 42–52.

[31] S. Lin, A.P. Straub, M. Elimelech, Thermodynamic limits of extractable energy by pressure retarded osmosis, Energy Environ. Sci. 7 (8) (2014) 2706–2714.

[32] A.P. Straub, A. Deshmukh, M. Elimelech, Pressure-retarded osmosis for power generation from salinity gradients: is it viable? Energy Environ. Sci. 9 (1) (2016) 31–48.

[33] I. Sutzkover, D. Hasson, R. Semiat, Simple technique for measuring the concentration polarization level in a reverse osmosis system, Desalination 131 (1–3) (2000) 117–127.

[34] S. Sablani, M. Goosen, R. Al-Belushi, M. Wilf, Concentration polarization in ultrafiltration and reverse osmosis: a critical review, Desalination 141 (3) (2001) 269–289.

[35] S. Kim, E.M. Hoek, Modeling concentration polarization in reverse osmosis processes, Desalination 186 (1–3) (2005) 111–128.

[36] A. Altaee, J. Zou, A.A. Alanezi, A.H. Hawari, Osmotic power plant: Process innovation and future potential, Recent Adv. Petrochem. Sci. 7 (3) (2018).

[37] A. Altaee, J. Zhou, A. Alhathal Alanezi, G. Zaragoza, Pressure retarded osmosis process for power generation: feasibility, energy balance and controlling parameters, Appl. Energy 206 (August) (2017) 303–311, https://doi.org/10.1016/j.apenergy.2017.08.195.

[38] S. Loeb, F. Van Hessen, D. Shahaf, Production of energy from concentrated brines by pressure-retarded osmosis: II. Experimental results and projected energy costs, J. Membr. Sci. 1 (1976) 249–269.

[39] G.D. Mehta, Further results on the performance of present-day osmotic membranes in various osmotic regions, J. Membr. Sci. 10 (1) (1982) 3–19.

[40] A. Zlotorowicz, R.V. Strand, O.S. Burheim, Ø. Wilhelmsen, S. Kjelstrup, The permselectivity and water transference number of ion exchange membranes in reverse electrodialysis, J. Membr. Sci. 523 (2017) 402–408, https://doi.org/10.1016/j.memsci.2016.10.003.

[41] D.A. Vermaas, E. Guler, M. Saakes, K. Nijmeijer, Theoretical power density from salinity gradients using reverse electrodialysis, Energy Procedia 20 (2012) 170–184.

[42] A. Daniilidis, R. Herber, D.A. Vermaas, Upscale potential and financial feasibility of a reverse electrodialysis power plant, Appl. Energy 119 (2014) 257–265.

[43] J. Kim, M. Wilf, J.-S. Park, J. Brown, Boron rejection by reverse osmosis membranes: national reconnaissance and mechanism study-phase 1, Tech. Rep. Georgia Institute of Technology, 2006.

[44] H. Strathmann, Electrodialysis, a mature technology with a multitude of new applications, Desalination 264 (3) (2010) 268–288.

[45] S. Pawlowski, T. Rijnaarts, M. Saakes, K. Nijmeijer, S. Crespo, Velizarov, Improved fluid mixing and power density in reverse electrodialysis stacks with Chevron-profiled membranes, J. Membr. Sci. 531 (2017) 111–121.

[46] M. Tedesco, A. Cipollina, A. Tamburini, I.D.L. Bogle, G. Micale, A simulation tool for analysis and design of reverse electrodialysis using concentrated brines, Chem. Eng. Res. Des. 93 (2015) 441–456, https://doi.org/10.1016/j.cherd.2014.05.009.

[47] Schlumberger, Resistivity of NaCl Solutions, (2017) URL https://www.google.no/url?sa=t&rct=j&q=&esrc=s&source=web&cd=1&ved=0ahUKEwir-Yax3KnXAhXJLFAKHRQVANsQFggqMAA&url=http%3A%2F%2Fwww1.uis.no%2FFag%2FLearningspace_kurs%2FPetBachelor%2Fwebpage%2Ftech%255CSchlumberger%2520charts%255C01_gen_1-1_1-5.p3.pdf&usg=AOvVaw11luS4F6p350Tr_iIh0HkD.

[48] E. ToolBox, Density of aqueous solutions of inorganic sodium salts. URL https://www.engineeringtoolbox.com/density-aqueous-solution-inorganic-sodium-salt-concentration-d_1957.html (accessed: November 2018).

[49] T. Thorsen, T. Holt, Finding hidden energy in membrane processes, Filtrat. Separ. 42 (3) (2005) 28–30.

[50] N.Y. Yip, A. Tiraferri, W.A. Phillip, J.D. Schiffman, L.A. Hoover, Y.C. Kim, M. Elimelech, Thin-film composite pressure retarded osmosis membranes for sustainable power generation from salinity gradients, Environ. Sci. Technol. 45 (10) (2011) 4360–4369, https://doi.org/10.1021/es104325z.

[51] A. Achilli, J.L. Prante, N.T. Hancock, E.B. Maxwell, A.E. Childress, Experimental results from RO-PRO: a next generation system for low-energy desalination, Environ. Sci. Technol. 48 (11) (2014) 6437–6443.

[52] D. Brogioli, Extracting renewable energy from a salinity difference using a capacitor, Phys. Rev. Lett. 103 (5) (2009) 31–34, https://doi.org/10.1103/PhysRevLett.103.058501.

[53] CAPMIX – Coordinator: Dr. IR. Martijn Bijmans, The Capacitive Principle, (2012) URL http://www.capmix.eu/project-description/the-capacitive-principle.

[54] S. Porada, D. Weingarth, H.V. Hamelers, M. Bryjak, V. Presser, P. Biesheuvel, Carbon flow electrodes for continuous operation of capacitive deionization and capacitive mixing energy generation, J. Mater. Chem. A 2 (24) (2014) 9313–9321.

[55] D. Caudle, J. Tucker, J. Cooper, B. Arnold, A. Papastamataki, Electrochemical demineralization of water with carbon electrodes: research and development progress, United States Department of the Interior, 1966, p. 190.

[56] Y. Oren, Capacitive deionization (cdi) for desalination and water treatment – past, present and future (a review), Desalination 228 (1) (2008) 10–29.

[57] S. Porada, R. Zhao, A. Van Der Wal, V. Presser, P. Biesheuvel, Review on the science and technology of water desalination by capacitive deionization, Prog. Mater. Sci. 58 (8) (2013) 1388–1442.

[58] B.B. Sales, M. Saakes, J.W. Post, C.J.N. Buisman, P.M. Biesheuvel, H.V.M. Hamelers, Direct power production from a water salinity difference in a membrane-modified supercapacitor flow cell, Environ. Sci. Technol. 44 (14) (2010) 5661–5665, https://doi.org/10.1021/es100852a.

[59] R. Rica, R. Ziano, D. Salerno, F. Mantegazza, R. van Roij, D. Brogioli, Capacitive mixing for harvesting the free energy of solutions at different concentrations, Entropy 15 (4) (2013) 1388–1407, https://doi.org/10.3390/e15041388.

[60] M.C. Hatzell, R.D. Cusick, B.E. Logan, Capacitive mixing power production from salinity gradient energy enhanced through exoelectrogen-generated ionic currents, Energy Environ. Sci. 7 (3) (2014) 1159–1165.

[61] O. Burheim, B. Sales, O. Schaetzle, F. Liu, H. Hamelers, Auto generative capacitive mixing for power conversion of sea and river water by the use of membranes, ASME 2011 International Mechanical Engineering Congress and Exposition, American Society of Mechanical Engineers, 2011, pp. 483–492.

[62] D.A. Vermaas, M. Saakes, K. Nijmeijer, Doubled power density from salinity gradients at reduced intermembrane distance, Environ. Sci. Technol. 45 (16) (2011) 7089–7095, https://doi.org/10.1021/es2012758.

[63] F.C. Store, fumasep FAS-30, (2018) URL http://www.fuelcellstore.com/fumasep-fas-30.

[64] F.C. Store, fumasep FKS-30, (2018) URL http://www.fuelcellstore.com/fumasep-fks-30?search=fks%2030.

[65] B.B. Sales, F. Liu, O. Schaetzle, C.J. Buisman, H.V. Hamelers, Electrochemical characterization of a supercapacitor flow cell for power production from salinity gradients, Electrochim. Acta 86 (2012) 298–304.

[66] Electricity Price Statistics, URL http://ec.europa.eu/eurostat/statistics-explained/index.php/Electricity_price_statistics (accessed: 10.9.2017).

[67] Table 5.6.a. Average price of electricity to ultimate customers by end-use sector, URL https://www.eia.gov/electricity/monthly/epm_table_grapher.php?t=epmt_5_06_a (accessed: 10.9.2017).

[68] B. Van der Bruggen, C. Vandecasteele, Modelling of the retention of uncharged molecules with nanofiltration, Water Res. 36 (5) (2002) 1360–1368.

[69] M. Pirsaheb, T. Khosravi, K. Sharafi, M. Mouradi, Comparing operational cost and performance evaluation of electrodialysis and reverse osmosis systems in nitrate removal from drinking water in Golshahr, Mashhad, Desalination Water Treat. 57 (12) (2016) 5391–5397.

[70] ED vs. RO: The Benefits Of Electrodialysis For Desalination, https://www.wateronline.com/doc/ed-vs-ro-the-benefits-of-electrodialysis-for-desalination-0001 (accessed: 27.6.2018).

[71] Nafion Westerling Perfluorinated Membrane, http://www.sigmaaldrich.com/catalog/product/aldrich/274674?lang=en&region=NO (accessed: 7.2.2016).

[72] A. Achilli, A.E. Childress, Pressure retarded osmosis: from the vision of Sidney Loeb to the first prototype installation – review, Desalination 261 (3) (2010) 205–211, https://doi.org/10.1016/j.desal.2010.06.017.

[73] Z. Jalili, J.G. Pharoah, O. Stokke Burheim, K.E. Einarsrud, Temperature and velocity effects on mass and momentum transport in spacer-filled channels for reverse electrodialysis: a numerical study, Energies 11 (8) (2018).

[74] X. Luo, X. Cao, Y. Mo, K. Xiao, X. Zhang, P. Liang, X. Huang, Power generation by coupling reverse electrodialysis and ammonium bicarbonate: implication for recovery of waste heat, Electrochem. Commun. 19 (2012) 25–28.

[75] A.M. Benneker, T. Rijnaarts, R.G. Lammertink, J.A. Wood, Effect of temperature gradients in (reverse) electrodialysis in the ohmic regime, J. Membr. Sci. 548 (2018) 421–428, https://doi.org/10.1016/j.memsci.2017.11.029 URL http://www.sciencedirect.com/science/article/pii/S0376738817327394.

[76] Y. Mei, C.Y. Tang, Co-locating reverse electrodialysis with reverse osmosis desalination: synergies and implications, J. Membr. Sci. 539 (March) (2017) 305–312, https://doi.org/10.1016/j.memsci.2017.06.014.

[77] D.D. Anastasio, J.T. Arena, E.A. Cole, J.R. McCutcheon, Impact of temperature on power density in closed-loop pressure retarded osmosis for grid storage, J. Membr. Sci. 479 (2015) 240–245, https://doi.org/10.1016/j.memsci.2014.12.046.

[78] J. Van der Hoek, D. Rijnbende, C. Lokin, P. Bonne, M. Loonen, J. Hofman, Electrodialysis as an alternative for reverse osmosis in an integrated membrane system, Desalination 117 (1) (1998) 159–172.

[79] J. Fan, A.G. Wright, B. Britton, T. Weissbach, T.J. Skalski, J. Ward, T.J. Peckham, S. Holdcroft, Cationic polyelectrolytes, stable in 10 m Kohaq at 100 ℃, ACS Macro Lett. 6 (10) (2017) 1089–1093.

[80] S. Mrayed, D. Maccioni, G. Leslie, Efficiency of membrane distillation to produce fresh water, Int. J. Chem. Mol. Nucl. Mater. Metall. Eng. 7 (12) (2013) 991–995.

6.0   Paper I | **77**

[81] X. Zhang, Y. Liu, X. Wen, C. Li, X. Hu, Low-grade waste heat driven desalination with an open loop heat pipe, Energy 163 (2018) 221–228.

[82] V. Chintala, S. Kumar, J.K. Pandey, A technical review on waste heat recovery from compression ignition engines using organic rankine cycle, Renew. Sustain. Energy Rev. 81 (2018) 493–509.

[83] B.-S. Park, M. Usman, M. Imran, A. Pesyridis, Review of organic Rankine cycle experimental data trends, Energy Convers. Manage. 173 (2018) 679–691.

[84] F. Liu, T.F. Donkers, R.M. Wagterveld, O. Schaetzle, M. Saakes, C.J. Buisman, H.V. Hamelers, Parallel up-scaling of capacitive mixing (capmix) system enhances the specific performance, Electrochim. Acta 187 (2016) 104–112.

[85] L. Agartan, B. Akuzum, T. Mathis, K. Ergenekon, E. Agar, E.C. Kumbur, Influence of thermal treatment conditions on capacitive deionization performance and charge efficiency of carbon electrodes, Sep. Purif. Technol. 202 (2018) 67–75.

[86] S.R. Shah, N.C. Wright, P.A. Nepsky, A.G. Winter, Cost-optimal design of a batch electrodialysis system for domestic desalination of brackish groundwater, Desalination 443 (May) (2018) 198–211, https://doi.org/10.1016/j.desal.2018.05.010.

[87] K.M. Chehayeb, D.M. Farhat, K.G. Nayar, J.H. Lienhard, Optimal design and operation of electrodialysis for brackish-water desalination and for high-salinity brine concentration, Desalination 420 (June) (2017) 167–182, https://doi.org/10.1016/j.desal.2017.07.003.

[88] H.-K. Kim, M.-S. Lee, S.-Y. Lee, Y.-W. Choi, N.-J. Jeong, C.-S. Kim, High power density of reverse electrodialysis with pore-filling ion exchange membranes and a high-open-area spacer, J. Mater. Chem. A 3 (31) (2015) 16302–16306.

[89] S. Porada, W.J. van Egmond, J.W. Post, M. Saakes, H.V. Hamelers, Tailoring ion exchange membranes to enable low osmotic water transport and energy efficient electrodialysis, J. Membr. Sci. 552 (February) (2018) 22–30, https://doi.org/10.1016/j.memsci.2018.01.050.

[90] Z.L. Cheng, X. Li, T.-S. Chung, The forward osmosis-pressure retarded osmosis (FO-PRO) hybrid system: a new process to mitigate membrane fouling for sustainable osmotic power generation, J. Membr. Sci. 559 (2018) 63–74.

[91] T. Yang, C.F. Wan, J. Xiong, T.-S. Chung, Pre-treatment of wastewater retentate to mitigate fouling on the pressure retarded osmosis (PRO) process, Sep. Purif. Technol. (2019).

[92] S. Porada, W. van Egmond, J. Post, M. Saakes, H. Hamelers, Tailoring ion exchange membranes to enable low osmotic water transport and energy efficient electrodialysis, J. Membr. Sci. 552 (2018) 22–30.

[93] E. Güler, R. Elizen, D.A. Vermaas, M. Saakes, K. Nijmeijer, Performance-determining membrane properties in reverse electrodialysis, J. Membr. Sci. 446 (2013) 266–276.

[94] Y.D. Raka, H. Karoliussen, K.M. Lien, O.S. Burheim, Opportunities and challenges for thermally driven hydrogen production using reverse electrodialysis system, Int. J. Hydro. Energy (2019) revised manuscript.

PAPER II

Article

Heat to H₂: Using Waste Heat for Hydrogen Production through Reverse Electrodialysis

Kjersti Wergeland Krakhella [1,2,*] ⓘ**, Robert Bock** [2]**, Odne Stokke Burheim** [2] **and Frode Seland** [1] **and Kristian Etienne Einarsrud** [1,*] ⓘ

[1]   Department of Materials Science and Engineering, Norwegian University of Science and Technology (NTNU), NO-7491 Trondheim, Norway

[2]   Department of Energy and Process Engineering, Norwegian University of Science and Technology (NTNU), NO-7491 Trondheim, Norway

*   Correspondence: kjersti.s.krakhella@ntnu.no (K.W.K.); kristian.e.einarsrud@ntnu.no (K.E.E.)

check for updates

Abstract: This work presents an integrated hydrogen production system using reverse electrodialysis (RED) and waste heat, termed Heat to H₂. The driving potential in RED is a concentration difference over alternating anion and cation exchange membranes, where the electrode potential can be used directly for water splitting at the RED electrodes. Low-grade waste heat is used to restore the concentration difference in RED. In this study we investigate two approaches: one water removal process by evaporation and one salt removal process. Salt is precipitated in the thermally driven salt removal, thus introducing the need for a substantial change in solubility with temperature, which KNO_3 fulfils. Experimental data of ion conductivity of K^+ and NO_3^- in ion-exchange membranes is obtained. The ion conductivity of KNO_3 in the membranes was compared to NaCl and found to be equal in cation exchange membranes, but significantly lower in anion exchange membranes. The membrane resistance constitutes 98% of the total ohmic resistance using concentrations relevant for the precipitation process, while for the evaporation process, the membrane resistance constitutes over 70% of the total ohmic resistance at 40 °C. The modelled hydrogen production per cross-section area from RED using concentrations relevant for the precipitation process is 0.014 ± 0.009 m³ h⁻¹ (1.1 ± 0.7 g h⁻¹) at 40 °C, while with concentrations relevant for evaporation, the hydrogen production per cross-section area was 0.034 ± 0.016 m³ h⁻¹ (2.6 ± 1.3 g h⁻¹). The modelled energy needed per cubic meter of hydrogen produced is 55 ± 22 kWh (700 ± 300 kWh kg⁻¹) for the evaporation process and 8.22 ± 0.05 kWh (104.8 ± 0.6 kWh kg⁻¹) for the precipitation process. Using RED together with the precipitation process has similar energy consumption per volume hydrogen produced compared to proton exchange membrane water electrolysis and alkaline water electrolysis, where the energy input to the Heat to H₂-process comes from low-grade waste heat.

Keywords: hydrogen production; reverse electrodialysis; waste heat

1. Introduction

Renewable energy sources, like wind, solar, and wave energy, are often intermittent and not available when and where they are needed. The mismatch between energy production and consumption can be solved by introducing energy storage. One promising energy storage technology is hydrogen production through water electrolysis. Due to low-grade waste heat being readily available (20 TWh in Norway alone [1–3]), and the high power density from reversed electrodialysis [4], this article suggests a concept of using waste heat to produce hydrogen through reverse electrodialysis (RED).

In reverse electrodialysis energy is converted from potential energy stored in two solutions with different concentrations to electrical energy. The ions migrate from the concentrated to the dilute solution, and due to the alternating AEM and CEM, the anions and cations migrate in opposite directions inside the RED stack resulting in a net ionic current [5,6]. The concentration difference between the outlet solutions is lower than the concentration difference of the inlet solutions.

The first research on RED was conducted in the 1950s, where all the first experiments were done with NaCl concentrations similar to sea and river water [5–8]. The use of naturally occurring salt solutions is affordable but introduces bio-fouling of the membranes, or the use of energy-intensive pre-treatments of the solutions. Recirculating the salt solutions enable for a greater variety of salts, and by not using naturally occurring solutions (like sea and river), the bio-fouling of membranes can be avoided.

Closed-loop RED systems, using heat to separate the outlet solutions to the initial concentrations, have already been suggested in the literature. Tamburini et al. [9] suggested multiple separation techniques both for water and salt extraction. For water extraction they suggested separation by evaporation with multi-effect distillation and membrane distillation, using an azeotropic mixture to lower the evaporation temperature and forward osmosis [9]. Among the salt extraction techniques, Tamburini et al. [9] suggested a thermolytic salt (ammonium bicarbonate—AmB), where the salt is evaporated. The technique of evaporating the salt is also presented by other authors [10–12], where Raka et al. [10] found the energy needed per kg hydrogen produced to be 105–480 kWh. Membrane distillation as a separation technique with RED is also mentioned by Long et al., using sodium chloride [13].

Hydrogen production from RED has also been presented earlier. Nam et al. [14], Luo et al. [15] and Hatzel et al. [16] examined hydrogen production using AmB. Nam et al. produced hydrogen from microbial reverse electrodialysis cells (MRECs) and AmB [14]. Luo et al. optimised the cell stack further for MRECs and AmB [15]. Hatzel et al. examined hydrogen production using different operational currents, and compared it to the hydrogen production using the energy from RED together with an external water electrolysis cell [16]. In the area of salt removal for solutions, the most used salt is AmB.

Scope of This Paper

This paper describes two concepts for regenerating the concentrations used in RED by a thermal separation unit. A general system schematic is shown in Figure 1. The first concept is to precipitate salt from the dilute solution from RED, and the second concept is to evaporate water from the outlet concentrated solution. For the first concept, a salt with a pronounced saturation concentration temperature dependency (SCTD) is needed. The most common salt to use in RED, NaCl, does not have a sufficient SCTD, and thus the relevant concentrations will not give a sufficient voltage over the membrane using the precipitation system. A better alternative is KNO_3 with a more significant change in solubility with temperature than NaCl, allowing for a larger concentration difference and a higher voltage over the membrane.

Most research on RED and ion exchange membranes (IEM) is reported for low NaCl concentrations or for AmB when waste heat is used for separation. As discussed in the next section, one of the larger contributors to the ohmic losses in RED is the ohmic resistance in the membranes. As a proof of concept for using KNO_3 as salt in RED, conductivity measurements of AEM and CEM soaked in KNO_3 at 23 °C and 40 °C were performed for concentrations close to saturation point, and compared with NaCl at the same concentrations and temperatures.

The current work is an extension and realization of preliminary concepts presented by the authors earlier [17]. The new and refined measurements of membrane conductivity presented in the following, combined with a more extensive theoretical framework enables lower uncertainties than what was presented before. Furthermore, an energy evaluation of the two processes allows for a broader comparison with other technologies, which was lacking in [17].
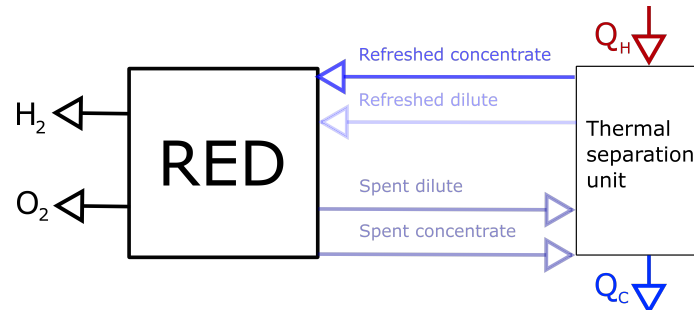
Figure 1. Reversing the spent concentrations from RED using a thermal separation unit.

2. Concepts

This work presents a concept of a RED stack that recirculates the salt solutions in a closed loop. This requires the spent solutions to be recovered to their initial concentrations. The concepts presented here, rely on the use of low-temperature waste heat by employing phase change separation techniques, making low-grade heat the only consumable in the closed loop RED system. Due to different achievable concentration differences with the two techniques, the driving potential will differ, and thereby the peak power current and hydrogen production.

2.1. Salt Extraction by Precipitation

Thermal energy is removed from the dilute solution by precipitating salt from the solution. The salt slurry is transported from the dilute and added to the concentrated outlet solution where it dissolves, as illustrated in Figure 2. The transportation is envisioned to take place in an Archimedes pump or screw pump-based transport unit where a slurry of the precipitate is continuously in motion to avoid accumulation and solid precipitation of salt.
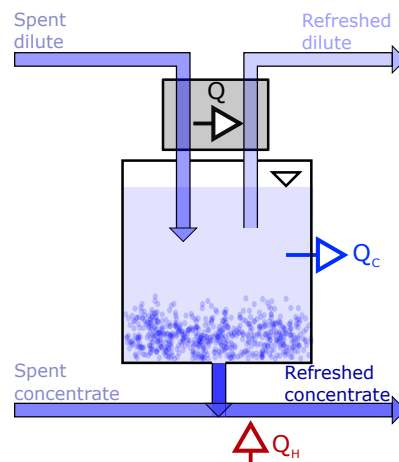
Figure 2. Illustration of the thermal separation unit (in Figure 1) using precipitation. Thermal energy is removed from the spent dilute solution (Q_C), to precipitate salt. Thermal energy (Q_H) is added to the spent concentrated solution after the salt slurry is added.

The amount of precipitated salt is dependent on the concentration of outlet dilute solution and solubility limit at the temperature the separation process is operated at. The concentration of the dilute inlet solution is therefore limited by the solubility of salt at the temperature used in the

precipitation process. To minimise energy consumption while cooling, natural cooling systems can be used, e.g., seawater, at a temperature around 10 °C.

The main contributor to the energy input needed for the precipitation concept is the heating of the salt slurry from the cooling (10 °C) to the operating temperature in the RED stack (40 °C), and the energy needed for dissolving the precipitated salt. To save energy, heat from the spent dilute solution, can be exchanged with the refreshed dilute solution, as shown by the heat flux, *Q*, in Figure 2.

2.2. Water Extraction by Evaporation

A sketch of a principle separation system using evaporation is shown in Figure 3. The spent concentrate solution is decompressed until the water evaporates with limited need for external thermal energy (*Q*). External low-grade heat, Q_H, is added to the vapor to keep the gas form condensing before the gas is compressed. The gas transfers thermal energy to the spent concentrate solution to maintain the temperature, represented by *Q* in Figure 3. The evaporation will continue until the initial concentration in the solution is recovered, where the evaporated water is added to the outlet dilute solution from the cell. Pumps are needed in to depressurize the container.

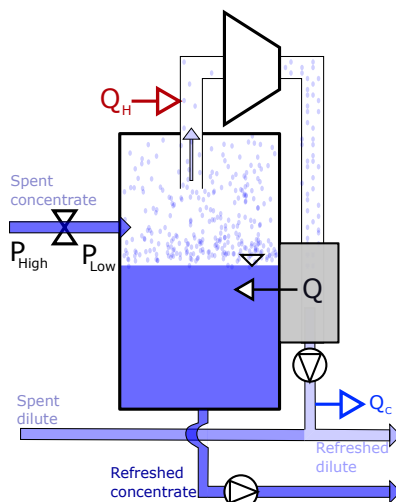**Figure 3.** Illustration of the thermal separation unit (in Figure 1) using evaporation. The spent concentrated solution from RED, is decompressed to a lower evaporation temperature, before heat (Q) is added and water evaporated from the spent dilute solution. The vaporised water is heated (Q_H) and compressed, before thermal energy is exchanged with the spent concentrated, and the vaporised water is condensed back to a liquid and added to the spent dilute solutions.

This separation technique needs more substantial quantities of thermal energy than the precipitation, where the main energy consumption in this separation process is the evaporation of the water. The heat exchange is also a disadvantage for the energy calculation.

2.3. Temperature and Concentration Limitaitons

The limitation on the temperature stems from the membrane since commercial membranes can typically withstand maximum 40 °C [18,19], some up to 80 °C. The membranes used in the experiments reported here can only operate up to 40 °C; therefore, 40 °C is set as the operating temperature for the RED cell.

The concentration of the concentrated inlet solution in RED is limited by the solubility of the salt at the RED operating temperature (40 °C), but due to more documented data in the literature at room temperature, all measurements and modeling are also carried out at 23 °C for reference.

The concentration for the dilute solution in RED, when using precipitation as the separation technique, is set by the solubility of the salt at the temperature used in the separation (10 °C). The solubility of KNO$_3$ and NaCl is found from CRC Handbook [20] (unit: wt% per mass solution) and calculated to molality (formula in [20]). The data is plotted in Figure 4.
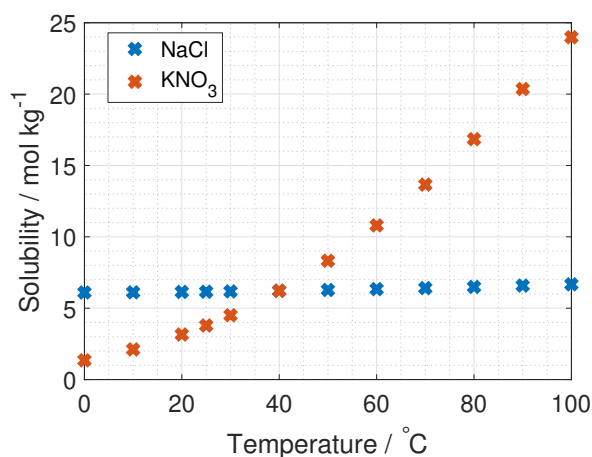

Figure 4. Solubility dependency on temperature for NaCl and KNO$_3$ [20].

The solubility for KNO$_3$ is 2.11, 3.16 and 6.22 mol kg^{-1} at 10 °C, 25 °C and 40 °C respectively, and 6.11, 6.15 and 6.22 mol kg^{-1} at 10 °C, 25 °C and 40 °C respectively for NaCl. The relevant dilute concentration for the evaporation process is not limited by solubility, but optimised for maximum hydrogen production with modeling.

For the precipitation process using the most common salt for RED, NaCl, the dilute concentration should be 6.1 mol kg^{-1} and the concentrated concentration should be 6.2 mol kg^{-1}, while using KNO$_3$, the dilute concentration should be 2.1 mol kg^{-1} and the concentrated solution should be 6.2 mol kg^{-1} [20]. This corresponds to a driving potential that is over 60 times higher for KNO$_3$ than that for NaCl (activity coefficient and permselectivity assumed equal to unity). However; the cost of KNO$_3$ is almost twice that of NaCl [21], so other more affordable salts can be considered for future work. KNO$_3$ was chosen as a proof of concept due to its significant change in saturation concentration with temperature and low cost. Other salts (such as CaCl$_2$, NaOH and NaNO$_3$) may also be relevant alternatives, granted they possess a high saturation concentration temperature dependency, reasonable cost and an improved permselectivity.

The concentration difference between the dilute and concentrated inlet solution can be larger in the evaporation system compared to the precipitation system, since there is no restriction on the dilute solution, improving the driving potential.
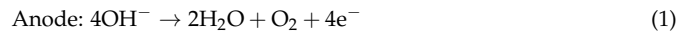
3. Theory

An illustration of a RED stack is given in Figure 5. Ions migrate both ways through the membranes, but more ions are available for migration from the concentrated solution to the dilute solution than vice versa, inducing a net ionic current of anions towards the anode and net current of cations towards the cathode.
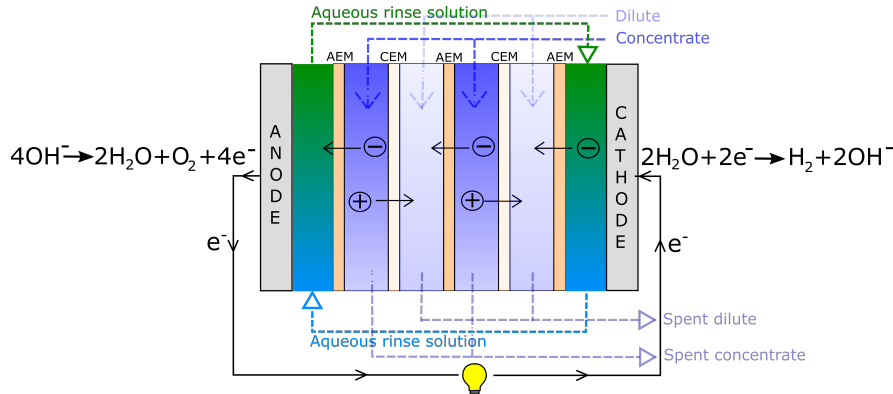
Figure 5. Illustration of a RED-cell. Hydrogen is produced at the cathode and oxygen at the anode.

By stacking the membranes, as shown in Figure 5, the voltage can be increased enough to enable water splitting (in the aqueous rinse solution) [22,23]. The water splitting reactions (also given in the figure) are:

$$\text{Anode: } 4\text{OH}^- \rightarrow 2\text{H}_2\text{O} + \text{O}_2 + 4\text{e}^- \tag{1}$$

$$\text{Cathode: } 4\text{H}_2\text{O} + 4\text{e}^- \rightarrow 2\text{H}_2 + 4\text{OH}^- \tag{2}$$

3.1. Driving Voltage

The open-circuit voltage (OCV) or the Donnan voltage, E_{OCV}, over a RED unit cell is given by the Nernst equation:

$$E_{\text{OCV}} = 2\bar{\alpha}\frac{RT}{zF}\ln\left(\frac{b_c\gamma_c}{b_d\gamma_d}\right) \tag{3}$$

where $\bar{\alpha}$ is the mean permselectivity of the AEM and CEM in the unit cell, R is the ideal gas constant, T is the temperature in Kelvin, z is the valence number of the ions transported, F is Faraday's constant, and b_c/b_d and γ_c/γ_d are the concentration and activity coefficients of the concentrated/dilute solution, respectively [24].

The ratio of the activity coefficients are often assumed unity. However, due to concentrations close to the salt saturation point, the Stokes–Robinson equation is used for the calculation of the solution activity coefficient [25,26]:

$$\gamma_{\pm} = exp\left(\frac{Az_{\pm}^2\sqrt{I}}{1 + Ba_{\text{KNO}_3}\sqrt{I}} - \frac{h}{\nu}\ln(a_w) - \ln(|1 + (M_w(\nu - h)b)|)\right) \tag{4}$$

where I is the ionic strength (reference: 1 mole salt per kg solvent). $z_{\pm}^2$ is the mean of the valence of the cation and anion (1 for KNO_3), M_w is the molar mass of water (0.018 kg mol^{-1}), ν is the number of ions per molecule (2 for KNO_3) and a_{KNO_3} is the distance of the closest approach, which is dependent on the kinetic energy of the ions, thereby also the concentration and temperature of the solution. For simplicity, a_{KNO_3} is set constant with temperature and concentration, and found from curve fitting of data from Dash et al. and Marcos-Arroyo et al. [27,28] to Equation (4), and found to be 1.1 Å. The hydration number, h, is found to have a dependence on temperature and concentration [29]. Afanasiev et al. [30] suggest an exponential dependence on concentration and negligible dependence on temperature, while Onori [31] gives a linear dependence on concentration and states that the hydration number is dependent on temperature. For simplicity, h for KNO_3 is set constant with temperature and concentration and taken to be the mean value from Lu et al. [32]: 5.

In Equation (4), A and B are temperature dependent constants given in Equation (5) (at 25 °C $A = 1.18$ (kg mol^{-1})$^{1/2}$ and $B = 3.29 \times 10^9$ (kg mol^{-1})$^{1/2}$m^{-1} [33]).

$$
\begin{aligned}
A &= (2\pi N_A \rho_w)^{1/2} \left(\frac{e_0^2}{4\pi \epsilon_0 \epsilon_{r,w} k_B T} \right)^{3/2} \\
B &= e \left(\frac{2 N_A \rho_w}{\epsilon_0 \epsilon_{r,w} k_B T} \right)^{1/2},
\end{aligned}
\tag{5}
$$

where N_A is Avogadro constant, ρ_w is the density of the solvent (here water and set to constant 1000 kg m^{-3} for simplicity), e_0 is the elementary charge, ϵ_0 is permittivity of vacuum, k_B is Boltzmann constant, and T is the temperature in Kelvin. $\epsilon_{r,w}$ is the dielectric constant of the solvent [34] (here water) and given in Equation (6) (rewritten to use temperature in Kelvin instead of Celsius):

$$
\epsilon_{r,w} = 87.74 - 0.4008(T - 273.2) + 9.398 \times 10^{-4}(T - 273.2)^2 - 1.410 \times 10^{-6}(T - 273.2)^3
\tag{6}
$$

In Equation (4), a_w is the water activity as a function of the salt concentration. Sangster et al. [35] measured the water activity in KNO$_3$ solutions above 3 M and extrapolated the data for concentrations down to 0 M, giving a linear trend of the water activity. An approximation of the linear equation for the water activity in a KNO$_3$ solution with molality b is given in Equation (7):

$$
a_w = 1 - 0.018b
\tag{7}
$$

To the author's knowledge, the activity coefficient of KNO$_3$ is only measured at 25 °C and up to salt concentrations of 3.5 mol kg^{-1}, by Dash et al. and Marcos-Arroyo et al. [27,28]. Their experiments were similar, but Dash et al. used double junction reference electrode, while Marcos-Arroyo et al. used single junction. The modeled activity coefficient from Stokes–Robinson equation (Equation (4)) is plotted in Figure 6 together with the data from Dash and Marcos-Arroyo.
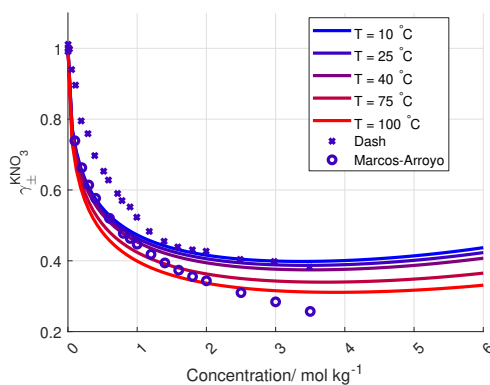
Figure 6. Modeled activity coefficient for KNO$_3$ for different concentration and temperatures, together with measured activity coefficients from [27,28].

A reason for the deviation between the Stokes–Robinson equation and the measured activity coefficient of KNO$_3$ from Dash et al. and Marcos-Arroyo et al. [27,28] is the assumption of no temperature or concentration dependency in the hydration number and the distance of closest approach in the model.

The apparent permselectivity, $\bar{\alpha}$ from Equation (3), increases with increasing concentration difference [36]. Krakhella et al. [37] measured FAS-50 and FKS-50 from Fumatech [18,19] at elevated NaCl concentrations, and found the permselectivity to vary (with concentrations) from 0.5 to 0.8.

Ji and Geise [38] found that the permselectivity of two membranes dropped by approximately 2% when the temperature increased from 14 to 31 °C. However, the Donnan voltage increases with increased temperature (Equation (3)), which was confirmed experimentally by Długołęcki et al. and Van Egmond et al. [39,40], among others.

The total voltage in a RED stack is given in Equation (8):

$$E = E_{\text{OCV}} N_{\text{uc}} - E_{\text{L}} - r i N_{\text{uc}}, \tag{8}$$

where N_{uc} is the number of unit cells, i is the current density per cross-section area and r is the unit cell area resistance given in Equation (14). E_{L} represents lumped electrode losses, including the activation overpotential losses and the ohmic losses at the electrodes. The power density gained from the RED stack is the stack voltage times the current, given in Equation (9):

$$P = E_{\text{OCV}} N_{\text{uc}} i - r N_{\text{uc}} i^2 \tag{9}$$

The voltage needed for hydrogen production is 1.23 V, while the current density is found at maximum power density, where the derivative of Equation (9) with respect to current density is zero. Using these two limitations, gives two equations with two unknowns (current and number of unit cells):

$$E_{\text{OCV}} N_{\text{uc}} - r i N_{\text{uc}} = (1.23 + E_{\text{L}}) \text{ and}$$
$$E_{\text{OCV}} N_{\text{uc}} - 2 r N_{\text{uc}} i = 0 \tag{10}$$

Solving Equation (10) gives the operating current density per unit cell area,

$$i_{P_{\max}} = \frac{E_{\text{OCV}}}{2 r_{\text{uc}}}, \tag{11}$$

and the number of unit cells needed:

$$N_{\text{uc}} = \frac{2(E_{\text{L}} + 1.23)}{E_{\text{OCV}}}. \tag{12}$$

The hydrogen production in grams per hour per cross-section area is

$$m(H_2) = \frac{3600 i_{P_{\max}} M}{2F} \tag{13}$$

where M is the molar mass of hydrogen gas (2.02 g mol^{-1}).

It is important to highlight that the total ohmic losses of the RED stack, $i r N_{\text{uc}}$, need to be (1.23 V + E_{L}) for all current densities and number of unit cells. This can be seen by solving Equation (10).

3.2. Losses

The losses considered in this work is the lumped electrode losses at the electrodes and the ohmic losses per unit cell. The Tafel losses are here considered to be a lumped loss of the activation potential and ohmic losses at the electrodes [24]. The operational current density for the RED stack is assumed small (<100 A m^{-2}), where the activation and ohmic losses at the electrodes are approximately 0.10 V (see [24], p. 156).

The ohimc losses are given in Equation (14):

$$r_{\text{uc}} = \frac{d_{\text{AEM}}}{\rho_{\text{AEM}}(1 - \beta)} + \frac{d_{\text{CEM}}}{\rho_{\text{CEM}}(1 - \beta)} + \frac{d_{\text{s}}}{\rho_{\text{d}} \epsilon^2} + \frac{d_{\text{s}}}{\rho_{\text{c}} \epsilon^2}, \tag{14}$$

where ρ_{CEM} and ρ_{AEM} are the conductivity of the AEM and CEM [S m^{-1}] respectively, d_{AEM} and d_{CEM} is the thickness of the AEM and CEM, and β is the spacer shadow (dimensionless) [39]. d is

the thickness of the spacer, ϵ (dimensionless) is the volume factor occupied by the spacer or the porosity (for no spacer: $\epsilon = 1$. For definition, see [41]). ρ_d and ρ_c are the conductivities of the dilute and concentrated solution respectively (S m^{-1}). Theoretical values for ρ_d and ρ_c are deduced from conductivity measurement from [42], where the data is fitted to Kohlrausch's equation (given in Hamann [43], p. 22) for 23 °C and 40 °C:

$$\begin{aligned}
\rho_{23\,°C,(Aq)}^{KNO_3} &= k_{1,23\,°C}b - k_{2,23\,°C}b^{3/2} \\
\rho_{40\,°C,(Aq)}^{KNO_3} &= k_{1,40\,°C}b - k_{2,40\,°C}b^{3/2}
\end{aligned} \tag{15}$$

where b is the molality, and the coefficients, $k_{1,i}$ and $k_{2,i}$, are given in Table 1. $k_{1,i}$ is equivalent to the molar conductivity of infinite dilute solution, Λ_0, and $k_{2,i}$ is a coefficient related to the stoichiometry of the electrolyte.

Table 1. Coefficients for Equation (15) with 95% conf. interval.

Name	Value
$k_{1,23\,°C}$	12.2 ± 0.3
$k_{2,23\,°C}$	3.4 ± 0.2
$k_{1,40\,°C}$	15.8 ± 0.4
$k_{2,40\,°C}$	4.5 ± 0.2

The ohmic losses in the flow compartment should be optimised with respect to hydrogen production (see Equation (13)). For wider compartments, the ohmic resistance increases, while pumping energy decreases. The ideal compartment width was found to be approximately 100 μm [44]. However, the compartment thickness in the simulations in this article is taken from Fumatechs ED-stack (given in Table 4). The solution concentration also contributes to the ohmic losses of the flow compartment, where a lower salt concentration increases the resistance (see Equation (15)). This would suggest higher concentrations on both sides of the membrane. However, a higher salt concentration gradient between the compartments enhances the RED driving potential (see Equation (3)). Optimising the solution resistance is needed for highest possible power density and hydrogen production, and varies with cell geometry and solution flow. When these factors are accounted for, the ionic resistance in the membranes is the main contributor to ohmic losses [8,45].

The energy losses in the RED-stack can be calculate from (unit Wh m^{-3} (hydrogen)):

$$W_{\text{RED-stack}} = E_{\text{RED-stack}}\frac{2pF}{3600RT}, \tag{16}$$

where $E_{\text{RED-stack}}$ is the voltage loss over the RED-stack and p is the pressure (1 atm = 101,325 Pa).

3.3. Ionic Membrane Conductivity

The ionic conductivity in the membrane in Equation (14), depends on the concentration and diffusion coefficient for both the counterions and co-ions [46] (Equation (8)). The concentration of counterions in the membranes is dependent on the fixed charges, and the amount of salt and water absorbed in the membrane pores [46,47]. The fixed charges are quantified by the ion exchange capacity (IEC) and are given as mmol g^{-1}, and are constant (per membrane weight) with concentration. By increasing the IEC, the hydrophilicity of the polymer chains in the membrane increases and with it the water uptake. Water makes the membrane swell, reducing the density of the fixed charges in the membrane and increasing the adsorption of ions in the membrane. For the two membranes used in the experiments in this article, the IEC is 1.2–1.4 for CEM and 1.6–2.0 mmol g^{-1} for AEM [18,19], indicating a slightly better conductivity in AEM than CEM.

The swelling of the membrane is also affected by the difference between the membrane concentration and the external concentration. The water uptake in the membrane does not change much with the external concentration, but if the external concentration exceeds a certain limit (the Donnan concentration of the membrane), water can diffuse from the membrane to the solution, due to osmotic forces [46], decreasing the water and salt content inside the membrane. This concentration limit is around 0.07 M for Nafion 117 [48]. The result of the swelling and de-swelling, is a flux of water and dissolved salt into the membrane at low external concentration, and a flux of water from the membrane to the external solution at high external concentration, resulting in a strictly increasing concentration of both counterion concentration and co-ions in the membrane pores with external concentration [46].

The concentration of co-ions is also affected by the Donnan voltage over the membrane/solution interface, where a lower Donnan voltage between membrane and external solution leads to higher co-ion adsorption in the membrane [46].

The other factor affecting the ion conductivity in the membrane is the diffusion coefficient [46]. For NaCl the diffusion coefficient of the counterion is reported to decrease slightly with external concentration in CEM, while in AEM, the reported data showed no effect on the concentration [47]. However, the reported data from [47] is only conducted up to 1 M NaCl. For higher concentrations, the diffusion coefficient is believed to decrease with external concentrations, due to deswelling of the membrane. Kamcev et al. found the diffusion coefficient of the counterion always to exceed the co-ion, regardless of anionic or cationic membrane [46]. This indicates a faster transport at the fixed groups than in the pores.

Smaller particles should theoretically have a higher diffusion coefficient [49]. However, a smaller ionic radius has more charges per area on the surface of the ion, bringing more water molecules with it [49], increasing the hydraulic diameter. This results in two effects on the conductivity. The first effect is increased membrane wetting, where more water increases the conductivity. The second effect is that the physically larger ion will lower the diffusion coefficient. The crystalline and the hydrated radius of Na^+, K^+, Cl^- and NO_3^- are found from [49] and given in Table 2.

Table 2. Crystal and hydrated radii of Na^+, K^+, Cl^- and NO_3^-. Data obtained from [49].

	Na^+	K^+	Cl^-	NO_3^-
Crystal radius (nm)	0.101–0.117	0.138–0.149	0.181–0.194	0.179–0.189
Hydrated radius (nm)	0.178–0.358	0.201–0.331	0.195–0.332	0.340

3.4. Electrochemical Impedance Spectrocopy

In electrochemical impedance spectroscopy (EIS), an oscillating current (or potential) is applied to the system at a specific frequency, and the amplitude and phase shift of the voltage (or current) is measured. From this, the impedance of the system can be obtained.

The system used for the present measurements is a membrane compressed between two electrodes (more details in Section 4.2). The equivalent circuit is therefore a series of the three components: the two electrode-membrane interfaces, and one membrane bulk impedance. The interface impedance between the membrane and the electrodes consists of a capacitive impedance (C_{dl}), due to the double layer, in parallel with a resistance (R_{dl}) representing the blocking interface. The membrane impedance is a bulk resistance (R_b) in parallel with a capacitor (C_b) due to the double layers building up in the pores in the membrane [50]. The total impedance is given in:

$$Z = \frac{1}{1/R_{dl,1} + i\omega C_{dl,1}} + \frac{1}{1/R_b + i\omega C_b} + \frac{1}{1/R_{dl,2} + i\omega C_{dl,2}},$$

(17)

Since no charge can pass the electrode/membrane interface, the interface impedance is merely capacitive [50]. Electrodes with a perfectly flat surface purely have a capacitive behaviour, although small irregularities in most electrodes lead to the use of a constant phase element (CPE)

instead of a capacitor when analysing the impedance. The total impedance in Equation (17) can be simplified to:

$$Z = \frac{1}{(i\omega C_{dl})^n} + \frac{1}{1/R_b + i\omega C_b} \tag{18}$$

The equivalent circuit for the electrode membrane system is given in Figure 7 and a typical Nyquist plot of the resistance is given in Figure 8 where the bulk resistance in the membrane is marked.
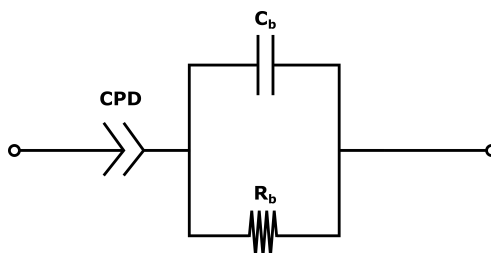

Figure 7. The equivalent circuit for a wet membrane between two electrodes.

When the frequency increases the contribution from the CPE decreases, and the contribution from the membrane increases. At a given frequency ($\approx$1 MHz), the majority of the impedance is from the membrane resistance, and the ohmic membrane resistance can be found from the Nyquist plot (see Figure 8).
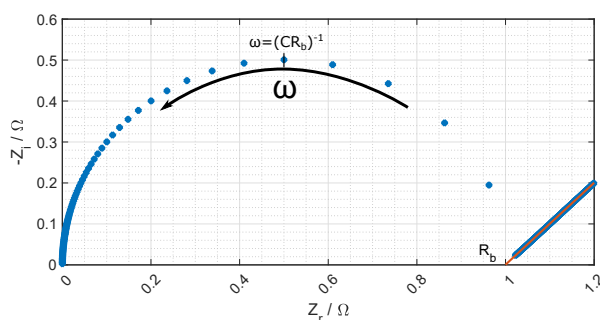

Figure 8. Nyquist plot of Equation (18), and where the ohmic resistance of the membrane is found.

4. Experimental

Two membranes from Fumatech, FAS-50 and FKS-50 [18,19], with high permselectivity (in seawater at 25 °C) are chosen for conductivity measurements with KNO$_3$. The ion conductivity is measured at 23 °C and 40 °C, where the upper limit is due to possible degradation of the membranes above 40 °C.

4.1. Membrane Preparation

FAS-50 and FKS-50 are delivered dry with the counter ions Br$^-$ and H$^+$, respectively, balancing the fixed charges [18,19]. After punching circular samples with a radius of 1 cm, six membranes were soaked in 500 mL of each concentration of KNO$_3$ for minimum 36 h. To avoid precipitation of salt (e.g., a drop in temperature before measurements start), the membrane conductivity measurements are carried out at maximum of 4.3 mol kg^{-1}. For comparison, both membrane types are soaked in the same concentration (mol kg^{-1}) NaCl.

To measure the conductivity of only the counterions, the membranes could be rinsed in deionised water to remove salt solutions from the pores in the membranes. However, for our purpose, the ion

conductivity of both the counterions and the ions dissolved in the pores in the membrane is of interest. The membranes are therefore not rinsed in deionised water before measurements.

After removed from the salt solution, the membrane thickness was measured in three different places for every sample with a micrometre and averaged, before they were placed in the setup described below.

4.2. Ion Conductivity Measurement

The cell used to measure membrane conductivity is illustrated in Figure 9. The setup contains two platinum disc electrodes with a radius of 1 cm and thickness of 1 mm, which the membrane sample is placed in between. Platinum wires are connected to the electrodes and mounted in a hard cylinder where the wires are emerging through the end. A tube is slid closely around the cylinders with the electrodes and membrane. Similar setups are standard in this kind of measurements [51,52].
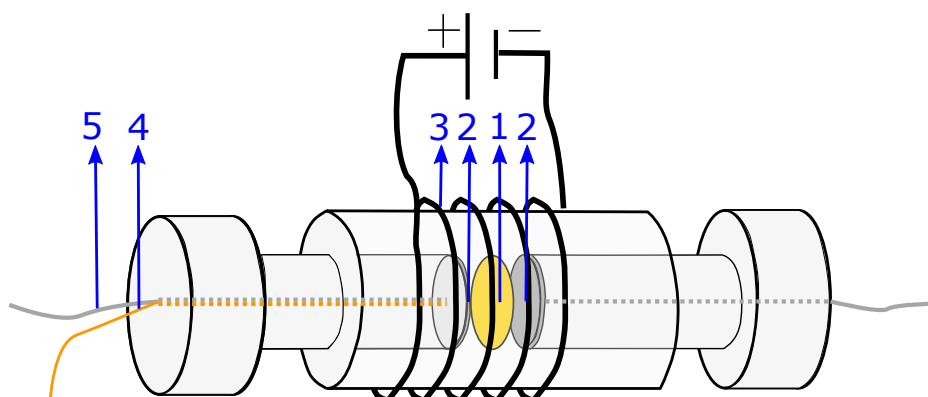
Figure 9. Sketch of the measurement cell for membrane conductivity, with (1) membrane sample(s), (2) platinum plates, (3) heating wire, (4) end of the thermocouple emerging from the cell, (5) end of the platinum wire (attached to the platinum plate) emerging from the cell.

To control the pressure on the membrane, the cylinder is placed in an (in-house made) screw clamp. The bolt (M6, hexagonal head) is tightened to a pressure of 2 Nm which is evenly distributed on the membrane due to the screw clamp.

For the measurements at 40 °C, the setup is placed in a heating cabinet, where the temperature is maintained at 40 ± 1 °C throughout the experiment. For some of the experiments at 40 °C, a heating wire was attached outside the cylinder to heat the system faster. This is illustrated in Figure 9.

Galvanostatic electrochemical impedance spectroscopy is performed with a two-electrode-setup using a Gamry Interface 5000E potentiostat. The settings used are given in Table 3.

Table 3. Galvanostatic EIS settings for the potentiostat. * rms = root mean square, $\approx 0.7 \times$ peak current.

Variable	Value
DC current [A]	0
AC current [A rms] *	0.001
Initial frequency [Hz]	1 MHz
Final frequency [Hz]	5
Points/decade	10

To eliminate changes on the electrode surface in-between the experiments, both electrodes were polarised in 1 M H_2SO_4 from 0.1 to 1.6 V_{SHE} until stable (no changes between the cycles), or minimum 30 cycles. The electrodes were also polished regularly. To account for inductance from

the hardware, an experiment without the membrane sample was conducted, where the electrodes are compressed with the same pressure as used during the experiments with the membrane samples. The resulting impedance is subtracted from the impedance found with the membrane, using the software Echem Analyst

As described in Section 3.4 , the bulk resistance of the membrane, is found at the higher frequencies (after subtracting the blank cell), where the imaginary impedance is close to zero. In many cases, the Nyquist plot showed a straight line where it was easy to read of the bulk resistance. In the cases where the data was noisy at higher frequencies, a line was drawn through the lower linear data points to find the crossing point on the real axis, as shown in Figure 10.
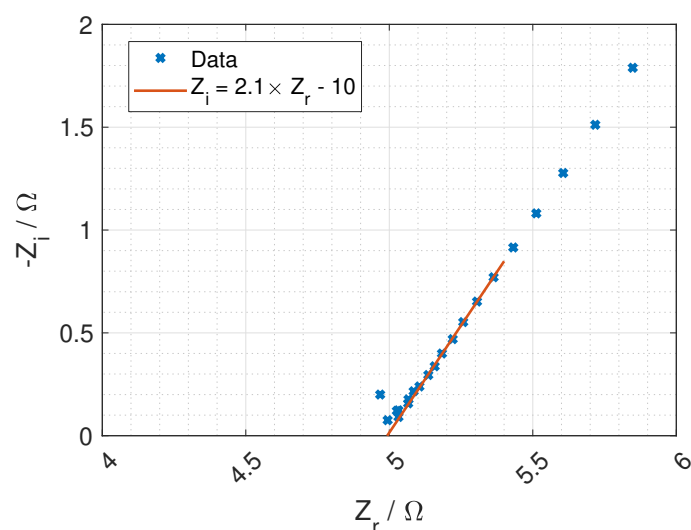

Figure 10. Impedance data with linear fit to find the crossing of the real axis.

For every concentration, temperature and membrane type (AEM and CEM), three experiments were run using 1, 3 and 5 membranes samples stacked inside the cell, to find the resistance for different thicknesses. The resistance was multiplied with the area of the membrane and plotted versus the thickness, where the slope of the graph is the resistivity (Ωm). The interface between the membranes is found to have a negligible impact on the resistance [17].

4.3. Power Density and Hydrogen Production

The unit cell power density is calculated from Equation (9), with all the input parameters given in Table 4. When plotting power density versus current density, a maximum power density can be found. The corresponding current density is used as an input to Equation (13).

As seen in Table 4 the concentrations of the concentrated solutions and the dilute solution used with the precipitation technique are set by the solubility limits. The ideal dilute concentration used with the evaporation process is set at maximum hydrogen production, which is found from calculations. The driving potential, solution resistance and power density are calculated for various dilute concentrations, giving one current density at maximum power for all the chosen dilute concentrations. The concentration giving the highest hydrogen production was chosen as the dilute concentration for the evaporation process.

Table 4. Input values used to model power density and hydrogen production from RED.

Name	Symbol	Value
Solutions		
Conc. dilute solution—evaporation	b_d^{eva}	calc. from H_2^{max}
Conc. dilute solution—precipitation (T = 10 °C)	b_d^{pre}	2.11 mol kg^{-1} *
Conc. concentrated solution (T = [25 40] °C)	b_c	[3.79 6.22] mol kg^{-1} *
Temperature	T	[297 313] K
Flow volume per unit cell	Φ	5.4×10^{-5} kg s^{-1}m^{-2} **
Membrane		
Mean permselectivity CEM and AEM	$\bar{\alpha}$	0.63–0.96 ***
Conductivity AEM	ρ_{AEM}	measured
Conductivity CEM	ρ_{CEM}	measured
Thickness AEM	d_{AEM}	50 μm
Thickness CEM	d_{CEM}	50 μm
Cell geometry		
Thickness spacer	d_s	155 μm [37]
Spacer parameters		
Shadow factor	β	0.35 [37]
Porosity	ϵ	0.84 [37]
Electrode		
Lumped electrode losses	E_L	0.10 V [24] (p. 156)
Constants		
Molar mass KNO$_3$	M	0.101 kg mol^{-1}
Molar mass H$_2$	M	0.00202 kg mol^{-1}
Faraday's constant	F	96,485 C mol^{-1}
Universal gas constant	R	8.314 J K^{-1}mol^{-1}

* solubility limit for KNO$_3$ at the given temperatures. ** recomended for the ED cell from Fumatech. *** no data for KNO$_3$, but datasheet reported a mean of 0.96 for 0.5 M for NaCl [18,19] and Ref. [37] reported a mean permselectivity from 0.63–0.76 at elevated concentrations of NaCl.

4.4. Energy Used in Solution Separation

The mass balance in the two separations systems needs to be calculated to find the energy used. In the assumption that no water is crossing the membrane, the water content of both the inlet and outlet flow are the same, for both the concentrated and dilute solution (given in Table 4). The concentration (mol kg^{-1}) of the outlet solutions from RED, is dependent on the hydrogen production:

$$
\begin{aligned}
b_c^{outlet} &= \frac{\dot{n}_c^{inlet} - 2\dot{n}_{H_2}}{\Phi_w} = \frac{b_c^{inlet}\Phi_w - 2\dot{n}_{H_2}}{\Phi_w} \\
b_d^{outlet} &= \frac{\dot{n}_d^{inlet} + 2\dot{n}_{H_2}}{\Phi_w} = \frac{b_d^{inlet}\Phi_w + 2\dot{n}_{H_2}}{\Phi_w}
\end{aligned}
\tag{19}
$$

where Φ_w is the flow of water per second per cross-section area and $\dot{n}$ is the flow of moles per second per cross-section area.

In the precipitation system, a slurry of water and salt is removed from the spent dilute solution. The water removed can be compensated for by adding some of the spent concentrated solution back to the spent dilute solution. This is illustrated in Figure 11, where the water content in the slurry, $\Phi_{w,2}$, is defined equal to the water content in the solution removed for the concentrated solution, $\Phi_{w,1}$, and added back to the dilute concentration.
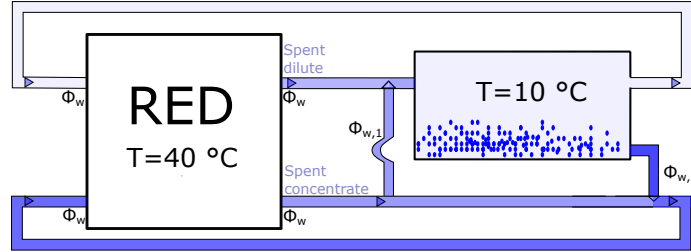
Figure 11. The mass flow in the precipitation system. $\Phi_{w,1}$ is the water flow from the concentrated to the dilute solution, while $\Phi_{w,2}$ is the water flow from dilute to concentrated solution. For no loss of water, $\Phi_{w,1} \equiv \Phi_{w,2}$.

If the inlet concentration is to be kept constant, these two equation must apply, where $\Phi_{w,2}$, is the water flux of the precipitated slurry and $\Phi_{w,1}$ is the water flux added back to the spent dilute solution. The units are per time and cross-section area (flux):

$$\frac{\dot{n}_c^{outlet} - b_c^{outlet}\Phi_{w,1} + b_{slurry}\Phi_{w,2}}{\Phi_w + \Phi_{w,2} - \Phi_{w,1}} = b_c^{inlet}$$

$$\frac{\dot{n}_d^{outlet} + b_c^{outlet}\Phi_{w,1} - b_{slurry}\Phi_{w,2}}{\Phi_w - \Phi_{w,2} + \Phi_{w,1}} = b_d^{inlet} \tag{20}$$

where $\dot{n}$ is the molar flux, b is the concentration and Φ_w is the mass flux of water (see Table 4 and Figure 11). The suffix *outlet* and *inlet* refers to the outlet and inlet solution from the RED stack, while c and d is the concentrated and dilute solution, respectively. The concentration of the slurry is set so that the mass of salt and water content is equal:

$$\frac{\Phi_{salt}}{\Phi_w} = 1 \rightarrow \frac{\dot{n}_{salt}M_{salt}}{\Phi_w} = 1 \rightarrow b_{slurry} = \frac{1}{M_{salt}} \tag{21}$$

Solving either of the equation in Equation (20) will give the mass flux of water in the salt slurry, $\Phi_{w,2}$, and the water flux transferred from the concentrated to the diluted solution, $\Phi_{w,1}$.

In the evaporation system, the water removed from the concentrated outlet solution needs to be added back for the dilute solution. This is illustrated in Figure 12. The water flux is taken to be the same as Fumatechs recommendations for their ED stack, and the outlet concentrations are calculated from Equation (19).
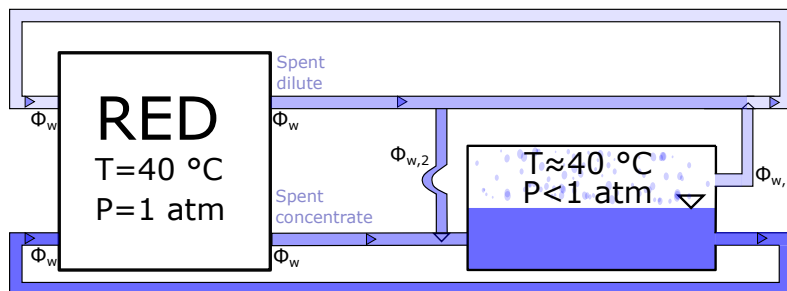
Figure 12. The mass flow in the evaporation system. $\Phi_{w,1}$ is the water flow from concentrated to the dilute solution, while $\Phi_{w,2}$ is the water flow from the dilute to the concentrated solution. For no loss of water, $\Phi_{w,1} \equiv \Phi_{w,2}$.

If the inlet concentration is to be kept constant, these two equations need to be solved, where $\Phi_{w,1}$, is the water evaporated and added to the dilute solution, and $\Phi_{w,2}$ is the water content of the solution added back to the spent concentrated solution. The units are per time and membrane area:

$$\frac{\dot{n}_c^{outlet} + b_d^{outlet}\Phi_{w,2}}{\Phi_w - \Phi_{w,1} + \Phi_{w,2}} = b_c^{inlet}$$

$$\frac{\dot{n}_d^{outlet} - b_c^{outlet}\Phi_{w,2}}{\Phi_w + \Phi_{w,1} - \Phi_{w,2}} = b_d^{inlet} \tag{22}$$

The enthalpy for heating and evaporating water, and the enthalpy to dissolve KNO_3 is given in Table 5.

Table 5. Input enthalpy values used to model power density and hydrogen production from RED.

Name	Symbol	Value
Vaporizing water	$\Delta H_{vap.}$	11.3 Wh mol^{-1} (628 Wh kg^{-1}) [53]
Heating water	$\Delta H_{heating}$	0.0209 Wh (mol K)$^{-1}$ (1.16 Wh (K kg)$^{-1}$)
Disolving KNO_3 in water	$\Delta H_{dissolve}$	9.69 Wh mol^{-1} (538 Wh kg^{-1}) [54]

5. Results and Discussion

The ion conductivity measurements revealed significant differences in ion conductivity for KNO_3 and NaCl. The relevance of these results is demonstrated by implementing them into the described model of the hydrogen production from RED using concentrations relevant for precipitation and evaporation. This section contains results from the measured ion conductivity and the modelled data, and discussion of all the results.

5.1. Ion Conductivity Measurements

The ion conductivity of KNO_3 and NaCl in CEM and AEM are plotted in Figure 13. The conductivity of KNO_3 in CEM at both 23 °C and 40 °C are similar to the conductivity of NaCl. The ion conductivity in AEM is significantly lower for KNO_3 than for NaCl at both 23 °C and 40 °C (Figure 13b,d).

(a)   (b)
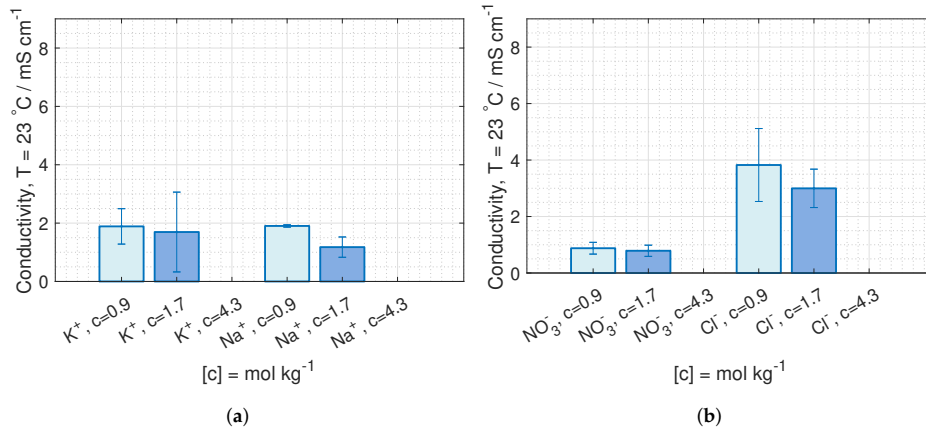
Figure 13. *Cont.*
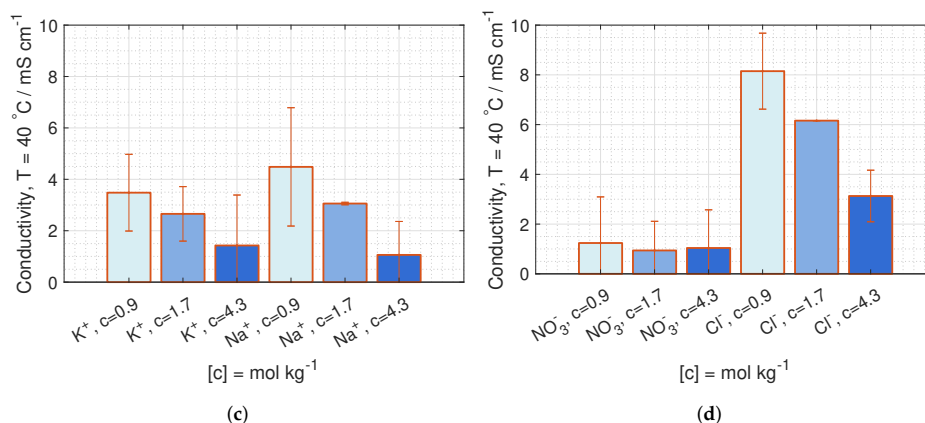
Figure 13. Ion conductivity at 23 °C in (**a**) CEM and (**b**) AEM, and at 40 °C in (**c**) CEM and (**d**) AEM, with 95% confidence interval.

Due to high deviations, a possible change in conductivity with concentrations can only be seen for NaCl, where the conductivity decreases with increased external concentrations. Even though the membrane concentration should increase with the external concentration (see Section 3.3), the water diffuses from the membrane to the external solution, both lowering the total amount of moving charges and decreases the diffusion coefficient.

The difference in conductivity between AEM and CEM could be due to a higher ICE in AEM than in CEM. This is the case for NaCl.

The general indication of an increase in conductivity with temperature can be due to increased swelling, resulting in a higher solution uptake.

5.2. Modeling of Hydrogen Production

As described in the experimental section, the dilute concentration used with the evaporation process is chosen from what gives the highest hydrogen production. The model of the hydrogen production for various concentrations is plotted in Figure 14 where the ideal dilute concentration for the evaporation process is found to be 0.081 and 0.101 mol kg^{-1} at 25 and 40 °C respectively.
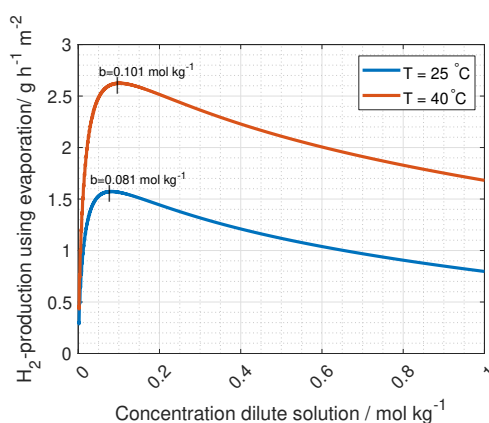
Figure 14. The change in the hydrogen production as a function of the dilute concentration in RED. The concentration of the concentrated inlet is set by the solubility limit at 25 and 40 °C, 3.79 and 6.22 mol kg^{-1}.

The permselectivity of the membranes in KNO_3 is unknown but assumed to be between 0.96 and 0.63 (see Table 4). The driving potential from RED is found from Equation (3), with concentrations given in Table 4 and Figure 14, and activity coefficients given in Equation (4). The unit cell driving potential is plotted in Figure 15. The reason for the higher driving potential with concentrations relevant to evaporation compared to the potential using concentrations relevant for precipitation is only due to the increased concentration difference.
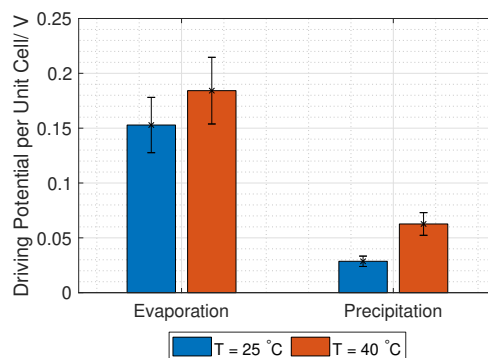
Figure 15. Driving force for RED using concentrations relevant for the separation techniques evaporation and precipitation.

The membrane resistance of AEM and CEM at 23 °C is taken to be the average over the measured concentrations (see Figure 13) due to no significant change in the conductivity. The relevant membrane ion conductivity for the modelling of the hydrogen is given in Table 6.

Table 6. Measured membrane ion conductivity for the relevant mean concentration of KNO_3 for the inlet to RED, 23 °C and 40 °C.

	κ_{AEM}	κ_{CEM}
23 °C	$0.08 \pm 0.01 \, S\,m^{-1}$	$0.18 \pm 0.07 \, S\,m^{-1}$
40 °C	$0.11 \pm 0.09 \, S\,m^{-1}$	$0.20 \pm 0.11 \, S\,m^{-1}$

The total theoretical ohmic resistance of the RED stack, including the measured membrane resistance, is given in Figure 16. The reason for the large difference in dilute solution resistance is the higher concentration in the inlet solutions used for the precipitation system compared to the evaporation system.

(**a**)   (**b**)
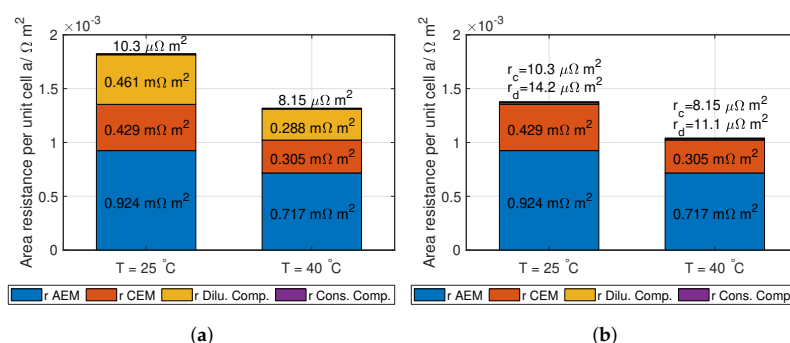
Figure 16. The total ohmic resistance in a RED unit cell at 23 °C and 40 °C using concentrations relevant for (**a**) evaporation and (**b**) precipitation. The calculation of the four contributions can be seen in Equation (14).

Given the open circuit potential in Figure 15, a lumped electrode loss of 0.1 V (see Table 4) and the unit cell ohmic resistance in Figure 16, the number of unit cells can be calculated from Equation (12). The results are given in Table 7. The operation current density is calculated from Equation (11), and given in Table 8.

Table 7. The number of unit cells needed to have a total stack potential of 1.33 V and an operating current density at peak power.

	25 °C	**40 °C**
Precipitation	93 ± 16	43 ± 8
Evaporation	18 ± 3	15 ± 3

Table 8. The operating current density of RED (see Equation (11)).

	25 °C	**40 °C**
Precipitation	10 ± 2 A m^{-2}	30 ± 18 A m^{-2}
Evaporation	42 ± 9 A m^{-2}	70 ± 34 A m^{-2}

The unit cell power density from RED is given in Figure 17. Due to uncertainties, both in the open circuit potential (permselectivity) and the membrane resistance, the propagation of uncertainty leads to correspondingly high uncertainties in the power density.

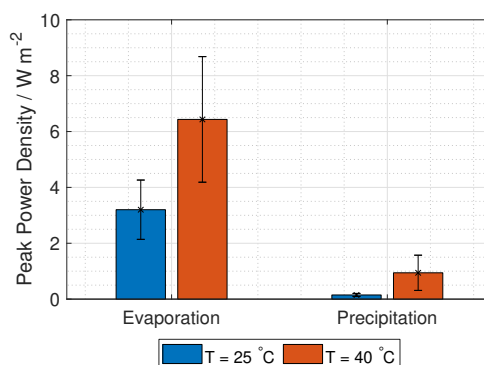**Figure 17.** Power density from one RED unit cell (no tafel or electrode losses) per cross-section area using concentrations relevant for the separation techniques evaporation and precipitation.

The predicted hydrogen production from the RED stack is given in Figure 18, where the production at 40 °C using KNO$_3$ is 2.6 ± 1.3 g h^{-1} m^{-2} (per cross-section area) for the evaporation process, and 1.1 ± 0.7 g h^{-1} m^{-2} (per cross-section area) for the precipitation process.

For comparison, proton exchange membrane water electrolysis (PEMWE) has a normal operation current density of 10 kA m^{-2} [55,56], resulting in a hydrogen production of 376 g h^{-1}m^{-2}. The cross-section area of RED needs to be minimum 160 times higher than the cross-section area in PEMWE to produce the same amount of hydrogen. However, the nature of the RED and PEMWE systems are different, as hydrogen is produced from electric power in PEMWE while the Heat to H$_2$-system intends to use low-grade waste heat to produce hydrogen. The cell stack in the two systems also differs significantly: The bipolar plates, separating every unit cell in PEMWE, contribute to 80% of the weight and almost 50% of the cost in PEMWE [57]. In the RED-stack, there is no need for a unit cell separator. The membrane is also potentially cheaper in RED, where hydrocarbon material is used versus Nafion in PEMWE.
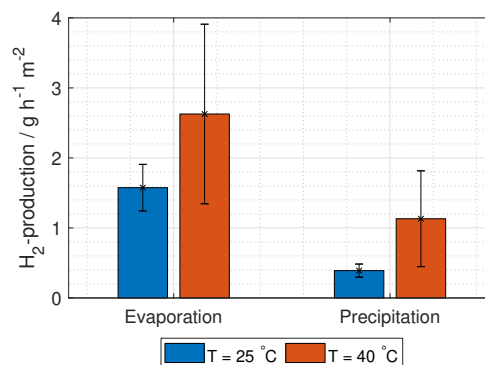
Figure 18. Hydrogen production per hour and unit cell area from RED using concentrations relevant for the separation techniques evaporation and precipitation.

5.3. Energy Consumption and Cost

The energy losses in the RED stack, are the ohmic losses per unit cell and the lumped electrode losses. The calculation of these losses is carried out as described in Section 3.2. In the precipitation separation process, the majority of the energy is needed for heating the solution from 10 to 40 °C and for dissolving the salt. In the evaporation separation process, the major energy consumption is in the evaporation of the water from the concentrated solution. In the calculation of the energy used per volume hydrogen produced, the hydrogen production at 40 °C is used as a reference.

Using the hydrogen production from Figure 18 as input for Equation (19), the outlet concentrations from RED can be calculated, given in Table 9. The difference in concentration from the inlet to the outlet solution from RED gives the amount of salt needed to add or remove from the outlet solutions to regenerate the original inlet concentrations.

Table 9. Inlet and outlet concentrations for the dilute and concentrated solutions.

Precipitation	
Inlet conc. concentration	6.2 mol kg^{-1}
Inlet dilute. concentration	2.1 mol kg^{-1}
Outlet conc. concentration	6.1 mol kg^{-1}
Outlet dilute concentration	2.2 mol kg^{-1}
Evaporation	
Inlet conc. concentration	6.2 mol kg^{-1}
Inlet dilute. concentration	0.1 mol kg^{-1}
Outlet conc. concentration	5.3 mol kg^{-1}
Outlet dilute concentration	1.0 mol kg^{-1}

Solving Equations (20) and (22), gives the mass fluxes as given in Table 10. Using the enthalpies in Table 5 and the fluxes from Table 10, the energy used in the two Heat to H$_2$-systems are given in Table 11.

For the evaporation process, 90% of the energy consumption is allocated to the evaporation of water. The total energy consumption is over ten times higher than the energy consumption per volume hydrogen produced with PEMWE (4.78 kWh m^{-3} [58], operating at 2 V) and alkaline water electrolyser (3 kWh m^{-3} [59]).

For the precipitation process, the majority of the losses are distributed evenly between the reversible work, the ohmic losses and the heating (dissolving of salt and heating of water). The total energy consumption of the RED and precipitation process is comparable to both PEMWE and alkaline water electrolysis.

100

Table 10. Mass fluxes in the two separation systems per cross-section area.

Specific Mass Flux	Mass Flux/kg h^{-1} m^{-2}
Precipitation	
Flux of water, Φ_w	8.36
Flux intlet conc. solution (from RED)	13.6
Flux intlet dilute solution (from RED)	10.1
Flux outlet conc. solution (from RED)	13.5
Flux outlet dilute solution (from RED)	10.3
Flux of salt from dilute to conc. solution	0.295
Flux of water from dilute to conc. solution	0.295
Flux of solution from conc. to dilute solution	0.476
Evaporation	
Flux of water, Φ_w	2.92
Flux inlet conc. solution (from RED)	4.75
Flux inlet dilute solution (from RED)	2.95
Flux outlet conc. solution (from RED)	4.49
Flux outlet dilute solution (from RED)	3.21
Flux of water from conc. to dilute solution (eva.)	2.62
Flux of solution from dilute to conc. solution	2.88

Table 11. Energy needed per volume hydrogen produced from RED using evaporation and precipitation at 40 °C. * Due to the restriction on the ohmic and lumped electrode losses (see Section 3.1), there is no uncertainty.

Process	V V	j A m$^{-2}_{\text{cross}}$	P W m$^{-2}_{\text{cross}}$	W kWh m^{-3}	W kWh kg^{-1}
Evaporation					
Reversible work	1.23	70 ± 34	86 ± 42	2.57	32.7
Electrode comp. loss	0.10 *	70 ± 34	7 ± 3	0.21	2.7
Ohmic loss RED-stack	1.33 *	70 ± 34	93 ± 45	2.78	35.3
Regen. heat (eva.)	24 ± 10	70 ± 34	1600 ± 1000	49 ± 22	600 ± 300
Total	**26 ± 10**	**70 ± 34**	**1800 ± 1000**	**55 ± 22**	**700 ± 300**
Precipitation					
Reversible work	1.23	30 ± 18	86 ± 42	2.57	32.7
Electrode comp. loss	0.10 *	30 ± 18	3.0 ± 1.8	0.21	2.7
Ohmic loss RED-stack	1.33 *	30 ± 18	40 ± 24	2.78	35.4
Regen. heat needed	0.341 ± 0.008	30 ± 18	10 ± 6	0.71 ± 0.02	9.1 ± 0.2
Regen. heat (dissolve)	0.94 ± 0.02	30 ± 18	28 ± 17	1.96 ± 0.04	25.0 ± 0.6
Total	**3.94 ± 0.02**	**30 ± 18**	**167 ± 52**	**8.23 ± 0.05**	**104.8 ± 0.6**

The cost per kg of hydrogen produced can be estimated by including the membrane cost, which is assumed to be the most expensive part of the RED-stack materials [4], and the cost of the salt. This is a simplification, and for a future study other costs should be considered, e.g., the cost of the separation unit. Assuming a membrane price of 170 \$ m^{-2} and a membrane lifetime of 4 years [10] the price for producing 1 kg of hydrogen is 55 \$ and 370 \$ for the evaporation and the precipitation process respectively. To compete with the cost of producing hydrogen using electrolysers, 4.2–14 \$ kg^{-1} [60], the membrane price needs to cost less than 43 \$ m^{-2} and 6.5 \$ m^{-2} for the evaporation and precipitation process respectively. The cost of KNO$_3$ is 78 \$ kg^{-1}, and the amount of salt inside the RED-stack is 1.3 kg m^{-2} and 4.7 kg m^{-2} for the number of unit cells relevant for the evaporation and precipitation system, respectively. Assuming the doubled amount of salt is needed for the entire Heat to H$_2$-system and the system can operate for 100 years (membranes need to be changed more often), the cost of the salt is 0.043 \$ and 0.371 \$ per kg hydrogen produced using the evaporation and precipitation system respectively. In the present Heat to H$_2$-system the price of the salt is negligible compared to the cost of

the membranes. Raka et al. [10] found the contribution from heating to be over 50% of the total cost in a system similar to the one presented here. Obtaining the heat at an energy price of 0.15 $ per kWh [4], the cost of the heating per kg hydrogen produced is 100 $ using the evaporation process and 16 $ using the precipitation process.

6. Conclusions

Two separation techniques for outlet solutions from RED are presented. Due to the necessity of a large change in solubility with temperature, KNO_3 is evaluated as a salt for the solutions used in RED. Ion conductivity is measured at 23 °C and 40 °C for one AEM and one CEM (FAS-50 and FKS-50) at three different concentrations. However, the conductivity of KNO_3 did not change significantly with concentration. The conductivity for AEM was found to be 0.8 ± 0.1 mS cm^{-1} and 1.1 ± 0.9 mS cm^{-1} at 23 °C and 40 °C respectively, while for CEM the conductivity was found to be 1.8 ± 0.7 mS cm^{-1} and 2.5 ± 0.9 mS cm^{-1} at 23 °C and 40 °C respectively. Due to the low conductivity of NO_3^- in AEM other salts should be considered, e.g., $CaCl_2$ and NaOH.

The driving force in RED using concentrations relevant to evaporation is 5 and 3 times higher than for the system relevant for precipitation at 25 °C and 40 °C respectively. However, due to lower dilute concentration in for the evaporation process, the resistance of the dilute compartment is 30 times higher for the concentration relevant for evaporation versus precipitation, increasing the total unit cell resistance by 30%.

Comparing the measured membrane resistance to the total unit cell resistance in RED, the membranes account for 98% of the total resistance using the precipitation process. For the evaporation process, the membrane resistance accounts for 70–80% of the total stack resistance. A decrease in the membrane resistivity with 50% would double the hydrogen production for the precipitation, while it would increase with 70% for the evaporation.

The predicted power density from RED in the two processes takes into account the assumed open circuit potential and the resistance. RED, using concentrations relevant for the evaporation process, can deliver seven times higher unit cell power density per cross-section area then RED using concentrations relevant for precipitation at 40 °C.

The hydrogen production is calculated using the current at maximum power density, and a total RED stack potential of 1.33 V. The production of hydrogen using concentrations relevant for the evaporation process is 4 and 2 times higher than for concentrations relevant for the precipitation process at 25 °C and 40 °C respectively. From a cost perspective the evaporation process is preferable over the precipitation process due to a higher hydrogen production per membrane area, while from an energy demand perspective the precipitation process is the superior separation technique. The energy needed per cubic meter of hydrogen produced is 55 ± 22 kWh for the evaporation process and 8.22 ± 0.05 kWh for the precipitation process. The most common renewable source of hydrogen production today is PEMWE, which stands for 4% of the world's total hydrogen production [61]. The results from the measurements and the modelling in this article present an alternative renewable way to produce hydrogen with an energy consumption comparable to PEMWE, where the input energy is otherwise lost low-grade waste heat.

Author Contributions: K.W.K. conducted the preparation of membranes and most of the conductivity measurements and all simulations. K.W.K. has written the article with contributions from weekly supervision meetings. R.B. conducted many of the conductivity measurements, contributed to discussions of the energy calculation and did copy-editing of the article. F.S. has contributed with guidance in EIS and general measurements at the lab and contributed with scientific feedback and proofreading. O.S.B. and K.E.E. formulate the idea of combining low-grade waste heat with RED to produce hydrogen and had weekly meetings with K.W.K. for discussion, and guidance of the theory and simulations. Both contributed with scientific feedback and otherwise advising manuscript development for editorial advising to the level of proofreading.

Conflicts of Interest: The authors declare no conflict of interest.

References

1. From Waste Heat to a Resource. Available online: https://www.sintef.no/en/projects/from-waste-heat-to-a-resource/ (accessed on 1 July 2019).
2. Enova, S.F. *Annual Report 2009—Results and Activities*; Technical Report; Enova: Trondheim, Norway, 2009.
3. Brueckner, S.; Miró, L.; Cabeza, L.F.; Pehnt, M.; Laevemann, E. Methods to estimate the industrial waste heat potential of regions–A categorization and literature review. *Renew. Sustain. Energy Rev.* **2014**, *38*, 164–171. [CrossRef]
4. Jalili, Z.; Krakhella, K.W.; Einarsrud, K.E.; Burheim, O.S. Energy generation and storage by salinity gradient power: A model-based assessment. *J. Energy Storage* **2019**, *24*, 100755. [CrossRef]
5. Pattle, R. Production of electric power by mixing fresh and salt water in the hydroelectric pile. *Nature* **1954**, *174*, 660. [CrossRef]
6. Wick, G.L. Power from salinity gradients. *Energy* **1978**, *3*, 95–100. [CrossRef]
7. Weinstein, J.; Leitz, F. Electric power from differences in salinity: The dialytic battery. *Science* **1976**, *191*, 557–559. [CrossRef]
8. Lacey, R. Energy by reverse electrodialysis. *Ocean Eng.* **1980**, *7*, 1–47. [CrossRef]
9. Tamburini, A.; Tedesco, M.; Cipollina, A.; Micale, G.; Ciofalo, M.; Papapetrou, M.; Van Baak, W.; Piacentino, A. Reverse electrodialysis heat engine for sustainable power production. *Appl. Energy* **2017**, *206*, 1334–1353. [CrossRef]
10. Raka, Y.D.; Karoliussen, H.; Lien, K.M.; Burheim, O.S. Opportunities and challenges for thermally driven hydrogen production using reverse electrodialysis system. *Int. J. Hydrog. Energy* **2019**. [CrossRef]
11. Luo, X.; Cao, X.; Mo, Y.; Xiao, K.; Zhang, X.; Liang, P.; Huang, X. Power generation by coupling reverse electrodialysis and ammonium bicarbonate: Implication for recovery of waste heat. *Electrochem. Commun.* **2012**, *19*, 25–28. [CrossRef]
12. Zhu, X.; He, W.; Logan, B.E. Influence of solution concentration and salt types on the performance of reverse electrodialysis cells. *J. Membr. Sci.* **2015**, *494*, 154–160. [CrossRef]
13. Long, R.; Li, B.; Liu, Z.; Liu, W. Hybrid membrane distillation-reverse electrodialysis electricity generation system to harvest low-grade thermal energy. *J. Membr. Sci.* **2017**, *525*, 107–115. [CrossRef]
14. Nam, J.Y.; Cusick, R.D.; Kim, Y.; Logan, B.E. Hydrogen generation in microbial reverse-electrodialysis electrolysis cells using a heat-regenerated salt solution. *Environ. Sci. Technol.* **2012**, *46*, 5240–5246. [CrossRef]
15. Luo, X.; Nam, J.Y.; Zhang, F.; Zhang, X.; Liang, P.; Huang, X.; Logan, B.E. Optimization of membrane stack configuration for efficient hydrogen production in microbial reverse-electrodialysis electrolysis cells coupled with thermolytic solutions. *Bioresour. Technol.* **2013**, *140*, 399–405. [CrossRef]
16. Hatzell, M.C.; Ivanov, I.; Cusick, R.D.; Zhu, X.; Logan, B.E. Comparison of hydrogen production and electrical power generation for energy capture in closed-loop ammonium bicarbonate reverse electrodialysis systems. *Phys. Chem. Chem. Phys.* **2014**, *16*, 1632–1638. [CrossRef]
17. Skilbred, E.S.; Krakhella, K.W.; Haga, I.J.M.; Pharoah, J.G.; Hillestad, M.; del Alamo Serrano, G.; Burheim, O.S. Heat to H2: Using Waste Heat to Set Up Concentration Differences for Reverse Electrodialysis Hydrogen Production. *ECS Trans.* **2018**, *85*, 147–161. [CrossRef]
18. FuelCellStore. *Fumasep FAS-50*; FuelCellStore: College Station, TX, USA, 2019.
19. FuelCellStore. *Fumasep FKS-50*; FuelCellStore: College Station, TX, USA, 2019.
20. Rumble, J.R. Aqueous solubility of inorganic compounds at various temperatures. In *Handbook of Chemistry and Physics*, 99th ed.; CRC: Boca Raton, FL, USA, 2018.
21. Inorganic Salts. Available online: https://www.sigmaaldrich.com/chemistry/chemistry-products.html?TablePage=16281684 (accessed on 22 August 2019).
22. Tufa, R.A.; Rugiero, E.; Chanda, D.; Hnàt, J.; van Baak, W.; Veerman, J.; Fontananova, E.; Di Profio, G.; Drioli, E.; Bouzek, K.; et al. Salinity gradient power-reverse electrodialysis and alkaline polymer electrolyte water electrolysis for hydrogen production. *J. Membr. Sci.* **2016**, *514*, 155–164. [CrossRef]

23. Kim, Y.; Logan, B.E. Hydrogen production from inexhaustible supplies of fresh and salt water using microbial reverse-electrodialysis electrolysis cells. *Proc. Natl. Acad. Sci. USA* **2011**, *108*, 16176–16181. [CrossRef]

24. Burheim, O.S. *Engineering Energy Storage*; Academic Press: Cambridge, MA, USA, 2017.

25. Stokes, R.H.; Robinson, R.A. Ionic hydration and activity in electrolyte solutions. *J. Am. Chem. Soc.* **1948**, *70*, 1870–1878. [CrossRef]

26. Glueckauf, E. The influence of ionic hydration on activity coefficients in concentrated electrolyte solutions. *Trans. Faraday Soc.* **1955**, *51*, 1235–1244. [CrossRef]

27. Dash, D.; Kumar, S.; Mallika, C.; Mudali, U.K. New data on activity coefficients of potassium, nitrate, and chloride ions in aqueous solutions of KNO$_3$ and KCl by ion selective electrodes. *ISRN Chem. Eng.* **2012**, *2012*. [CrossRef]

28. Der Mar Marcos-Arroyo, M.; Khoshkbarchi, M.K.; Vera, J.H. Activity coefficients of sodium, potassium, and nitrate ions in aqueous solutions of NaNO$_3$, KNO$_3$, and NaNO$_3$+KNO$_3$ at 25 °C. *J. Solut. Chem.* **1996**, *25*, 983–1000. [CrossRef]

29. Pitzer, K.S.; Pabalan, R.T. Thermodynamics of NaCl in steam. *Geochim. Cosmochim. Acta* **1986**, *50*, 1445–1454. [CrossRef]

30. Afanasiev, V.N.; Ustinov, A.N.; Vashurina, I.Y. State of Hydration Shells of Sodium Chloride in Aqueous Solutions in a Wide Concentration Range at 273.15–373.15 K. *J. Phys. Chem. B* **2008**, *113*, 212–223. [CrossRef]

31. Onori, G. Ionic hydration in sodium chloride solutions. *J. Chem. Phys.* **1988**, *89*, 510–516. [CrossRef]

32. Lu, G.W.; Li, C.X.; Wang, W.C.; Wang, Z.H. Structure of KNO$_3$ electrolyte solutions: A Monte Carlo study. *Fluid Phase Equilibria* **2004**, *225*, 1–11. [CrossRef]

33. Ribeiro, A.C.; Lobo, V.M.; Burrows, H.D.; Valente, A.J.; Sobral, A.J.; Amado, A.M.; Santos, C.I.; Esteso, M.A. Mean distance of closest approach of potassium, cesium and rubidium ions in aqueous solutions: Experimental and theoretical calculations. *J. Mol. Liq.* **2009**, *146*, 69–73. [CrossRef]

34. Malmberg, C.G.; Maryott, A.A. Dielectric constant of water from 0 °C to 100 °C. *J. Res. Natl. Bur. Stand.* **1956**, *56*, 1–8. [CrossRef]

35. Sangster, J.; Teng, T.; Lenzi, F. A general method of calculating the water activity of supersaturated aqueous solutions from ternary data. *Can. J. Chem.* **1973**, *51*, 2626–2631. [CrossRef]

36. Zlotorowicz, A.; Strand, R.V.; Burheim, O.S.; Wilhelmsen, Ø.; Kjelstrup, S. The permselectivity and water transference number of ion exchange membranes in reverse electrodialysis. *J. Membr. Sci.* **2017**, *523*, 402–408. [CrossRef]

37. Krakhella, K.W.; Seland, F.; Einarsrud, K.E.; Burheim, O.S. Electrodialytic Energy Storage System: IEM Permselectivity and Stack Measurements. Unpublished work.

38. Ji, Y.; Geise, G.M. The Role of Experimental Factors in Membrane Permselectivity Measurements. *Ind. Eng. Chem. Res.* **2017**, *56*, 7559–7566. [CrossRef]

39. Długołęcki, P.; Gambier, A.; Nijmeijer, K.; Wessling, M. Practical potential of reverse electrodialysis as process for sustainable energy generation. *Environ. Sci. Technol.* **2009**, *43*, 6888–6894. [CrossRef]

40. Van Egmond, W.; Starke, U.; Saakes, M.; Buisman, C.; Hamelers, H. Energy efficiency of a concentration gradient flow battery at elevated temperatures. *J. Power Sources* **2017**, *340*, 71–79. [CrossRef]

41. Post, J.W.; Hamelers, H.V.M.; Buisman, C.J.N. Energy recovery from controlled mixing salt and fresh water with a reverse electrodialysis system. *Environ. Sci. Technol.* **2008**, *42*, 5785–5790. [CrossRef]

42. Isono, T. Density, viscosity, and electrolytic conductivity of concentrated aqueous electrolyte solutions at several temperatures. Alkaline-earth chlorides, lanthanum chloride, sodium chloride, sodium nitrate, sodium bromide, potassium nitrate, potassium bromide, and cadmium nitrate. *J. Chem. Eng. Data* **1984**, *29*, 45–52.

43. Hamann, C.; Hamnett, A.; Vielstich, W. *Electrochemistry*; Wiley-VCH: Weinheim, Germany, 2007.

44. Vermaas, D.A.; Guler, E.; Saakes, M.; Nijmeijer, K. Theoretical power density from salinity gradients using reverse electrodialysis. *Energy Procedia* **2012**, *20*, 170–184. [CrossRef]

45. Güler, E.; Elizen, R.; Vermaas, D.A.; Saakes, M.; Nijmeijer, K. Performance-determining membrane properties in reverse electrodialysis. *J. Membr. Sci.* **2013**, *446*, 266–276. [CrossRef]

46. Kamcev, J.; Paul, D.R.; Manning, G.S.; Freeman, B.D. Ion diffusion coefficients in ion exchange membranes: Significance of counterion condensation. *Macromolecules* **2018**, *51*, 5519–5529. [CrossRef]

47. Kamcev, J.; Doherty, C.M.; Lopez, K.P.; Hill, A.J.; Paul, D.R.; Freeman, B.D. Effect of fixed charge group concentration on salt permeability and diffusion coefficients in ion exchange membranes. *J. Membr. Sci.* **2018**, *566*, 307–316. [CrossRef]

48. Beers, K.M.; Hallinan, D.T., Jr.; Wang, X.; Pople, J.A.; Balsara, N.P. Counterion condensation in Nafion. *Macromolecules* **2011**, *44*, 8866–8870. [CrossRef]

49. Tansel, B.; Sager, J.; Rector, T.; Garland, J.; Strayer, R.F.; Levine, L.; Roberts, M.; Hummerick, M.; Bauer, J. Significance of hydrated radius and hydration shells on ionic permeability during nanofiltration in dead end and cross flow modes. *Sep. Purif. Technol.* **2006**, *51*, 40–47. [CrossRef]

50. Soboleva, T.; Xie, Z.; Shi, Z.; Tsang, E.; Navessin, T.; Holdcroft, S. Investigation of the through-plane impedance technique for evaluation of anisotropy of proton conducting polymer membranes. *J. Electroanal. Chem.* **2008**, *622*, 145–152. [CrossRef]

51. Barsoukov, E.; Macdonald, J.R. *Impedance Spectroscopy: Theory, Experiment, and Applications*; John Wiley & Sons: Hoboken, NJ, USA, 2005.

52. Müller, F.; Ferreira, C.A.; Azambuja, D.S.; Alemán, C.; Armelin, E. Measuring the proton conductivity of ion-exchange membranes using electrochemical impedance spectroscopy and through-plane cell. *J. Phys. Chem. B* **2014**, *118*, 1102–1112. [CrossRef]

53. Datt, P. Latent heat of vaporization/condensation. In *Encyclopedia of Snow, Ice and Glaciers*; Springer: Berlin/Heidelberg, Germany, 2011; p. 703.

54. Parker, V. *Thermal Properties of Uni-Univalent Electrolytes*; National Bureau of Standards: Washington, DC, USA; 1965, Volume 2, p. 66.

55. Carmo, M.; Fritz, D.L.; Mergel, J.; Stolten, D. A comprehensive review on PEM water electrolysis. *Int. J. Hydrog. Energy* **2013**, *38*, 4901–4934. [CrossRef]

56. Barbir, F. PEM electrolysis for production of hydrogen from renewable energy sources. *Sol. Energy* **2005**, *78*, 661–669. [CrossRef]

57. Tsuchiya, H.; Kobayashi, O. Mass production cost of PEM fuel cell by learning curve. *Int. J. Hydrog. Energy* **2004**, *29*, 985–990. [CrossRef]

58. Rashid, M.M.; Al Mesfer, M.K.; Naseem, H.; Danish, M. Hydrogen production by water electrolysis: A review of alkaline water electrolysis, PEM water electrolysis and high temperature water electrolysis. *Int. J. Eng. Adv. Technol.* **2015**, *4*, 2249–8958.

59. Zeng, K.; Zhang, D. Recent progress in alkaline water electrolysis for hydrogen production and applications. *Prog. Energy Combust. Sci.* **2010**, *36*, 307–326. [CrossRef]

60. Proost, J. State-of-the art CAPEX data for water electrolysers, and their impact on renewable hydrogen price settings. *Int. J. Hydrog. Energy* **2019**, *44*, 4406–4413. [CrossRef]

61. National Academy of Sciences. Carbon Capture and Storage—The rationale of carbon capture and storage from hydrogen production. In *The Hydrogen Economy: Opportunities, Costs, Barriers, and R&D Needs*; The National Academies Press: Washington, DC, USA, 2019.

PAPER III

An Electrodialytic Energy Storage System: IEM Permselectivity, Stack Measurements and LCA

Kjersti Wergeland Krakhella[a,b], Odne Stokke Burheim[b], Marjorie Alejandra Morales Arancibia[c], Robert Bock[b], Kristian Etienne Einarsrud[a,*]

[a]*Department of Materials Science and Engineering, Norwegian University of Science and Technology (NTNU), NO-7491 Trondheim, Norway*
[b]*Department of Energy and Process Engineering, Norwegian University of Science and Technology (NTNU), NO-7491 Trondheim, Norway*
[c]*Inria, Domaine de Voluceau, Rocquencourt - BP 105, 78153 Le Chesnay Cede, France*

Abstract

Reverse electrodialysis and electrodialysis can be combined into an energy storage system, where surplus energy is stored in a salinity gradient between two solutions in a closed system. The system is charged by applying an external power source to force ions through alternating ion exchange membranes from a dilute solution to a concentrated solution, and is discharged by letting ions migrate through the same membranes from the concentrated solution to the dilute solutions loading off electric energy at the electrodes. Most literature reports on experiments on natural occurring NaCl concentration (seawater and river water), while a closed system can have a higher salt concentration (NaCl up to 6 M). A closed system also benefits from the ability to mitigate membrane module fouling, and the temperature is easier to control. In this work, the permselectivity of two membranes, FAS-50 and FKS-50 from Fumatech, is tested at concentration ratios 5.000 M/0.05000 M, 4.500 M/0.5500 M, 3.000 M/2.050 M and 2.800 M/2.525 M and found to be ranging from 0.7 to 0.5 for FAS-50 and from 0.8 to 0.7 for FKS-50. The maximum open-circuit voltage from one unit cell was measured to be 115 ± 9 mV and 118 ± 8 mV at 25 °C and 40 °C respectively. The power density was found to be 1.5 ± 0.2 W m_{uc}^{-2} at 25 °C and 2.0 ± 0.3 W m_{uc}^{-2} at 40 °C. A life-cycle analysis of the electrodialytic energy storage system, with a total energy storage capacities of 1 GWh per day, 2 hours discharging time and 20 years of operation, give a global warming factor of 62-75 kg CO_2/MWh and a cumulative energy demand of 0.22-0.26 MWh/MWh for the production phase of the EESS.

Keywords: Electrodialytic energy storage system (EESS); Reverse electrodialysis (RED); Permselectivity; Life-cycle analysis (LCA)

*Corresponding author.

Email addresses: `kjersti.s.krakhella@ntnu.no` (Kjersti Wergeland Krakhella), `odne.s.burheim@ntnu.no` (Odne Stokke Burheim), `marjorie-alejandra.morales@inria.fr` (Marjorie Alejandra Morales Arancibia), `robert.bock@ntnu.no` (Robert Bock), `kristian.e.einarsrud@ntnu.no` (Kristian Etienne Einarsrud)

1. Introduction

The prognosis for 2050 of the world's electricity production done by DNV-GL [1] shows that over 70 % of the production stems from renewable sources like wind and solar power. These energy sources are intermittent and often not available when and where we need energy, making a renewable-based economy dependent on energy storage.

Example of ways to store energy is in hydrogen, lithium-ion batteries, capacitors and phase change materials where each storage system has its niche; e.g. cheap, long-lived, high power and high efficiency. A potential storage system which is cheap, easy to scale and chemically flexible is storage in salinity gradient power. The available energy when one cubic meter of river water enters the sea is 2.3 MJ [2, 3] corresponding to a water column of over 200 m [4]. Using brine and river water instead gives us 15 MJ of available energy, which is equivalent to the volumetric energy density of hydrogen at 3 bar.

An energy storage system based on salinity gradients combines a desalination technology with a mixing technology. The system is charged with external power increasing the concentration difference between two solutions, and energy is stored in the form of a chemical potential difference. The system is discharged by mixing the two solutions, converting the chemical potential to electricity, and decreasing the concentration difference. An illustration of a general energy storage system with solutions of different concentrations is given in Fig. 1.
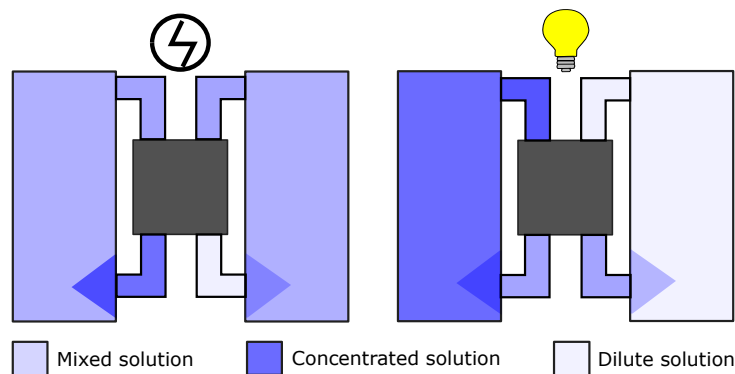
Figure 1: Illustration of an energy storage system; charging (left) by increasing the concentration difference and discharging (right) by mixing the same solutions. The illustration is modified from Jalili et al. [5].

Examples of combinations of technologies which together make up a salinity gradient energy storage system (SGESS) are reversed electrodialysis (RED) and electrodialysis (ED), pressure retarded osmosis (PRO) and reversed osmosis (RO), and capacitive Donnan potential (CDP) and membrane capacitive deionisation (MCDI). A model comparing these SGESSs is carried out by Jalili et al. [5], where RED/ED and PRO/RO was preferable over CDP/MCDI, and at higher temperatures, RED/ED had the highest power density and efficiency. Due to these findings, this article focuses on the electrodialytic energy storage system (EESS) based on RED and ED.

2

An EESS was first suggested by Kingsbury et al. in 2015 [6], with a round-trip efficiency of up to 34 %. Egmond et al. [7] increased the solution temperature to 40 °C and found that the ohmic resistance decreased with increasing temperature, but the water transport increased. Both studies included experiments at constant current. In our study, the concentration of the solutions will be held constant while controlling the potential and measuring the current. The gained polarisation curve gives information regarding kinetics in RED/ED and an energy storage efficiency based on realistic operating current densities. By holding both the inlet concentrations constant while measuring polarisation curves, we can get a better understanding of the limiting kinetics. The polarisation curve will also give the ideal discharging current for maximum power density, and using a realistic current restriction (e.g. the duck curve constraint explained in Jalili et al. [5]), the charging current can be calculated, together with the total efficiency of the EESS.

The power output from an EESS is highly dependent on the concentration difference between the two solutions [6, 7], where higher difference results in higher power density. However, the membranes available for an EESS are mostly used for naturally occurring concentrations and salts (seawater and river water) [8], while for a closed system, higher concentrations are relevant.

This paper will compare the performance of EESS at two temperatures, where the power density and efficiency are chosen as parameters describing the performance. The permselectivity is measured for two relevant membranes at higher salt concentrations. Both stack measurements and permselectivity are compared with theoretically expected values. The results also include a brief life-cycle analysis (LCA) of the EESS.

3

2. Theory

A schematic of the EESS while discharging is shown in Fig. 2. In the discharging process, the chloride ions travel from the concentrated solution to the dilute solution through the anion exchange membrane (AEM), while the sodium ions travel from the concentrated solution to the dilute through the cation exchange membrane (CEM). At each electrode, a redox or rinse solution is circulated. For the experiments carried out in this project, iron(II/III)chloride is used as a redox solution.
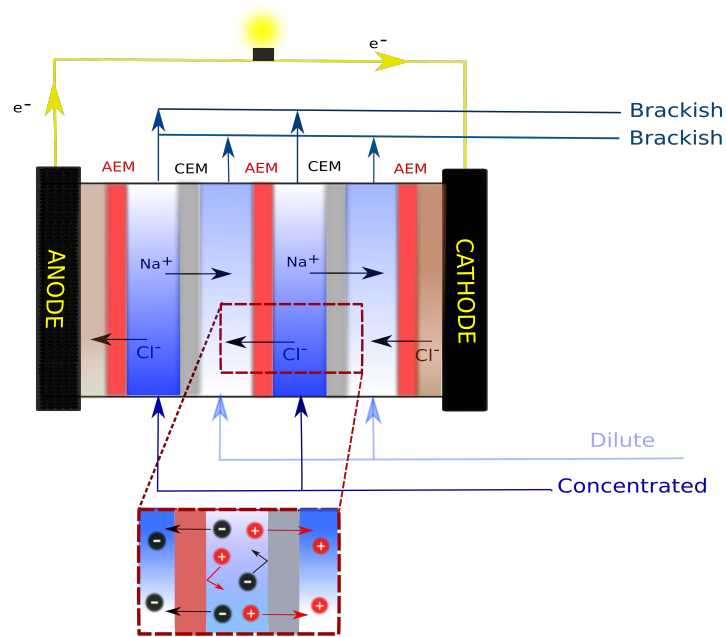

Figure 2: The figure shows the discharging process of an EESS. The sodium and chloride ions travel from the concentrated solutions to the dilute solutions, through AEMs and CEMs. At both electrodes iron(II/III)chloride is circulated absorbing chloride ions at the anode and giving off chloride ions at the cathode.

During discharge, the chloride ions enter the redox solution at the anode, while at the cathode chloride ions leave the redox solution. The reactions at each electrode are:

$$\text{Anode: } Fe^{2+} \rightarrow Fe^{3+} + e^-$$
$$\text{Cathode: } Fe^{3+} + e^- \rightarrow Fe^{2+}$$
(1)
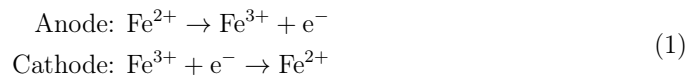
The electrons conduct from the anode to the cathode while discharging. When the EESS is charging, electrons are forced from the anode to the cathode using an external power source, also reversing the reactions given in Eq. (1).

The open-circuit voltage (OCV) over a unit cell is derived from the Nernst equation:

4

$$E_{\text{OCV}} = 2\overline{\alpha}\frac{RT}{zF}\ln\left(\frac{c_c\gamma_c}{c_d\gamma_d}\right), \tag{2}$$

where R is the ideal gas constant, T is the temperature in Kelvin, F is Faraday constant, z is the number of electrons transferred and $\overline{\alpha}$ is the mean permselectivity of the CEM and AEM. The permselectivity of the membranes expresses the capability to discriminate between two ions with a different charge. It is highly dependent on solution concentration and transport number of salt and water, but less dependent on solution temperature [8]. c_c and c_d, and γ_c and γ_d are the molarity and activity coefficients of the concentrated and dilute solution respectively.

To the author's knowledge, the permselectivity of the membranes used in this study is only measured at 25 °C and 0.5 M NaCl, where Fumatech reports a permselectivity of 0.97-0.99 and 0.92-0.96 for FKS-50 and FAS-50 respectively [9, 10]. The theoretical permselectivity for an IEM is given in Eq. (3) [8]:

$$\begin{aligned} \alpha &= t_s - t_w \times M_W \times \frac{b_1 - b_2}{\ln((b_1 \times \gamma_1)/(b_2 \times \gamma_2))} \quad (b_1 \neq b_2) \\ \alpha &= t_s - t_w \times M_W \times b_1 \quad\quad\quad\quad\quad\quad (b_1 = b_2), \end{aligned} \tag{3}$$

where t_s and t_w are the transport number of salt and water respectively, M_w is the molar weight of water (0.018 kg mol^{-1}), and b_1 and b_2 are the molalities of the solutions on each side of the membrane. Given the constant transport number of salt and water, the permselectivity would increase with concentration difference.

The transport number of salt is defined as the amount of the current carried by the counterion. If more co-ions are transported with the salt gradient, the transport numbers decrease, and the amount of co-ions in the membrane is dependent on the salt concentration in the bulk and the concentration of the fixed charges in the membrane [11]. FAS-50 and FKS-50 has an average of 0.13 mol and 0.10 mol fixed charges per square meter membrane respectively [9, 10].

Zlotorowicz et al. [8] measured the transport number of water and salt in the membranes FAD and FKD from Fumatech at a concentration up to 0.6 M, where the transport number of salt was 0.93 and 0.998 for CEM and AEM, respectively. Długołęcki et al. modelled the transport number of salt in the same membranes as Zlotorowicz et al., where linear regression gives the following salt transport numbers for FKS and FAD from Fumatech [12]:

$$\begin{aligned} t_s^{\text{AEM}} &= -0.09 \times c + 1 \\ t_s^{\text{CEM}} &= -0.03 \times c + 1 \end{aligned} \tag{4}$$

where c is the molarity of the solution. In this study, c is the mean value of the solutions on each side of the membrane.

The water transport number is dependent on osmotic and electroosmotic effects [13]. The water transported by osmosis diffuses from the dilute to the concentrated solution, reducing the permselectivity, while water transported due to electroosmosis is carried as a hydration shell around the counterions (hydration number), moving from the concentrated

5

to the dilute solution, increasing the permselectivity. The osmotic effect will be higher with higher concentration difference, while the number of water molecules per ion is lowered with concentration [14]. Zlotorowicz et al. [8] measured the transport number of water to be 8 and 6 for CEM and AEM respectively. However; due to the large difference between the concentrations in the present work and concentrations used by Zlotorowicz et al., the water transport number in AEM and CEM for the model is varied between 0 and 10 [15]. The permselectivity given salt transport number equal to Eq. (4), and average water transport number: $t_w = 5$, and activity coefficients equal to unity, is plotted in Fig. 3.
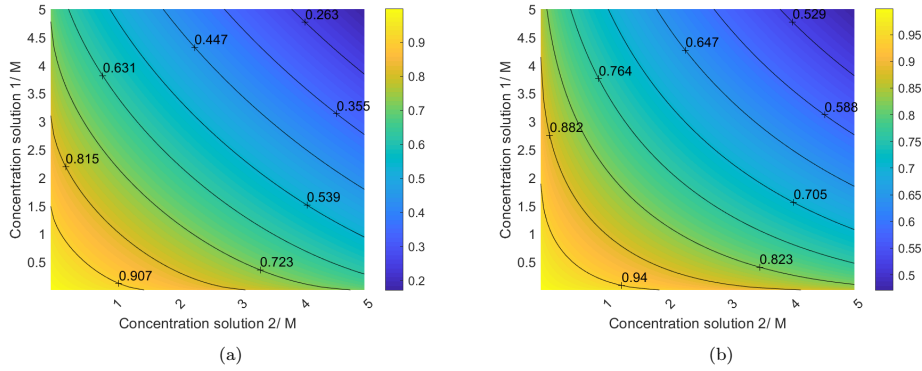

Figure 3: Permselectivity for AEM (a) and CEM (b). $t_w = 5$ and t_s follow Eq. (4), with the membrane concentration equal to the average concentration between the solutions, and activity coefficient assumed unity.

Activity coefficients for solutions with higher concentrations than 1 M lie beyond Debye-Hückel, Davies and Truesdell-Jones modell limitations. Stokes and Robinsons equation is therefore used [16, 17]:

$$\gamma_{\pm} = exp\left(\frac{A \times z_{\pm}^2 \times \sqrt{I}}{1 + B \times a\sqrt{I}} - \frac{h}{\nu}\ln(a_w) - \ln(|1 + (M_w(\nu - h) \times b|)\right) \quad (5)$$

where I is the ionic strength, here with 1 mol kg^{-1} as reference, $z_{\pm}$ is the mean of the valence of the cation and anion (1 for NaCl), ν is the number of ions per molecule (2 for NaCl), h is the hydration number of NaCl and a is the distance of the closest approach[1]. h and a are found to be 5.2 and 0.42 nm respectively from curve fitting to [18]. The hydration number and the distance of the closest approach is found to depend on temperature and concentration [14]; however this is not taken into consideration for the modelling in this article. A and B are temperature dependent and given in Eq. (6) ($A = 1.18$ (kg/mol)$^{1/2}$ and $B = 3.29 \times 10^9$ (kg/mol)$^{1/2}$ m^{-1} at 25 °C [19]):

---

[1]the minimum distance between the center core of two particles before it is reflected back

6

$$A = (2\pi N_A \rho_w)^{1/2} \left(\frac{e^2}{4\pi\epsilon_0\epsilon_{r,w}k_BT} \right)^{3/2}$$

$$B = e \left(\frac{2N_A\rho_w}{\epsilon_0\epsilon_{r,w}k_BT} \right)^{1/2},$$

(6)

where N_A is Avogadro number, ρ_A is the density of the solvent (for simplicity set to 1000 kg m^{-3}), e is the elementary charge, ϵ_0 is permittivity of vacuum and k_B is Boltzmann constant. $\epsilon_{r,w}$ is the dielectric constant of the solvent [20] (here water) and given in Eq. (7) (rewritten to use Kelvin instead of Celsius):

$$\epsilon_{r,w} = 87.74 - 0.4008 \times (T-273.2) + 9.398 \times 10^{-4} \times (T-273.2)^2 - 1.410 \times 10^{-6} \times (T-273.2)^3 \quad (7)$$

In Eq. (5), a_w is the water activity as a function of the salt concentration given in Eq. (8) [21]:

$$a_w = \gamma_w \times x_w$$
$$\gamma_w = \alpha_{a_w,NaCl}x_s^2 + \beta_{a_w,NaCl}x_s^3$$
$$x_s = \frac{b}{b + 1/M_{\rm w}}$$
$$x_w = \frac{1/M_{\rm w}}{b + 1/M_{\rm w}}$$

(8)

where γ_w is the activity constant of water (equal to 1 with no salt present), x_w is the mole fraction of water, $\alpha_{a_w,NaCl}$ and $\beta_{a_w,NaCl}$ are constants found from Miyawaki to be 1.825 and -20.78 for NaCl respectively [21]. x_s is the mole fraction of salt.

The modelled activity coefficient from Stokes-Robinson equation (Eq. (5)) is plotted in Fig. 4 together with the data from Pytkowicz [18]. One reason for the deviation between Stokes-Robinson equation and the measured activity coefficient of NaCl is the assumption of no temperature or concentration dependency in the modelled hydration number. Afanasiev et al. [22] suggest an exponential dependence on concentration and negligible dependency of temperature, while Onori [23] gives a linear dependence on concentration and state that the hydration number is dependent on temperature. For simplicity, neither the dependence on temperature nor concentration, of the hydration number nor the distance of the closest approach is taken into consideration for this work.

Increasing the solution activity difference between the two solutions in the EESS will increase the OCV and thereby the power density. From the activity coefficient perspective, it is beneficial to have one concentration close to 1 M and the other concentration at 0 M or 5 M. The activity also increases with increasing temperature, but the impact is less prominent than for concentration.

The total unit cell voltage is given in Eq. (9) for charging and Eq. (10) for discharging.
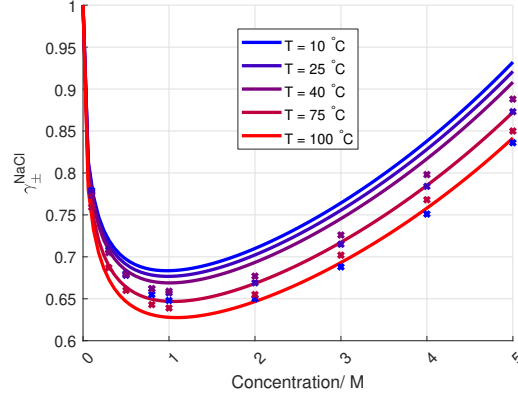
7

Figure 4: Modelled activity coefficient for NaCl for different concentrations and temperatures, together with data from Pytkowicz [18]. The model is following Stokes-Robinson equation, where a and h is found from curve fitting to data from [18].

$$E^{\text{charging}} = E_{\text{OCV}} + r_\Omega \cdot i^{\text{charging}} \tag{9}$$

$$E^{\text{discharging}} = E_{\text{OCV}} - r_\Omega \cdot i^{\text{discharging}} \tag{10}$$

where i is the current density per cross-section area and r_Ω is the ohmic resistance (Ωm^2) of a unit cell. The latter is the sum of the resistance of one AEM, one CEM, one compartment of dilute and one compartment of concentrated solution. It is important to emphasise that the electrode resistance, $r_{\text{electrode}}$ can be assumed negligible for a stack containing a large number of cell pairs [24], but on the laboratory scale, it needs to be considered. The ohmic resistance in one unit cell is given in Eq. (11) [25]:

$$r_\Omega = \frac{\delta_{\text{m}}}{\sigma_{\text{AEM}}(1 - \beta)} + \frac{\delta_{\text{m}}}{\sigma_{\text{AEM}}(1 - \beta)} + \frac{\delta_{\text{s}}\rho_{\text{d}}}{\epsilon^2} + \frac{\delta_{\text{s}}\rho_{\text{c}}}{\epsilon^2}, \tag{11}$$

where δ_{m} is the membrane thickness, σ_{AEM} and σ_{CEM} are the ionic conductivity in the AEM and CEM (S m^{-1}) respectively and β (dimensionless) is the spacer shadow effect [26] or the part of the membrane that is covered by a spacer. δ_{s} is the thickness of the spacer and ϵ (dimensionless) is the porosity or the factor to correct for the occupied volume by the spacer (equal to 1 with no spacer). The porosity is defined as one minus the volumetric ratio[2] and squared to represent the tortuous behavior of the ion transport in the spacer-filled channel. ρ_d and ρ_{c} are the resistivity of the dilute and concentrated solution respectively (Ω m). Theoretical values are deduced from conductivity measurements of sodium chloride in water at 25 °C from [27] (wt% to mol L^{-1}, and µS cm^{-1} to S m^{-1}), and fit to the equation given in [28, p.22]:

---

[2]the ratio of the apparent gravity and the specific gravity of the spacer (see [25])

8

$$\sigma_{sol,25} = k_1 \times c - k_2 \times c^{3/2} \tag{12}$$
$$k_1 = 11.8 \pm 0.2 \text{ S m}^{-1}$$
$$k_2 = 2.7 \pm 0.1 \text{ S/(mol m}^{-1})^{1/2}$$

where $\sigma_{sol,25}$ is the solution conductivity at 25 °C (S m^{-1}). The theoretical temperature effect on the resistance is from a report of Schlumberger [29]:

$$\rho_{sol} = \frac{1}{\sigma_{sol,25}} \frac{46.5 \text{ K}}{T - 251.5 \text{ K}} \tag{13}$$

The equation is rewritten to use Kelvin instead of Celsius.

The power density per unit cell (uc) area, P (W m$^{-2}_{\text{uc}}$), is the electrode voltage, E (V) Eq. (10), multiplied by the current density, i (A m^{-2}):

$$P_{\text{uc}}^{\text{charging}} = E_{\text{OCV}} i^{\text{charging}} + r_\Omega \cdot (i^{\text{charging}})^2 \tag{14}$$
$$P_{\text{uc}}^{\text{discharging}} = E_{\text{OCV}} i^{\text{discharging}} - r_\Omega \cdot (i^{\text{discharging}})^2 \tag{15}$$

Following the duck curve constraint (see Jalili et al. [5]), the current density while charging is approximately half the current density while discharging. The discharging current density at the peak power density is:

$$i^{\text{discharging}} = \frac{E_{\text{OCV}}}{2r_\Omega}, \tag{16}$$

Inserting the given current density into Eq. (15) and half the current density into Eq. (14), the power density used while charging is given in Eq. (17) and the power density gained during discharge is given in Eq. (18):

$$P^{\text{charging}} = \frac{5E_{OCV}^2}{16r_\Omega}, \tag{17}$$

$$P_{\text{max}}^{\text{discharging}} = \frac{E_{OCV}^2}{4r_\Omega}, \tag{18}$$

The total reversible power density is given as:

$$P_{\text{reversible}} = E_{\text{OCV}} i \tag{19}$$

In this work the reversible potential is calculated from the measured OCV, and the measured peak power current density while discharging and half this current for the reversible power for charging.

The power loss in pumping is given in Eq. (20) [30]:

9

$$P_{\text{pump}} = \frac{12\mu v^2 \delta_{\text{s}} \epsilon}{0.25 D_h^2} \cdot 1.5 \tag{20}$$

where v is the flow velocity (m s^{-1}) and the factor 1.5 is an approximation of the compensation for the electric efficiency of the pump [31]. D_{h} is the hydraulic diameter [30, 32]:

$$D_{\text{h}} = \frac{4\epsilon}{2/\delta_{\text{s}} + (1 - \epsilon)(\frac{S_{\text{sp}}}{V_{\text{sp}}})}, \tag{21}$$

where $\frac{S_{\text{sp}}}{V_{\text{sp}}}$ is the ratio between the surface area and volume of the spacer filaments.

The viscosity is given in Eq. (22) [33]:

$$\mu = 1.234 \times 10^{-6} e^{0.00212 \cdot c \cdot M + 1965/T}, \tag{22}$$

The efficiency of the discharging is the net power density produced divided by the reversible power density, given in Eq. (23). The efficiency of the charging of the EESS is the reversible power density divided by the power density used by ED and the power used for pumping, given in Eq. (24).

$$\eta_{\text{discharging}} = \frac{P_{\text{max}}^{\text{discharging}} - P_{\text{pump}}}{P_{\text{reversible}}} \tag{23}$$

$$\eta_{\text{charging}} = \frac{P_{\text{reversible}}}{P^{\text{charging}} + P_{\text{pump}}} \tag{24}$$

Given no pumping losses and purely ohmic losses the efficiency for charging and discharging is 0.8 and 0.5 respectively, and the total efficiency of the EESS is 0.4.

2.1. Life-Cycle Analysis

Life-cycle analysis is a technique for targeting the environmental impacts (e.g. use of resources and effect on human health) of a product. Two ISO standards (ISO 14040 and 14044) describes the framework and principles for conducting LCA, including the inventory compilation, impact assessment and interpretations of the results.

The software SimaPro v8.3 is used for the LCA, where the characterisation factors from the midpoint (H) ReCiPe 2016 method v1.1 [34] and cumulative energy demand (CED) method v1.10 [35] were used for determining global warming potential and energy performance, respectively. CED method calculates the energy intensity of a process (in MWh) used for storing 1 MWh of available electricity, which is the functional unit for this LCA. Real data is provided by experiments from the RED-stack (power density) and the model of the pumping losses. Background data from Ecoinvent v3.4 database were used for upstream processes, such as material and electricity production.

For this LCA the Cut-off U system is used. This system implies that the impact for producing a product is allocated to the first user, and a potentially recycling of the product does not benefit the LCA [36]. Using the Cut-off system also implies that any use of recycled materials in the production only include the impact of the recycling process and not the impact of the production of the materials itself.

10

3. Methodology

The maximum concentration in the experiments was set to 5.0 M even though the solubility limit of NaCl is 6 M, to avoid possible precipitation of salt inside the RED-stack. The dilute solution starts at 0.05 M due to the assumption of a drop in power density due to high ohmic resistance at lower concentrations [5]. When the EESS is fully discharged, both the solutions are at 2.525 M (the average concentrations is always 2.525 M). Experiments and the model are conducted with the solution temperature at both 25 °C and 40 °C. The model does not account for losses due to concentration polarisation. The material and cell properties are given in Tab. 1.

Table 1: Materials and cell properties for the cell stack used in the experiments and in the modeling. *measured **calculated

Name	Symbol	Value
Soltuions		
Flow salt solution	$\Phi_{\text{solutions}}$	7.0 ml min^{-1}
Flow redox solution	Φ_{redox}	7.0 ml min^{-1}
Flow salt solution $(\Phi/(60 \times 10^6 \times \delta_{\text{s}} \times w \times \epsilon))$	$v_{\text{solutions}}$	0.0012 m s^{-1}
Flow redox solution $(\Phi/(60 \times 10^6 \times \delta_{\text{s}} \times w \times \epsilon))$	v_{redox}	0.011 m s^{-1}
Concentration dilute solution	c_d	0.05 - 2.525 M
Concentration concentrated solution $(c_c = 5.05 - c_d)$	c_c	5.0 - 2.525 M
Temperature	T	[297, 313] K
Dielectric constant $(T = [297, 313])$	τ_w	[78.4, 73.2] [20]
Resistance		
Resistance AEM	R_{AEM}	1.44×10^{-4} Ω m^2 [9]
Resistance CEM	R_{CEM}	1.00×10^{-4} Ω m^2 [10]
Cell geometry		
Channel thickness	δ_{s}	1.55×10^{-4} m
Channel width	w	4.0×10^{-2} m
Channel length	l	9.0×10^{-2} m
Membrane thickness	δ_{m}	5.0×10^{-5} m
Spacer parameters		
Open area	OA	0.65
Thread thickness	δ_t	8.0×10^{-5} m
Mesh opening	δ_o	3.37×10^{-4} m
Maximum spacer shadow	$\beta\,(1 - OA)$	0.35
Specific gravity (polyester)	SG_{poly}	1380 kg m^{-3} [37]
Weight fabric	m_{spacer}	0.0333 kg m^{-2} *
Apparent gravity	AG_{spacer}	214.6 kg m^{-3} **
Porosity (1-$AG_{\text{poly}}/SG_{\text{poly}}$)	ϵ	0.844

11

3.1. Membrane Treatment

The membranes used in the stack measurements and the measurements of the perm-selectivity were delivered wet in an ED-40 stack from Fumatech. The cell contained NaCl solution; thus the membranes were already ion-exchanged to Na^+ and Cl^- ions. Before stack measurements, the correct concentrations were pumped through the flow compartments until a stable OCV was obtained. The same membranes were later used to measure the perm-selectivity, where the membranes were kept in approximately 1 M NaCl for minimum one week before the permselectivity was measured.

3.2. Permselectivity Measurements

The membrane was placed between two solutions with different concentrations, were rubber rings on each side of the membrane prevented leaking. The solution was stirred throughout the experiment with magnetic stirrers. An agar/3 M KCl salt bridge, half-filled with the solutions from the glass containers, connected the glass containers with a saturated KCl solution. Two double junctions Ag/AgCl electrodes with the 3 M KCl solution were set in the saturated KCl solution at the end of the salt bridge. The setup can be seen in Fig. 5.
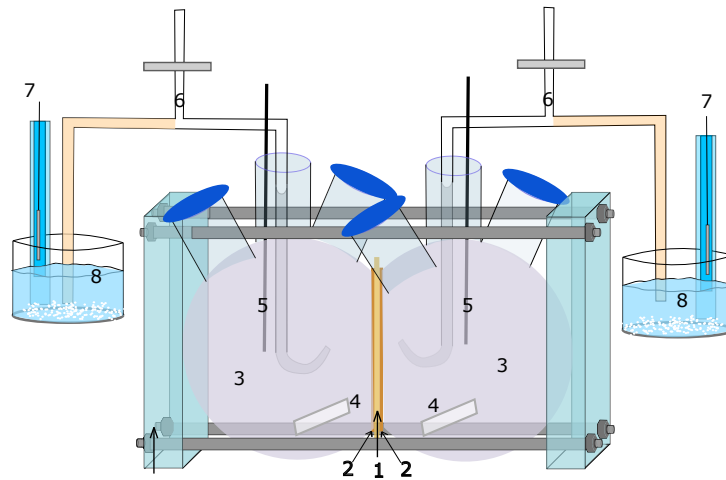

Figure 5: The setup used for the permselectivity measurements, inspired by [8]. In the figure 1) is the membrane, 2) are the sealing rings, 3) are the glass containers, one with dilute solution and one with concentrated solution, 4) are the magnets for stirring, 5) are the thermometers, 6) are the Agar/KCl-saltbriges, 7) are the double junction Ag/AgCl reference electrodes and 8) are saturated KCl solutions.

The OCV was measured for a minimum of one hour. The permselectivity was found by dividing the measured OCV by the calculated OCV given in Eq. (2) (without α).

Each membrane (FAS-50 and FKS-50) were measured with each pair of concentrations: 5.000 M/0.05000 M, 4.500 M/0.5500 M, 3.000 M/2.050 M and 2.525 M/2.525 M. The same concentrations used in the stack experiments were also used in the permselectivity measurements, with one exception: The stack measurement carried out with solutions of equal

12

concentration (2.525 M), had a calculated OCV of 0 V, making the calculation of the perm-selectivity invalid. The concentrations were set to 2.525 M and 2.800 M instead.

3.3. Stack Measurements

The cell used for stack measurements was a Fumatech ED-40 cell. The stack contains four elements: Electrodes (titanium and iridium plasma coated stainless steel), membranes (FAS-50 and FKS-50), spacers (polyester) and gaskets (PVC), that are pressed together by two endplates of PEEK. An illustration of the setup is shown in Fig. 6.

The dilute and concentrated solutions were pumped in through two separate openings at the endplate. Two holes for each of the solutions (four in total) distribute the solution over the membrane area, where the dilute and the concentrated solutions are distributed in every second compartment. Both solutions flow out from the cell through two holes in the other end plate (see Fig. 6). The redox solution is pumped in at each electrode and flows out from the same electrode, to avoid short-circuiting by circulating the redox solution. The redox couple used in the experiments was a solution of $FeCl_2$ (0.5 M), $FeCl_3$ (0.5 M) and NaCl (1.0 M). When the cell was not in use, dilute (0.05-0.5 M) NaCl solution was pumped in at all compartments, including the redox compartment.
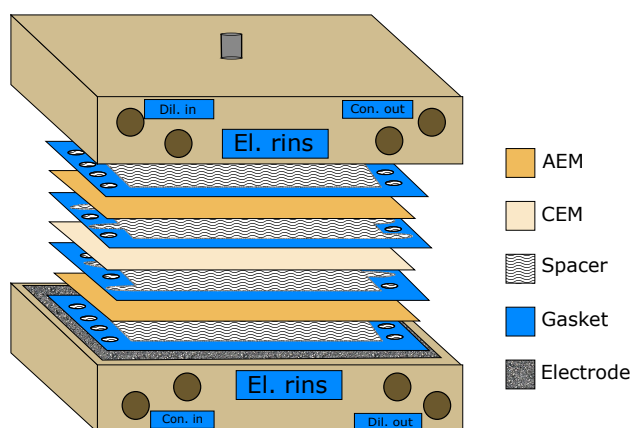

Figure 6: The figure shows the RED stack used in all experiments reported in this article. The holes at the front of the stack are the inlet and outlet of the dilute solution, the concentrated solution and the electrode rinse (redox) solution. In the experiments, nine cell pairs were used (ten AEM and nine CEM).

To reduce the loss in temperature between the heated inlet solutions and the flow channels inside the RED stack, the RED stack and most of the tubings were kept in a heating cabinet throughout the measurements at 40 °C. The temperature was measured in the inlet salt solutions, and at the outlet solution. The temperature was kept within 40 ± 1 °C.

Linear sweep voltammetry (LSV) [38, p.178] was run for each concentration and temperature. In all LSV experiments reported in this article, scan rates of 5 mV s⁻¹ were used. From these experiments, the current and voltage were recorded directly.

13

Chronopotentiometry measurements of the cell containing the electrodes, the redox solution and one AEM is carried out to compensate for the voltage losses at the electrode. The current steps are held for 1000 s and randomised. Between every current step, the current is set to zero for 100 s. At the end of every step, the resistance is found from dividing the measured voltage by the set current. The resistance is plotted versus the current density to find the ohmic region and its ohmic resistance, R_{blank}. The unit cell voltage is found from:

$$E_{uc} = \frac{E_{total} - R_{blank} \times I}{N} \tag{25}$$

where E_{total} is the total stack voltage, R_{blank} is the resistance of wires, electrodes, redox solution and one AEM, I is the current and N is number of unit cells.

3.4. Life-Cycle Analysis

In the present LCA, 1 GWh of the energy storage capacity is considered, which is 20 % of the daily energy needed for 100'000 Norwegian households (every house using a total of 20 MWh per year [39]). The energy storage capacity of the EESS is defined by the amount of NaCl solution available. In every cubic meter of concentrated salt solution there is 15 MJ, or 4.2 kWh, of available energy relative to a cubic meter of a dilute salt solution [3], meaning two tanks of 2.4×10^5 m^3 with NaCl solution are needed; one for the dilute and one for the concentrated solution. The number should be multiplied with 10 for operating within 90 % of the state of charge. The energy is assumed to be used during 2 hours in the evening (duck curve [5]), with an energy to power ratio (E2P) of 2. The operation life span is set to 20 years.

The power density needed is defined by the number of unit cells and the total membrane area, where the power density needed from the RED stack is 0.5 GWh (E2P = 2). The power density from the RED stack is found from measurements, while the pumping losses are calculated from Eq. (20). From the measured power density, the total membrane area can be calculated, together with the endplate area (from the number of unit cells). The inventory used for the LCA analysis is given in Tab. 2 and Tab. 7 . The LCA of the EESS indulges only the production phase, where the base scenario uses spacer material PA6.6 (see Tab. 2). The global warming effect (kg CO_2 equivalents) per kg and the CED (Wh) per kg for all the materials included in the EESS is given in Tab. 3.

14

Table 2: The materials used in an EESS

Component	Name in SimaPro	Density
Salt solution	Sodium chloride, powder GLO	2.525 mol L^{-1} *
Redox solution	Iron(II)chloride GLO, and Iron(III)chloride,	
	without water, in a 12 % iron solution state GLO	0.5 mol L^{-1}
	Iron(II) chloride GLO | market for	0.5 mol L^{-1}
Solute	Water, deionized, from tap water	1000 kg m^{-3}
End-plate	Aluminium scrap, post-consumer GLO	2700 kg m^{-3}
Gasket	Polyvinylchloride, suspension polymerised GLO	1380 kg m^{-3}
CEM	Cationic resin GLO	1100 kg m^{-3}
AEM	Anionic resin GLO	1100 kg m^{-3}
Electrode	Graphite, battery grade GLO	
	at user Europe without Switzerland	7 kg m^{-2} **
Tank material	Lean concrete RoW	2300 kg m^{-3}
Spacer materials		
	Nylon 6-6 GLO| market for (PA66)	1140 kg m^{-3}
	Nylon 6 GLO| market for (PA6)	1130 kg m^{-3}
	Polyethylene terephthalate, granulate,	
	amorphous GLO| market for (PET)	1350 kg m^{-3}
	Polypropylene, granulate GLO| market for (PP)	905 kg m^{-3}

* mean value of the concentrated and dilute concentration
** measured in house

15

Table 3: Global warming (GW) and CED per kg for all materials used in the EESS.

Resource	GW	CED
	kg CO_2 eq./kg	kWh/kg
NaCl	0.305	1.14
$FeCl_2$	0.300	1.19
$FeCl_3$	0.642	2.53
Gasket	2.03	16.9
IEM (cationic resin)	1.88	10.7
IEM (anionic resin)	3.60	17.6
Electrode	2.29	15.0
End-plate	0.833	0.155
DI water	9.92×10^{-4}	5.39×10^{-3}
Tank	0.0753	0.106
Spacer materials		
PA6.6	6.74	38.5
PA6	9.88	34.3
PET	3.28	22.0
PP	2.18	21.2

16

4. Results and Discussion

This section contains all the experimental results from permselectivity and stack measurements, where the results are compared with modelled data. An LCA of the EESS is included at the end.

4.1. Permselectivity

The measured permselectivity at room temperature (23 °C) for AEM (FAS-50) and CEM (FKS-50) is given in Fig. 7.
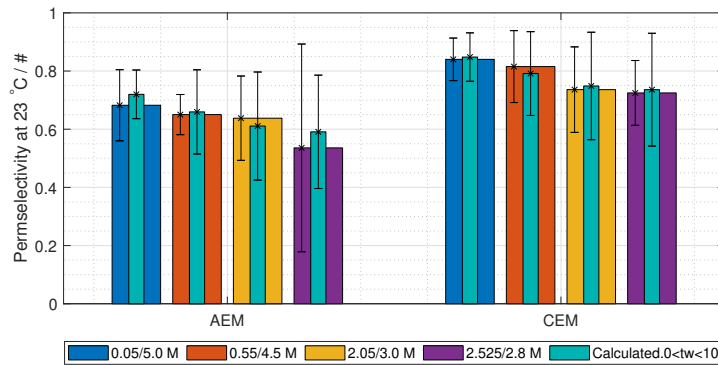

Figure 7: Measured permselectivity of AEM and CEM at 23 °C with 0.95 confidence interval, together with the modelled permselectivity (Eq. (3)), with water transport number from 0 to 10, and salt transport numbers equal to Długołecki et al. [12] (see Eq. (4)).

The measured permselectivity is in the same range as given in the literature: Daniilidis et al. [40] measured a mean permselectivity of 0.8 and 0.7, for concentration ratios 0.050 M/5.0 M and 0.55 M/4.5 M, respectively. Daniilidis, referring to Veerman et al. [41], pointed out that the losses from co-ion transport increase with increasing concentration difference. An increase in the concentration difference will also increase the counterion transport, increasing the permselectivity. However, the data obtained here cannot be used to say anything about the two transport numbers separately.

The permselectivity of CEM is higher than for AEM, as expected, partly due to a higher amount of fixed charges in CEM than in AEM, reducing the number of co-ions in the CEM.

Due to a constant mean concentration between the compartments in every experiment, the salt transport number can be assumed constant. Given the measured permselectivity in Fig. 7, and salt transport numbers given in Eq. (4) (0.8 for AEM and 0.9 for CEM), the water transport number is as given in Tab. 4. The large uncertainty in the permselectivity leads to large uncertainty in the transport numbers. Zlotorowicz et al. [8] found the water transport number to be 8±7 and 6±1 for two similar membranes from Fumatech but at lower concentrations.

Smaller concentration differences need to be evaluated to find the exact contribution from the water and salt transport number on the permselectivity [8]. However; in this work, the aim is to find the permselectivity at *operating conditions*.

17

Table 4: Transport number of water in fumatechs membranes FAS-50 and FKS-50, given salt transport numbers from Eq. (4) and measured permselectivities given in Fig. 7.

Concentration / M/M	0.05000/5.000	0.5500/4.500	2.050/3.000	2.525/2.800
t_w AEM	5±7	4±2	4±4	6±9
t_w CEM	5±4	4±4	5±4	5±3

4.2. Stack Measurements

The resistance of a blank cell with one AEM and redox solution is shown in Fig. 8, where the ohmic resistance of the blank cell is 3×10^{-3} Ω m^2. At an absolute current density lower than 30 A m^{-2}, the non-ohmic losses are negligible. As seen later the operational current density of the full RED/ED stack is mainly in the ohmic region and a constant resistance is subtracted.
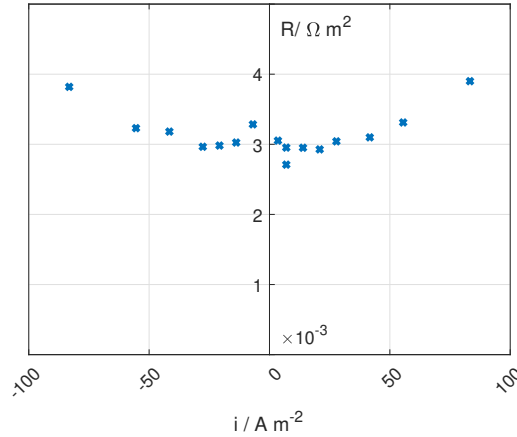

Figure 8: Resistance of the blank RED cell with one AEM and redox solution at 25 °C.

The polarisation curves for the EESS stack measurements are given in Fig. 9. The unit cell potential given in the graph is calculated from Eq. (25).

The OCV of the RED-stack gained from Fig. 9 is plotted together with the calculated potential from Eq. (2) (with α equal to 1 and the measured data given in Fig. 7) in Fig. 10a. The unit cell resistance (R_{blank} subtracted), together with the calculated resistance, is given in Fig. 10b.

The theoretical OCV ($\alpha = 1$) is two times as high as the measured OCV. One of the reasons is the drop in the permselectivity mentioned in subsection 4.1. Tedesco et al. [42] and Daniilidis et al. [40] also measured half of the theoretical potential using similar concentrations for the concentrated feed as in our experiments.

The measured resistance is higher than the calculated resistance. A reason for this is an underestimation of the membrane resistance in the calculation, where the membrane resistance included in the calculated resistance is taken from the membranes datasheet from
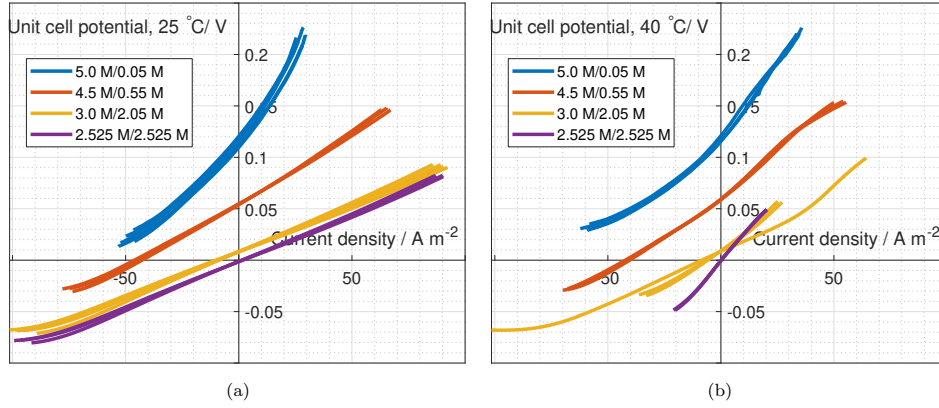
18

Figure 9: Polarisation curves for all measurements obtained at 25 °C (a) and at 40 °C (b).
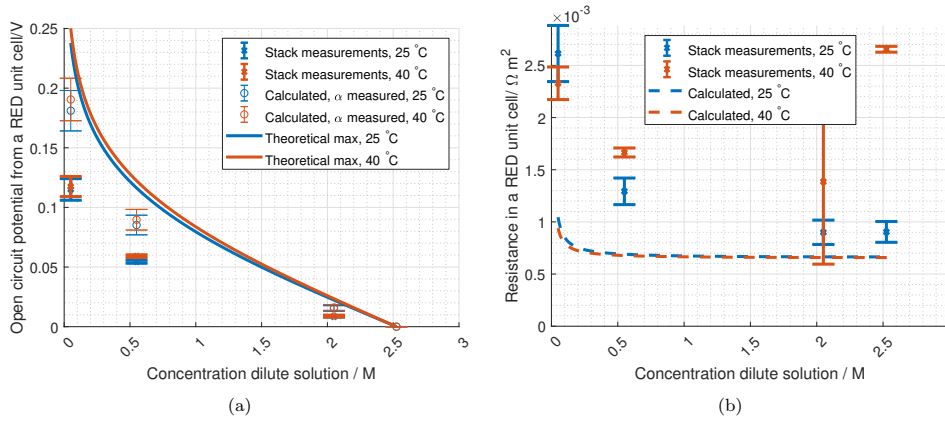

Figure 10: Figure (a) shows the OCV for one unit cell included the calculated OCV from Eq. (2). Figure (b) shows the unit cell resistance included the evaluated resistance from Eq. (11), compared to dilute concentration. $C_c = 5.05 - C_d$.

Fumatech [9, 10]. However, these values are representative for 0.5 M NaCl, while the mean concentration is 2.525 M in the experiments conducted in this work. Conductivity measurements carried out on FAS-50 and FKS-50 soaked in up to 4.3 mol kg^{-1} NaCl, indicate a decrease in conductivity with increasing mean concentration. For FAS-50 the conductivity decreased from 4 to 2 mS cm^{-1} from 0.9 to 4.3 M in concentration at 23 °C, and from 8 to 3 mS cm^{-1} at 40 °C. The conductivity in FKS-50 decreased from 2 to 1 mS cm^{-1} from 0.9 to 1.8 M, and from 4 to 1 mS cm^{-1} from 0.9 to 1.8 M at 40 °C [43]. These measurements indicate that the calculated resistance in Fig. 10b is too low.

The cell resistance (mostly) increases with decreasing dilute concentration, due to the decrease in the resistance of the dilute flow compartment. Jalili et al. simulated the resistance

19

in the flow compartments in RED using OpenFOAM [44], where they found the resistance to be 0.4 mΩ m^2 and 0.04 mΩ m^2 for the dilute and concentrated solutions respectively. Thesis calculations are similar to our total calculated resistance. At 40 °C, the unit cell resistance decrease from 0.05000 M to 0.5500 M. The measured stack resistance at 40 °C for 2.525 M/2.525 M is high compared to the other resistances at 40 °C, where this irregularity was not detected during measurements but is lightly due to oxidation and precipitation of the iron in the redox-solution. This could also have affected the measurements at a dilute concentration of 2.05 M, and be the reason for the high uncertainty.

The ohmic losses can be reduced by decreasing the compartment thickness. As mentioned, 100 µm or lower is recommended by Vermaas et al. [45]. Increasing the temperature would also decrease the resistance of the solutions [43]. Jalili et al. showed a significant decrease in stack resistance, increasing the temperature from 10 °C to 80 °C. However, for the temperature range used in the present study Jalili et al. did not show a prominent change in stack resistance [5], where the stack resistance was measured to be between 1 and 2 mΩ m^2 between 25 °C and 40 °C. It is also worth mentioning that the model in [5] uses concentrations 0.01 M to 1.0 M. However, both this study and the previous study by Jalili et al. [5] show that membranes with lower resistance, even at high concentration difference a high temperature, should be prioritised.

The polarisation curves in Fig. 9 show dominating ohmic losses in the galvanostatic region where the EESS is discharged. At higher current densities in the galvanostatic region (and in the super galvanostatic region) some losses due to electrode kinetics can also be observed. At the electrolytic region, where the EESS is charged, the losses are mainly ohmic, with some losses from the mass transfer, particularly for the higher concentration differences.

The kinetic losses can be reduced by increasing the temperature [46, p.200]. In the experiments carried out in this work, only the sodium chloride solutions were heated, but not the redox solution, due to increased oxidation and precipitation of the iron at elevated temperature. Increasing the temperature of the redox solution could be done in a sealed container with nitrogen or argon bubbled into it. The mass transport losses can be reduced by increasing the mixing achieved by increasing the flow of the solution. This will, however, increase the pumping losses.

The power density gained from RED and the power density used in ED (given a charging current half the discharging current), and the corresponding current density at maximum power is given in Tab. 5 (together with a 95 % confidence interval).

The maximum power density from discharging the EESS is 1.5 ± 0.3 W m$_{uc}^{-2}$ (per unit cell area) and 2.0 ± 0.3 W m$_{uc}^{-2}$ at 25 °C and 40 °C respectively. The charging energy, given half the discharging current, is 2.1 ± 0.3 W m$_{uc}^{-2}$ and 3.8 ± 0.9 W m$_{uc}^{-2}$ at 25 °C and 40 °C respectively.

The discharge power density for Egmond et al. [7] was approximately 0.5 W m^{-2}, 0.7 W m^{-2} and 0.7 W m^{-2} for 10 °C, 25 °C and 40 °C respectively at a discharge current density of 15 A m^{-2}. Daniilidis et al. [40] measured power density from RED between 3.8 and 6.7 W m^{-2} from 25 to 60 °C respectively, with solutions of 0.01 M and 5 M. Daniilidis used membranes from Neosepta and Tokuyama Inc. and had a mean permselectivity of almost 0.8 at maximum concentration difference.

20

Table 5: Peak power current density, peak power density and charging power density at different temperatures and different concentrations fractions.

c_c/c_d	25 °C			40 °C		
	$i^{\text{dischar.}}$	$P^{\text{dischar.}}_{\max}$	$P^{\text{char.}}$	$i^{\text{dischar.}}$	$P^{\text{dischar.}}_{\max}$	$P^{\text{char.}}$
M/M	A m^{-2}	W m$^{-2}_{\text{uc}}$	W m$^{-2}_{\text{uc}}$	A m^{-2}	W m$^{-2}_{\text{uc}}$	W m$^{-2}_{\text{uc}}$
5.000/0.05000	28±3	1.5±0.2	2.1±0.3	42±7	2.0±0.3	3.8±0.9
4.500/0.5500	22±1	0.60±0.08	0.76±0.07	21±2	0.58±0.02	0.8±0.1
3.000/2.050	4.8±0.8	0.020±0.003	0.024±0.006	3±2	0.015±0.008	0.019±0.009
2.525/2.525	0.8±0.2	(5±3)×10^{-4}	(6±4)×10^{-4}	0.08±0.09	(1.2±0.4)×10^{-5}	(2.2±2.1)×10^{-5}

The power lost in pumping is presented in Fig. 11, while the efficiency for the charging and discharging EESS, together with the total energy storage efficiency, is given in Tab. 6. The pumping losses are neglectable compare to the power density output from EESS at the higher concentrations ratios.
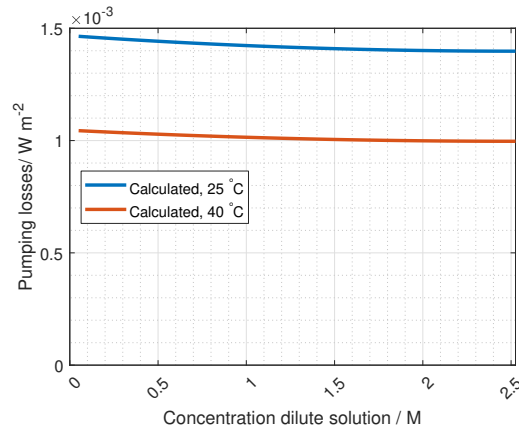

Figure 11: The power density lost in pumping.

Table 6: The efficiency of ED, RED and ED/RED.

c_c/c_d	25 °C			40 °C		
	η_{ED}	η_{RED}	$\eta_{\text{ED/RED}}$	η_{ED}	η_{RED}	$\eta_{\text{ED/RED}}$
M/M	(max=0.8)	(max=0.5)	(max=0.4)	(max=0.8)	(max=0.5)	(max=0.4)
5.000/0.05000	0.74±0.16	0.47±0.10	0.34±0.11	0.65±0.21	0.40±0.10	0.26±0.11
4.500/0.5500	0.79±0.10	0.50±0.08	0.39±0.08	0.75±0.14	0.48±0.04	0.36±0.07
3.000/2.050	0.76±0.22	0.47±0.11	0.36±0.13	0.78±0.54	0.47±0.34	0.36±0.37
2.525/2.525	0.27±0.17	0	0	0.013±0.009	0	0

As seen from Tab. 6, the efficiency of discharging the EESS is between 0.40 and 0.50,

21

compared to the reversible potential ($\eta_{\text{RED,max}} = 0.5$). Under the concentration ratio 3.000 M/2.050 M, the pumping losses are higher than the power output, and according to this study, the battery should not be operated below this concentration limit. At 3.000 M/2.050 M and higher ratios, the power density shows no significant variation with concentration ratio. The deviation from 0.5 can be explained by pumping power and kinetic losses. As seen from Fig. 9, the kinetic losses are highest at the concentration ratio 0.05000 M/5.000 M and 40 °C.

There is no significant change in efficiency with temperature indicating a proportional change in the available energy with the measured energy. Earlier studies by Jalili et al.[5] show an impact from the temperature on efficiency. However, the temperature range in the study by Jalili et al. is larger than the one given here. Daniilidis et al. [40] found an energy efficiency of 15-20 % at the same concentration difference as used in our experiments, where the efficiency decreased with temperature from 20 % to under 10 % from 10 °C to 60 °C. However, Daniilidis et at. [40] used a fixed current for all their experiments. Veerman et al. [41] measured a stack efficiency of 18 % using four RED cells operating in series.

4.3. Life-Cycle Analysis

The inventory for the LCA of the EESS is given in given in Tab. 7. The table includes results from the measurements and the modelling.

The total mass of each material needed for building a full-scale EESS with a life span of 20 years is given in Tab. 8. The amount of mass used of every material is divided by the number of days the battery operates ($20 \times 365 = 7300$) since the storage capacity also is given per day. The mass of each material per MWh stored is also included in Tab. 8.

The impact on global warming and the CED is calculated from multiplying the data given in Tab. 8 with the data given in Tab. 3. The impacts for the base scenario, using PA6.6 for the spacer, is given in Fig. 12.
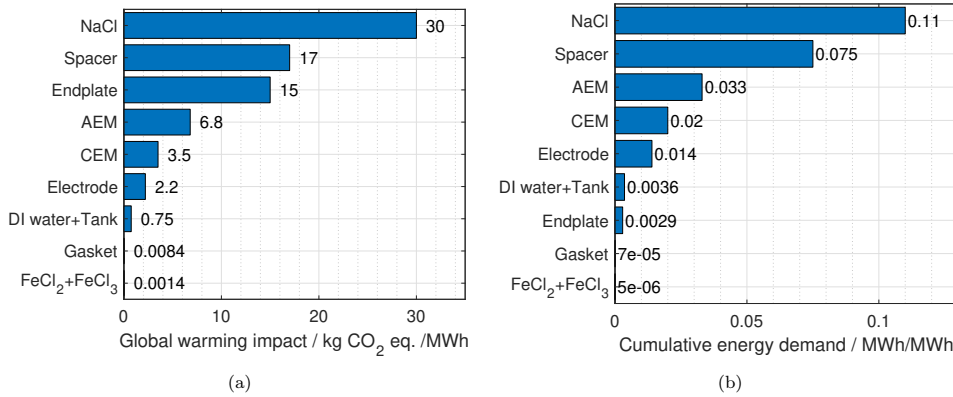

Figure 12: Impact on global warming (kg CO_2 eq./MWh) (a) and the CED (MWh/MWh) (b) for each component in the production phase.

22

Table 7: The inventory description of EESS with 1 GWh storage capacity

Name	Value
General	
Usable capacity	1 GWh *
Discharging time	2 hours *
Operation time	20 years *
Available energy in NaCl solutions	4167 Wh m^{-3} [3]
Water tanks	
Total storage capacity needed ^{a}	10 GWh ***
Volume water tanks	2.4×10^6 m^3 ***
Number of tanks	2 *
Height	100 m *
Radius	276 m ***
Wall thickness	0.30 m *
RED Stack	
Power density needed (E2P=2)	0.5 GW ***
Number of unit cells	500 *
Height flow channel	155 μm **
Height redox channel	155 μm **
Porosity flow channel	1
Thickness membrane	50 μm **
Thickness endplate	0.05 m *
Power density per membrane area RED	1 W m^2 **
Power density per membrane used by pumps	0.0005 W m^2 ***
Total membrane area needed	5.00×10^8 m^2 ***
Cell area needed ($A_{\mathrm{mem.}}/2N_{\mathrm{uc}}$)	5.00×10^5 m^2 ***
Volume redox solution	155 m^3 ***
Volume NaCl solution in cell	7.75×10^4 m^3 ***

*set, ** measured, *** calculated, ^{a} considering 90 % of state of change

The most significant impact on both global warming and the CED is the NaCl and the spacer material. Some of the NaCl (and DI water) can be substituted by brine water which is included in the SimaPro database. However, lack of information on the brine water concentration in SimaPro, this alternative was dropped due to the transparency of the LCA. Another solution is to decompress and heat seawater or brine water (see [43]), and thereby make the solution more concentrated. However, the LCA of this process is not included in this work due to time limitations.

The spacer has more possibilities for variations. Four different spacers are included to compare their total global warming and CED. This is given in Fig. 13. The best material to use for the spacer, concerning global warming and energy demand, is polypropylene.

23

Table 8: Material used per day and per functional unit (1 MWh) for the EESS.

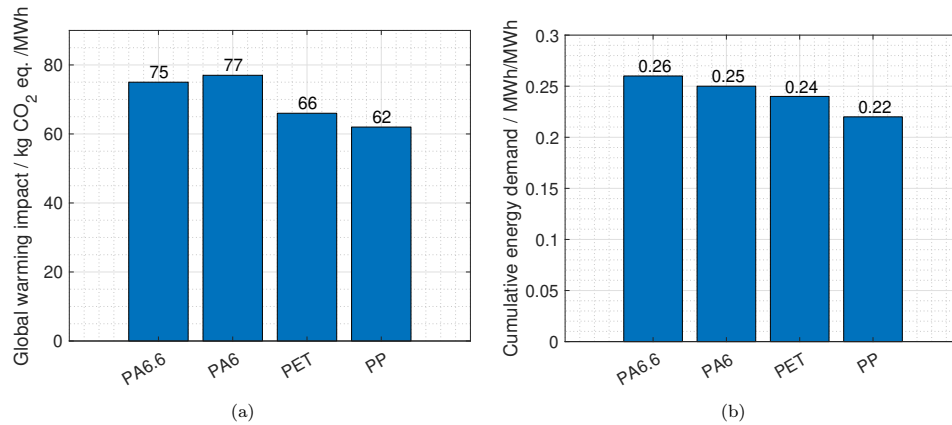| Name	Mass per day of operation kg/d	Mass per energy stored kg/MWh
NaCl	9.76×10^4	97.6
$FeCl_2$	1.72	0.0017
$FeCl_3$	1.35	0.0013
End-plate	1.85×10^4	18.5
Gasket	4.15	0.00415
IEM	3.77×10^3	3.77
DI water	6.34×10^5	658
Electrode	959	0.959
Tank	3.28×10^3	3.28
Spacer materials		
PA6.6	1.94×10^{-3}	1.94
PA6	1.92×10^{-3}	1.92
PET	2.30×10^{-3}	2.30
PP	1.54×10^{-3}	1.54

Figure 13: Impact on global warming (kg CO_2 eq./MWh) (a) and the CED (MWh/MWh) (b) for the total prodcution phase using four different spacer materials.

The environmental footprint of EESS was compared to a system of the same storage capacity with Li-ion batteries. Many LCAs of Li-ion batteries are conducted [47–50], reporting on global warming factors between 17'000 - 356'000 kg CO_2 eq. per MWh capacity (storage per day). The large variation originates from the different assumption on energy demand for cell manufacturing and the amount of material needed [50]. If an assumption on three years of operation for the Li-ion battery, the global warming factor range between 16 and 333 kg CO_2 eq. per MWh (total storage), which is in the range of the global warming factor of the

24

EESS. The CED for Li-ion batteries is reported to range between 267 and 600 MWh/MWh capacity (storage per day) [47], corresponding to a range from 0.24 to 0.55 MWh/MWh (total storage), which mostly is higher than the CED from EESS.

Due to a large difference in efficiency between EESS (0.4) and Li-ion ($\approx$1), the user phase of the LCA should be included for a fair compare of CED between the two energy storage systems.

25

5. Conclusion

Reverse electrodialysis and electrodialysis can be combined to an EESS, where the system is charged by increasing the concentration difference between two salt solutions and discharged by mixing the same two salt solutions trough alternating AEMs and CEMs. Given this system being a closed system, the concentrations can be higher than the naturally occurring concentration.

Permselectivity of one AEM and one CEM from Fumtech is measured at NaCl concentrations close to saturation. The mean permselectivity decreases from 0.95 using seawater, to a mean permselectivities ranging from 0.6 to 0.8 using concentration ratios from 2.800 M/2.525 M to 5.000 M/0.05000 M, indicating a higher co-ion transport with the counterions and/or water transport in the membranes.

Stack measurements of a RED/ED cell were conducted, measuring the current density and voltage. The OCV at 5.000 M/0.05000 M was measured to 115±9 mV and 118±8 mV at 25 °C and 40 °C respectively. The measured OCV was 50 % of the theoretical ($\alpha = 1$), and 60 % of the calculated OCV using the measured permselectivities.

The power density from EESS was measured to 1.5 ± 0.2 W m^{-2} and 2.0 ± 0.3 W m^{-2} at 25 °C and 40 °C respectively. The efficiency was 0.4 for the higher concentration differences, while the system was found to use more energy than gained for concentration ratios below 3.000 M/2.050 M. The temperature impact on the OCV and power density were not significant in this study, showing the need for raising the temperature above 40 °C in future studies. The main objective is to increase the permselectivity of the membranes and reduce their ionic resistance.

An LCA of EESS with a total energy storage capacities of 1 GWh per day, 1 W m$_{\mathrm{m}}^{-2}$ power density and a lifetime of 20 years, give a global warming factor of 62-75 kg CO_2 eq. per MWh and a CED of 0.22-0.26 MWh/MWh for the production phase of the EESS. This study indicates that the mass of CO_2 eq. released in the production phase per MWh storage capacity using EESS, is similar to the mass of CO_2 eq. per MWh released from Li-ion battery production, and that the CED per MWh capacity, is in the lower range of the CED from large scale Li-ion storage.

26

6. Acknowledgment

27

Nomenclature

α	membrane permselectivety
$\alpha_{\mathrm{aw,NaCl}}$	constant used to define the activity of water
β	shadow factor of the spacer on the membranes
$\beta_{\mathrm{aw,NaCl}}$	constant used to define the activity of water
δ_0	mesh opening in spacer
δ_t	thread thickness in spacer
δ_{m}	membrane thickness
δ_{s}	spacer thickness
ϵ	porosity water channel
ϵ_0	permittivity of vacuum
$\epsilon_{\mathrm{r,w}}$	dielectric constant of water
η	efficiency
γ	activity coefficient
μ	viscosity
ν	number of ions per molecule
Φ	flow of solution
$\rho_{\mathrm{sol.}}$	resistivity solution
ρ_{w}	density of water
ρ_{w}	density water
σ	conductivity
τ_{w}	dielectric constant of water
A	variable used in the definition of γ
a	distance of closes approach between ions in solution
a_{w}	activity of water
AG_{spacer}	apparent gravity (spacer)

28

B variable used in the definition of γ

b molality

c molarity

D_h hydraulic diameter

E electric potential

e elementary charge

F Faraday constant

h hydration number

I ionic strength

i current density

K_B Boltzmann constant

l length flow channel

M_w molar mass of water

N number of unit cells

N_A Avogadro number

OA open area spacer

P power density

R universal gas constant

r_Ω area specific ohmic resistance

R_blank Ohmic resistance of the RED/ED stack with two electrodes, redox solution, one AEM and the wires to the potentiostat

S_sp surface of the spacer filaments

SG_poly specific gravity polyester (fabric of spacer)

T temperature

t_s transport number of salt

t_w transport number of water

29

v	flow velocity
V_{sp}	volume of the spacer filaments
w	width flow channel
x	mole fraction
z	valence number

30

References

[1] DNV-GL, Renewables, Power and Energy Use Forecast 2050, Tech. rep., DNV-GL (2017).

[2] E. R. Sholkovitz, Flocculation of dissolved organic and inorganic matter during the mixing of river water and seawater, Geochimica et Cosmochimica Acta 40 (7) (1976) 831–845. `doi:10.1016/0016-7037(76)90035-1`.

[3] N. Boon, R. Van Roij, Blue energy from ion adsorption and electrode charging in sea and river water, Molecular Physics 109 (7-10) (2011) 1229–1241.

[4] R. E. Pattle, Production of electric power by mixing fresh and salt water in the hydroelectric pile, Nature 174 (4431) (1954) 660.

[5] Z. Jalili, K. W. Krakhella, K. E. Einarsrud, O. S. Burheim, Energy generation and storage by salinity gradient power: A model-based assessment, Journal of Energy Storage 24 (2019) 100755.

[6] R. S. Kingsbury, K. Chu, O. Coronell, Energy storage by reversible electrodialysis: The concentration battery, Journal of Membrane Science 495 (2015) 502–516.

[7] W. J. van Egmond, U. K. Starke, M. Saakes, C. J. N. Buisman, H. V. M. Hamelers, Energy efficiency of a concentration gradient flow battery at elevated temperatures, Journal of Power Sources 340 (2017) 71–79. `doi:10.1016/j.jpowsour.2016.11.043`.

[8] A. Zlotorowicz, R. V. Strand, O. S. Burheim, Ø. Wilhelmsen, S. Kjelstrup, Wilhelmsen, S. Kjelstrup, The permselectivity and water transference number of ion exchange membranes in reverse electrodialysis, Journal of Membrane Science 523 (October 2016) (2017) 402–408. `doi:10.1016/j.memsci.2016.10.003`.

[9] FuelCellStore, Fumasep FAS-50 (2019).
URL `https://www.fuelcellstore.com/fumasep-fas-50`

[10] FuelCellStore, Fumasep FKS-50 (2019).
URL `https://www.fuelcellstore.com/fumasep-fks`

[11] J. Kamcev, D. R. Paul, G. S. Manning, B. D. Freeman, Ion diffusion coefficients in ion exchange membranes: significance of counterion condensation, Macromolecules 51 (15) (2018) 5519–5529.

[12] P. Długołecki, B. Anet, S. J. Metz, K. Nijmeijer, M. Wessling, Transport limitations in ion exchange membranes at low salt concentrations, Journal of Membrane Science 346 (1) (2010) 163–171. `doi:10.1016/j.memsci.2009.09.033`.

[13] L. Giorno, E. Drioli, H. Strathmann, Water Transport in Ion-Exchange Membranes, Springer Berlin Heidelberg, Berlin, Heidelberg, 2016. `doi:10.1007/978-3-662-44324-8_1434`.

[14] K. S. Pitzer, R. T. Pabalan, Thermodynamics of nacl in steam, Geochimica et Cosmochimica Acta 50 (7) (1986) 1445–1454.

[15] C. Larchet, B. Auclair, V. Nikonenko, Approximate evaluation of water transport number in ion-exchange membranes, Electrochimica acta 49 (11) (2004) 1711–1717.

[16] R. H. Stokes, R. A. Robinson, Ionic hydration and activity in electrolyte solutions, Journal of the American Chemical Society 70 (5) (1948) 1870–1878.

[17] E. Glueckauf, The influence of ionic hydration on activity coefficients in concentrated electrolyte solutions, Transactions of the Faraday Society 51 (1955) 1235–1244.

[18] R. Pytkowicz, Activity coefficients in electrolyte solutions, no. v. 2 in Activity Coefficients in Electrolyte Solutions.

[19] A. C. Ribeiro, V. M. Lobo, H. D. Burrows, A. J. Valente, A. J. Sobral, A. M. Amado, C. I. Santos, M. A. Esteso, Mean distance of closest approach of potassium, cesium and rubidium ions in aqueous solutions: Experimental and theoretical calculations, Journal of Molecular Liquids 146 (3) (2009) 69–73.

[20] C. G. Malmberg, A. A. Maryott, Dielectric constant of water from 0 °C to 100 °C, Journal of research of the National Bureau of Standards (1) 1–8. `doi:10.6028/jres.056.001`.

[21] O. Miyawaki, A. Saito, T. Matsuo, K. Nakamura, Activity and activity coefficient of water in aqueous solutions and their relationships with solution structure parameters, Bioscience, biotechnology, and biochemistry 61 (3) (1997) 466–469.

[22] V. N. Afanasiev, A. N. Ustinov, I. Y. Vashurina, State of hydration shells of sodium chloride in aqueous

31

solutions in a wide concentration range at 273.15- 373.15 k, The Journal of Physical Chemistry B 113 (1) (2008) 212–223.

[23] G. Onori, Ionic hydration in sodium chloride solutions, The Journal of chemical physics 89 (1) (1988) 510–516.

[24] G. Z. Ramon, B. J. Feinberg, E. M. V. Hoek, Membrane-based production of salinity-gradient power, Energy & Environmental Science (11) 4423. `doi:10.1039/c1ee01913a`.

[25] J. W. Post, H. V. M. Hamelers, C. J. N. Buisman, Energy recovery from controlled mixing salt and fresh water with a reverse electrodialysis system, Environmental Science and Technology 42 (15) (2008) 5785–5790. `doi:10.1021/es8004317`.

[26] P. Długołęcki, A. Gambier, K. Nijmeijer, M. Wessling, Practical potential of reverse electrodialysis as process for sustainable energy generation, Environmental Science and Technology 43 (17) (2009) 6888–6894. `doi:10.1021/es9009635`.

[27] EXW Foxboro, CONDUCTIVITY ORDERING GUIDE (1999).

[28] C. H. Hamann, A. Hamnett, W. Vielstich, Electrochemistry, CambrWiley-VCH, 1998.

[29] Schlumberger, Resistivity of NaCl Solutions, Tech. rep., Schlumberger (2017).

[30] D. A. Vermaas, E. Guler, M. Saakes, K. Nijmeijer, Theoretical power density from salinity gradients using reverse electrodialysis, Energy Procedia 170–184`doi:10.1016/j.egypro.2012.03.018`.

[31] A. Daniilidis, R. Herber, D. A. Vermaas, Upscale potential and financial feasibility of a reverse electro-dialysis power plant, Applied energy 119 (2014) 257–265.

[32] A. Da Costa, A. Fane, D. Wiley, Spacer characterization and pressure drop modelling in spacer-filled channels for ultrafiltration, Journal of membrane science 87 (1-2) (1994) 79–98.

[33] J. Kim, M. Wilf, J.-S. Park, J. Brown, Boron rejection by reverse osmosis membranes: national recon-naissance and mechanism study-phase 1, Tech. rep., Georgia Institute of Technology (2006).

[34] M. Huijbregts, Z. Steinmann, P. Elshout, F. Stam, G. andVerones, M. Vieira, A. Hollander, M. Zijp, R. van Zelm, ReCiPe 2016 v1.1 (2017).

[35] H.-J. Althaus, C. Bauer, G. Doka, R. Dones, R. Hischier, S. Hellweg, S. Humbert, T. Köllner, Y. Loer-incik, M. Margni, T. Nemecek, Implementation of Life Cycle Impact Assessment Methods - Data v2.0 (2007) (2007).

[36] Ecoinvent, Allocation cut-off by classification, `https://www.ecoinvent.org/database/system-models-in-ecoinvent-3/cut-off-system-model/allocation-cut-off-by-classification.html`, [Online; accessed 20-July-2019] (2019).

[37] Marlow, Material Properties, `https://www.marlowropes.com/material-properties`, [Online; ac-cessed 20-July-2019] (2019).

[38] D. Pletcher, R. Greff, R. Peat, L. M. Peter, J. Robinson, J. Pletcher, Derek and Greff, R and Peat, R and Peter, LM and Robinson, Instrumental methods in electrochemistry, Elsevier, 2001.

[39] SSB - Ann Christin Bøeng, Energy consumption in households, 2012 (2014).
URL `https://www.ssb.no/en/energi-og-industri/statistikker/husenergi/hvert-3-aar/2014-07-14`

[40] A. Daniilidis, D. A. Vermaas, R. Herber, K. Nijmeijer, Experimentally obtainable energy from mixing river water, seawater or brines with reverse electrodialysis, Renewable Energy 123–131`doi:10.1016/j.renene.2013.11.001`.

[41] J. Veerman, R. M. De Jong, M. Saakes, S. J. Metz, G. J. Harmsen, Reverse electrodialysis: Comparison of six commercial membrane pairs on the thermodynamic efficiency and power density, Journal of Membrane Science 343 (1) (2009) 7–15.

[42] M. Tedesco, E. Brauns, A. Cipollina, G. Micale, P. Modica, G. Russo, J. Helsen, Reverse electrodialysis with saline waters and concentrated brines: a laboratory investigation towards technology scale-up, Journal of Membrane Science 492 (2015) 9–20.

[43] K. W. Krakhella, R. Bock, F. Seland, O. S. Burheim, K. E. Einarsrud, Heat to H$_2$, submitted to MDPI Energies (2019).

[44] Z. Jalili, O. S. Burheim, K. E. Einarsrud, New insights into computational fluid dynamic modeling of the resistivity and overpotential in reverse electrodialysis, ECS Transactions 85 (13) (2018) 129–144.

32

[45] D. A. Vermaas, M. Saakes, K. Nijmeijer, Doubled power density from salinity gradients at reduced intermembrane distance, Environmental Science and Technology 45 (16) (2011) 7089–7095. `doi:10.1021/es2012758`.

[46] K. Oldham, J. Myland, A. Bond, Electrochemical science and technology: fundamentals and applications, John Wiley & Sons, 2011.

[47] R. Arvidsson, M. Janssen, M. Svanström, P. Johansson, B. A. Sandén, Energy use and climate change improvements of li/s batteries based on life cycle assessment, Journal of Power Sources 383 (2018) 87–92.

[48] C. Samaras, K. Meisterling, Life cycle assessment of greenhouse gas emissions from plug-in hybrid vehicles: implications for policy - supporting online information (2008).

[49] H. C. Kim, T. J. Wallington, R. Arsenault, C. Bae, S. Ahn, J. Lee, Cradle-to-gate emissions from a commercial electric vehicle li-ion battery: a comparative analysis, Environmental science & technology 50 (14) (2016) 7715–7722.

[50] L. A.-W. Ellingsen, C. R. Hung, A. H. Strømman, Identifying key assumptions and differences in life cycle assessment studies of lithium-ion traction batteries with focus on greenhouse gas emissions, Transportation Research Part D: Transport and Environment 55 (2017) 82–90.

33